8-5-2004

# Optoelectronic Multifractal Wavelet Analysis for Fast and Accurate Detection of Rainfall in Weather Radar Images

Radhika Dahale
*University of New Orleans*

# OPTOELECTRONIC MULTIFRACTAL WAVELET ANALYSIS FOR FAST AND ACCURATE DETECTION OF RAINFALL IN WEATHER RADAR IMAGES

A Thesis

Submitted to the Graduate Faculty of the
University of New Orleans
in partial fulfillment of the
requirements for the degree of

Master of Science
in
The Department of Electrical Engineering

by

Radhika H. Dahale

M.S., University of New Orleans, 2004

August 2004

# DEDICATION

This thesis is dedicated to my wonderful family without whose support it was impossible. I would like to express my gratitude to my parents (Mr. H.G.Dahale and Mrs. U.H. Dahale) whom I admire and will always be indebted for their unconditional love, support and encouragement. I am highly grateful to my husband Parikshit for always being by my side and for his immense love, and faith in everything I did. I appreciate adoration bestowed by my sister and brother which has always motivated me to attain higher goals. I express my sincere thanks to Balli for providing inestimable help time and again. I thank all of them whose presence has comforted me in my hardships.

I also highly appreciate the help extended by other family members, friends and well wishers whom I might have missed out unintentionally.

# ACKNOWLEDGMENTS

I am grateful to Dr.Alsamman for being my major advisor. I would like to express my gratitude for his vital and continued support during the course of my thesis. I wish to convey my heartiest thanks to Dr. Charalampidis's invaluable contribution. I am highly grateful to him for his time, involvement and patience during the course of my work. I would also like to thank Mr. Jovanovich for being an excellent teacher and for agreeing to be on my defense committee.

# TABLE OF CONTENTS

# LIST OF TABLES

# LIST OF FIGURES

# ABSTRACT

In this thesis we propose an automated process for the removal of non-precipitation echoes present in weather radar signals and accurate detection of rainfall. The process employs multifractal analysis using directional Gabor wavelets for accurate detection of the rain events. An optoelectronic joint transform correlator is proposed to provide ultra fast processing and wavelet analysis.

Computer simulations of the proposed system show that the proposed algorithm is successful in the detecting rainfall accurately in radar images. The accuracy of the algorithms proposed are compared to accurate results that were generated under expert supervision. Results of the proposed system are also compared to results of QC algorithm for the ground validation software (GVS) used by TRMM ground validity Project and a previous QC algorithm. Several statistical measures computed for different reflectivity ranges show that the proposed algorithm gives accuracy as high as 98.95%, which exceed the 97.46% maximum accuracy for the GVS results. Also, the minimum error rate obtained by the proposed algorithm for different dB ranges decreases to 1.09% whereas the GVS results show a minimum error rate of 1.80%. The rain rate accumulation confirms the success of the proposed algorithm in the accurate removal of non-precipitation echoes and a higher precision in rain accumulation estimates.

# CHAPTER 1

# 1. INTRODUCTION

Weather plays an important part in people's lives today affecting day-to-day activities. Therefore, weather forecasting on the seasonal scale has become increasingly significant to make important decisions on a daily basis. Weather forecasting is not a new concept and the art dates back to the 650 B.C. In those days the predictions for short-term weather changes were made depending on the appearance of the clouds. The Greek philosopher Aristotle presented several theories related to the weather forecast until the seventeenth century. Numerous attempts were made over the centuries to produce weather forecast all based on the weather knowledge, experience and individual observations. Eventually this was found to be inadequate and a need for added knowledge regarding the atmosphere was felt. It was not until the fourteenth century that several instruments were invented to measure data which would make meteorological observations which would improve weather predictions. In the mid-nineteenth century several weather observation sites were set up across the globe where not only meteorological observations were made but, the data could also be exchanged between different sites. This data was then studied by observers' and weather maps drawn. As these observation networks rapidly extended over the globe more and more data was available everywhere increasing knowledge facilitating weather forecast. Several instruments were developed which would make meteorological observations like the pressure, temperature and moisture. This data was then transmitted to the ground stations where they were fed into computers. One of the well known practices adopted is the launching of balloons in the air which record different meteorological parameters like temperature, pressure, humidity, speed of wind which is then transmitted and recorded in the computers.

## 1.1. History of Weather Radars

The radar technology employed in the mid nineteenth century has resulted in a breakthrough in making accurate weather forecasts. Radars were used to detect, locate

and measure the amount of precipitations in the atmosphere by meteorologists. These were interpreted as colorful areas in the radar images. Initial radar images were in grayscale however; with the advent of modern technology the demand for color imagery was stimulated. Current radar images are colored with wide range of intensity which helps the precipitation identifiable. The National Weather Service (NWS) provides weather, hydrologic, and climate forecasts and warnings for the United States, its territories, adjacent waters, and ocean areas for the protection of life and property and the enhancement of the national economy. In 1980 the United States Weather Services deployed NEXRAD (Next Generation Weather Radar) system which has 137 Doppler radars (called WSR-88D) throughout the country. The image data from all these sites is collected to detect the presence of precipitation in the atmosphere.

## 1.2. Problem Description

Though the radar images which are expected to depict only precipitations in weather they also include a lot of false information affecting its quality of the decision. Hence it is extremely important to analyze the images and to detect and eliminate this false information from the radar image retaining only the precipitation echoes. This process basically is referred to as the quality control. Quality control of radar image is thus important major step involved after the acquisition of the images. Previous quality control methods were based on just the visual observation of the image data. This required experienced personnel who made decisions on the basis of his experiences and knowledge. However, this subjective analysis was rather slow and not completely reliable. Thus, these limitations demanded a faster quality control process with minimum human interference i.e. automation. With the massive use of computers, several algorithms have since been generated to provide effective quality control algorithms. The TRMM (Tropical Rainfall Measurement Mission) satellite launched by the NASA has developed a quality control algorithm which makes use of echo height and reflectivity values. However it is not completely automated and involves a high number of parameters. Research in this area has been extensively done and algorithms employing different methods are used. Some of the algorithm use neural networks, fuzzy logic which involves use of several parameters like the temperature, reflectivity, velocity, echo

heights and many more. One such quality control algorithm makes use of multifractal analysis along with the textural and intensity information. Hence, there is a need for the development of systems and algorithms which are: accurate in the detection of rain events and elimination of false echoes, automated to minimized or eliminated human supervision, and fast to provide response in or close to real-time.

### 1.3. Multifractal Analysis and Wavelets

Radar images have shown to exhibit a lot of irregularity and can be treated as texture images. They do not have regular textures which can be defined by simple models. In this irregularity is embedded a lot of essential information which can help in analyzing the image and hence cannot be disregarded. Use of multifractal analysis is not new and it has been employed in the area of geophysics and proved to be successful in image analysis [13-16]. However, very few quality control algorithms are present in the literatures which are based on multifractal analysis. The multifractal analysis mainly exploits the scale invariant behavior of the images. This analysis aids in extracting underlying information in the texture of the image. Multifractal analysis is helpful in characterizing radar images based on the textural information and also in improving the quality control. Another significant feature of the radar images is its directionality. This directionality feature of the radar images can be exploited to acquire important information.

Wavelets analysis can be employed to extract features such as directionality from the images. Roots of wavelet analysis date back to the eighteenth century and its uses in modern technology are quite common. The major advantage of wavelets is the ability to characterize textural properties in multiple resolutions. Thus, the application of wavelets analysis for irregular image textures, like radar images has been a helpful tool for radar image analysis [14,17]. Directional wavelets can be used to characterize the directionality of the radar images at different scales. The idea is to analyze the image using different directions of the wavelets to extract useful information.

## 1.4. Optical Processing

The quality control algorithms using multifractal analysis certainly involve extensive image analysis. With the inclusion of the directional wavelets the task becomes even more complex and slow. Thus, these computationally intensive operations often are time consuming. Consequently, the need for some way to ensure fast quality control arises.

Optical processing has the potential for providing the processing power needed for real-time analysis of weather images. Optical processing is not an innovative field and its use dates back to the eighteenth century. Optical signal processing has witnessed a rapid growth in recent years. The speed of optical systems and its massive parallelism of make it possible for real time image processing. Another advantage of the optical processing is the ability to generate the Fourier transforms using a simple converging lens and at the speed it takes the coherent light to pass through the lens. The most time consuming operations in the image processing are the filtering and wavelet processing operations. Performing these operations optically would ensure a speedy computation without compromising the quality of the algorithm.

## 1.5. Thesis Organization

This thesis is organized into five major chapters. Chapter 2 deals with the basics of radar imagery. It describes the operation of the NEXRAD weather radar system and acquisition of the weather radar images. In chapter 3 the concept of quality control in weather radar images is introduced. It presents the different quality control algorithm pertinent to this thesis. It also is devoted to the explanation of the quality control algorithm proposed in this thesis. Chapter 4 describes the role of optics in this thesis. It gives an overview of the optics and is devoted exclusively to the optical implementation of the algorithm proposed in the thesis. The results and comparisons of the proposed algorithm are presented in chapter 5 along with performance measures and comparisons to other algorithms. Finally, chapter 6 presents the conclusion of the work in this thesis and suggestions for future work in this field. Finally, the appendix comprises of the

original test images used for every hour, the corresponding results obtained using the proposed algorithm and the accurate rain events.

# CHAPTER 2

# 2. NEXRAD AND WEATHER RADAR

## 2.1. Background [3],[4]

The current radar system used by the United States National Weather Services sites is known as **NEXRAD** which is an acronym for **NEX**t Generation Weather **RAD**ar. These sites provide meteorological data and the official designation is WSR-88D (**W**eather **S**ervice **R**adar 19**88** – **D**oppler). It uses the advanced Doppler type radar network and has replaced the conventional radar. The Doppler radar as the name suggests works on the basis of the Doppler Theory. It detects the change in the frequency or wavelengths of the storms that move towards or away the radar. This concept is used to derive all the velocity products obtained by the radar.

### *2.1.1. Workings of the NEXRAD*

The radar transmitter creates pulses of radio waves, which are focused in a beam by an antenna and is transmitted through the atmosphere. Targets scatter the electromagnetic energy is in all directions and a fraction of this scattered energy returns back to the radar. This backscattered radiation is called the "radar echo". The process is depicted in Fig.2.1.

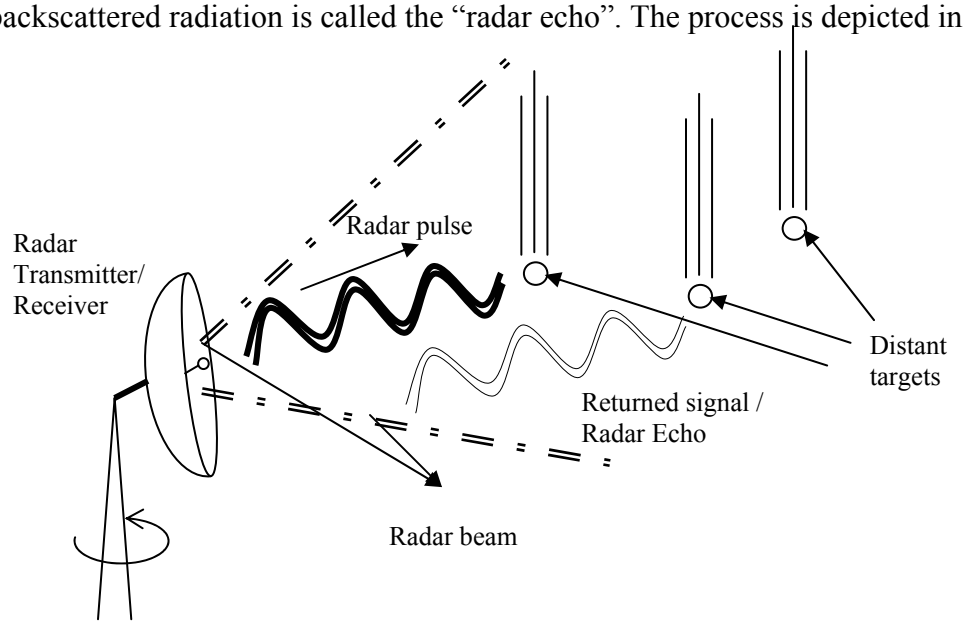


**Fig. 2.1 Working of the Radar**

The magnitude of the reflected signal is directly proportional to the size of the object in the path of the beam and is analyzed by computers. The NEXRAD being a Doppler radar also detects the "shift in the phase" of the reflected signals caused by the motion of the objects in the atmosphere.

The complete process of transmitting the electromagnetic pulses, listening to the returned signal, and emitting the next pulse is a extremely fast and takes place for about 1300 times every second. The radar spends quite a long period in listening to the reflected signals. When the total transmission and listening time of the radar is calculated it's understood that the former takes place just for 7 seconds in each hour while the rest of the time is spent in listening to the reflected signals. The radar dish makes $360^{O}$ azimuth scans for different elevations. The radar images used in the thesis were acquired from the radar site at Melbourne, Florida on March 31, 1999. These images that were scanned for 24 hours by the radar for every 9 minutes are acquired at the lowest two elevations.

### *2.1.2. Precipitation Echoes*

Precipitation occurs when cloud particles become too heavy to remain suspended in the air and fall to the earth in the forms of hail, rain, freezing rain, sleet or snow. Precipitations intercepted by the radar beam is scattered at different rates depending on the movement of the distant targets like precipitation and in different directions. The reflected signals from the precipitation, known as "precipitation echoes" are assembled to produce the radar reflectivity images. The precipitation intensity (reflectivity) is measured in dBZ which is actually the local radar base reflectivity product. Larger precipitations and higher precipitation concentration produces a stronger radar echo seen as high dBZ reflectivity value in the radar image. While radars can detect precipitation, it does not detect the condensation that forms the clouds. The time elapsed between the transmission and reception of the pulse at the radar and the orientation of the radar antenna is used to determine the location of events.

### *2.1.3. Non-Precipitation Echoes*

Radars can usually detect most intense precipitations within a certain range, typically 5dBZ-75 dBZ. However, light rain, snow or drizzle from shallow cloud weather systems is not necessarily detected. In addition to this, radar reflectivity images may depict false echoes mainly caused by the following effects:

*Atmospheric Effects:* The majority of the non-precipitation echoes in radar images is caused by anomalous propagation. These are legitimate meteorological, non-precipitation phenomenon detected by the radar and not a result of the radar errors. The anomalous propagation occurs in specific atmospheric conditions when the typical state of the atmosphere is reversed. In this particular non-standard condition the atmosphere is cool near the ground and warmer higher up and appears typically on clear nights with calm winds. This consequently causes temperature variation between the cool air near the ground and the layer of warm air above, which in-turn causes the difference in the density in the air. When the radar beam travels through the atmosphere in these conditions the refracted radar beam is reflected back to the radar and it appears as a strong echo in the radar images. Echoes from this atmospheric phenomenon are usually characterized by large uniformly colored areas usually centered on the radar site.

*Ground Clutter:* These non-precipitation echoes are a result of the reflections that are caused by the radar beam side lobes as seen in Fig. 2.2. The energy from the side lobes reflected back to the radar by non-weather related ground objects like tall buildings, hills which appear as strong echoes in the radar reflectivity image. As the presence of these objects is inevitable, this type of non-precipitation echoes appears in almost all radar reflectivity images and are known as “ground clutter”. Other semi-stationary objects such as fluttering leaves and cars also produce ground clutter returns. The ground clutter generally appears near the radar as a circular region with a random pattern. It has a have high reflectivity value due to the high density of the target and it exhibits rapidly changing intensities in an unrealistic fashion. These characteristics are atypical of the precipitation echoes and make ground clutter easily identifiable in the radar images.

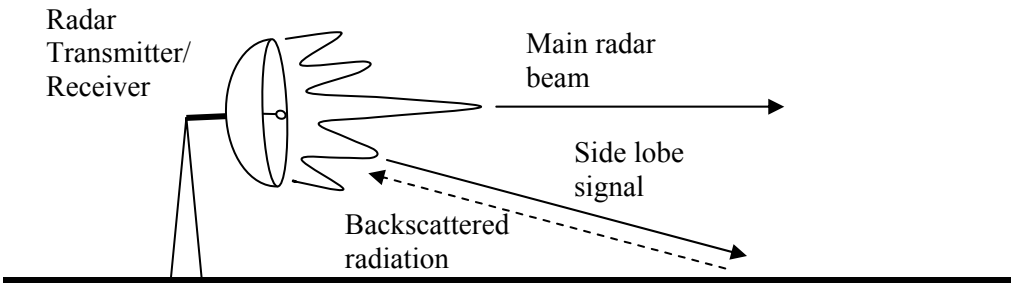


**Fig. 2.2 Ground Clutter**

*False Echoes:* In addition to pulses reflected from the precipitation, energy is also reflected from moving objects like aircraft, areas of smoke or ash. The reflected signals from large fires, swarms of insects, flocks of birds or even the surface appear in almost all radar reflectivity images.

*Beam Spreading:* The radar beam spreading is not a result of an inaccuracy in the radar but just a result of the beam characteristics. The radar beam is focused in a shape of a cone as seen in Fig.2.1 with its tip at the radar site. As the beam progresses into the atmosphere it starts to widen. In this process the energy of the radar beam is attenuated as the targets in the path of the radar beam absorb energy. Also, the energy reflected from the targets close to the radar will be greater. This affects the resolution of the radar. As a result the reflectivity value will be lower even if it is from actual precipitation leading to inaccuracies.

Due to the aforementioned effects, the weather images acquired from the weather radars is not an accurate depiction of the actual rainfall. It is not always the case that high reflectivity values correspond to precipitations echoes but are sometimes a result of pulses reflected back from non-precipitation related objects. Therefore, it becomes extremely necessary to distinguish between these non-precipitation echoes and the precipitation echoes to provide accurate detection. To reduce non-precipitation echoes radars can be set to operate in two basic modes: ‘clear air mode’ and ‘precipitation mode’ depending on the significant and insignificant precipitation in the atmosphere respectively.

*Clear Air Mode:* The radar operates in the 'clear mode' when the atmosphere is clear and there is no significant precipitation in the atmosphere. In this operating mode the radar becomes more sensitive so that it can detect very small precipitation if present in the atmosphere. Due to the absence of significant precipitation the radar scans and acquires an image every 10 minutes. Moreover, it also scans at few elevations (typically 5).

*Precipitation Mode:* The radar switches to the precipitation mode when the amount of precipitation in the atmosphere is very high. In such conditions it is not required for the radar to be very sensitive and hence the radar is less sensitive. However, it provides higher resolution for stronger. Unlike the 'clear air mode' the radar operating in this mode scans for more number of times producing images every 6 minutes. Also, it uses more number of elevations (typically 9) and a greater range. Thus, the maximum precipitation echoes are detected by the weather radar.

However, these precautions do not eliminate the possibility of introducing undesirable echoes in the radar images. Some non-precipitation echoes like ground clutter can be easily detected and removed by viewing, but others cannot be easily identified. Also, over-interpretation can result in errors when echoes are mistaken to be stronger than actual.

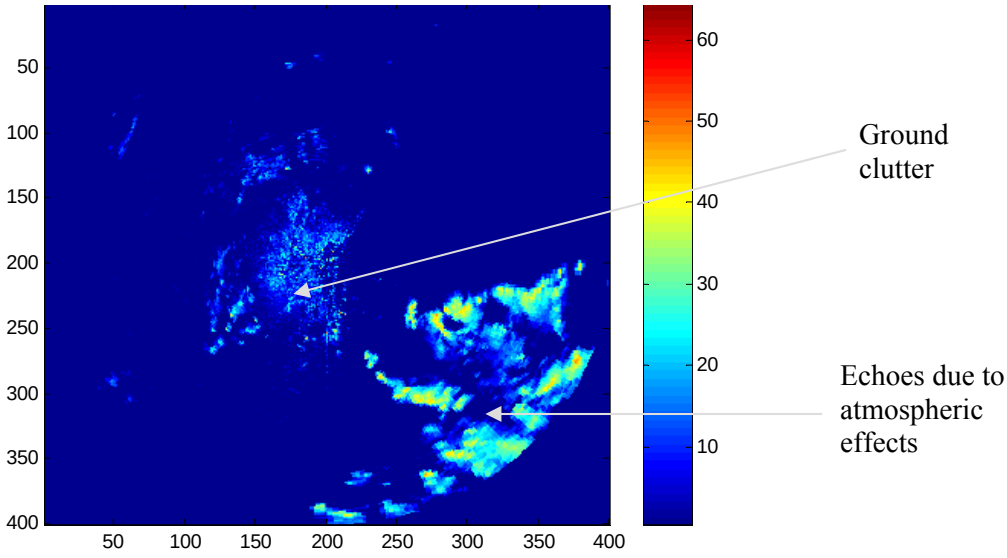


**Fig. 2.3 Reflectivity image at elevation 1**

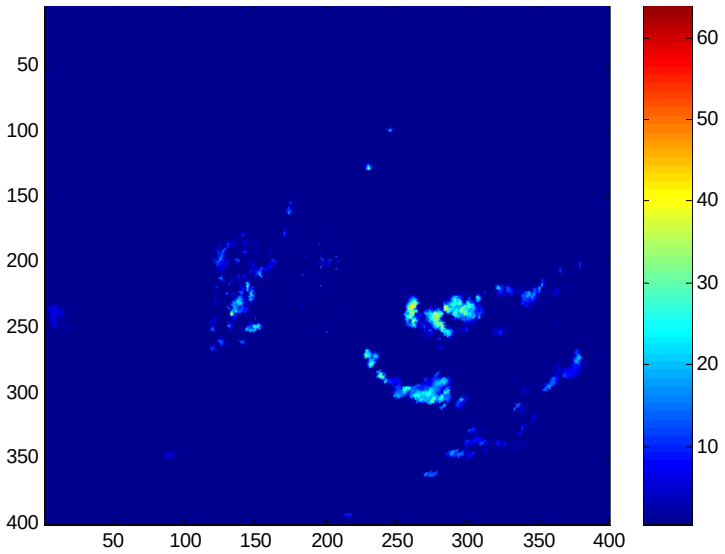


**Fig. 2.4 Reflectivity image at elevation 2**

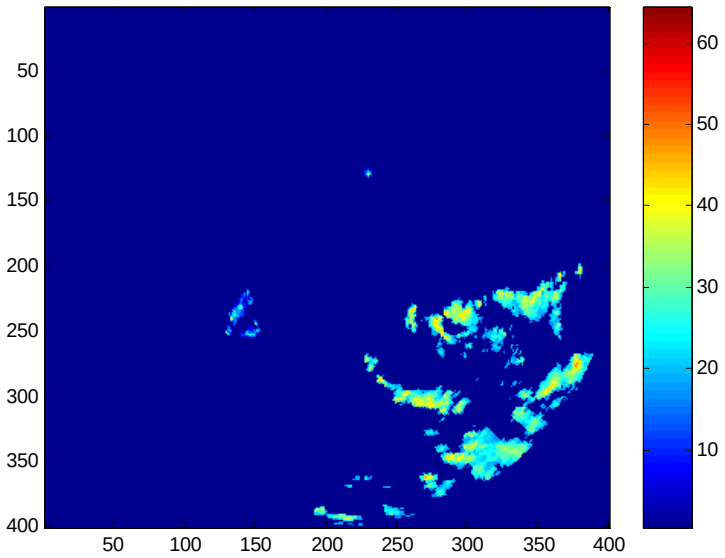


**Fig. 2.5 Actual precipitation echoes**

The images seen in Fig.2.3 and Fig.2.4 were acquired from the radar site situated at Melbourne, Florida on 31, March 1991 at two different elevations. The image in Fig 2.3 is acquired at a lower elevation and it can be observed that it contains a lot of non-precipitation echoes along with the precipitation echoes. On the other hand the image in Fig. 2.4 is acquired at a higher elevation and as discussed it has a considerably few non-precipitation echoes. Fig. 2.5 depicts the image with only the precipitation echoes present. As can be seen, the ground clutter at the center of the images as well as the lower reflectivity value echoes surrounding the actual precipitation echoes caused due to atmospheric effects are eliminated.

# CHAPTER 3
# 3. QUALITY CONTROL

## 3.1. Identifying Precipitation

Reflectivity can be defined as the amount of energy that is reflected back to the radar receiver from a precipitation, as compared to a reference power density at a distance of 1 meter from the radar antenna. It is apparent from the previous sections that the radar base reflectivity product image is an interpretation of the radar echoes detected by the radar receiver for a 360-degree volume scan at every elevation. However, the operational characteristics have their own limitations resulting in the corruption of the data discussed in preceding section 2.1.3. Apart from the consequence of anomalous propagation, the radar beam misses a lot of information at higher elevations. It is necessary that the undesired false information be removed or corrected from the acquired image data. The process of extracting accurate data and the removal of false data related to rainfall is referred as the 'quality control' (QC).

Knowing the characteristics of precipitation and non-precipitation echoes helps in discriminating one from the other. The operating mode of the radar indicates the proportionality between the reflectivity values and the strength of precipitation. Accordingly, the intensity of the precipitation can be examined and a preliminary distinction between the different echoes can be made. The following table shows how precipitation intensity corresponds with the dBZ values:

**Table 3.1 Relation between reflectivity values and precipitation intensity**

| Range (dBZ) | Precipitation intensity |
|---|---|
| 15-30 | Light |
| 30-45 | Moderate |
| 45 and higher | Heavy |

It is known that precipitation usually reflects at least 15 dBZ and hence values below this do not represent any significant precipitation. Precipitation has a characteristic

look and with practice one can identify the precipitations. One such image shown in Fig. 3.1 depicts a typical base reflectivity radar image from a particular radar site.

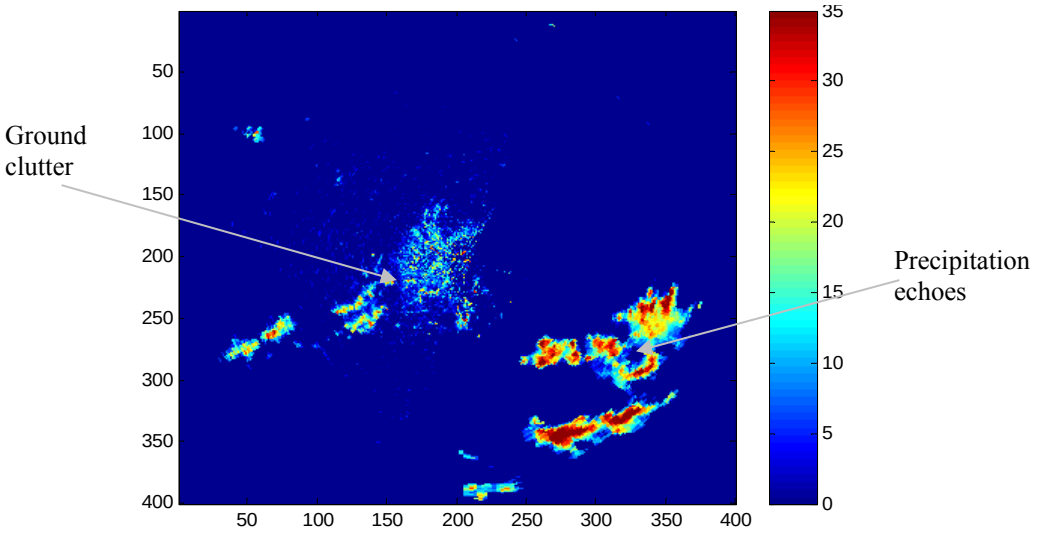


**Fig. 3.1 Base Reflectivity Image**

The radar image was acquired from Melbourne, Florida on March 31, 1999. The color bar on the lower left hand corner shows the reflectivity values corresponding to different colors. As seen in the figure at the center of the radar there are echoes, which follow a random pattern and also have high values. These are mainly the ground clutter returns explained in the previous section. There are also some other pixels in the image, which are spread out in a random fashion and have low values and can be identified as non-precipitation echoes. While the larger areas with high reflectivity values and uniform patterns are the precipitation echoes. Though non-precipitation echoes and non-precipitation echoes with distinguishable characteristics can be classified by observing just one image it is also important to study adjacent images to make an accurate classification. The reflectivity values can used to convert to rainfall rate using a simple equation. The relationship between the rainfall rate R (units) and the reflectivity Z (units) can be derived from [1] as,

$$R = \left(\frac{Z}{300}\right)^{\frac{2}{3}} \qquad \ldots\ldots\ldots\ldots\ldots\ldots\ldots\ldots\ldots\ldots \textit{(1)}$$

However, these methods are subjective and do not provide accurate and reliable results. All these limitations generate the necessity for developing an automated process which would provide fast and accurate results without the need for human supervision or feedback. Numerous algorithms have been proposed based on different techniques like fuzzy logic rules [6], reflectivity neural networks [5].

### *3.1.1. WSR-88D Quality Control*

The QC algorithm [6] used in the national Weather Service's WSR-88D makes use of the fuzzy logic to identify echoes. It makes use of moments, which are the mean radial velocity field, the standard deviation of the radial velocity field, the vertical difference of the reflectivity and the mean spectrum width field. These are used by three different algorithms to classify the radar echoes. The description of this algorithm is beyond the scope of this thesis and is detailed in [11] for reference. The major disadvantage [130] of this approach is that it is a relatively complex process that involves many parameters. Another limitation of the process is it inefficiency to detect mixed precipitation i.e. ground clutter embedded in precipitation [24].

### *3.1.2. Radar Data Quality Control*

The Tropical Rainfall Measuring Mission (TRMM) is a joint mission between NASA and the Japan Aerospace Exploration Agency (JAXA). It is designed to monitor and study the tropical rainfall. The TRMM office provides support to the Global Validation Program (GVP), which consists of 10 or more different ground validation sites over the tropics. Radar data is collected from all these different sites which is then processed and analyzed to determine the rainfall and related parameters.

A software referred as the Global Validation Software (GVS) is developed for the GVP. The software has a set of programs for three different levels. The quality control of the radar reflectivity image is performed in level 1. The quality control algorithm is referred to as the 1C-51 algorithm [10].

*3.1.2.1. The IC-51 Algorithm*

The objective of the 1C-51 algorithm is to improve the quality of the radar reflectivity images by removing the non-precipitation echoes caused by anomalous propagation and other effects. It uses eight different parameters: three echo height (maximum height of reflectivity above a certain threshold) thresholds and five radar reflectivity thresholds. These parameters are adjusted so as to optimize the performance of the algorithm. A brief description of the 1C-51 algorithm is given below [10],[12].

1. Check in a ~5x5 $km^2$ area in polar coordinates.
2. Height checks are made only when the top volume scan is higher than the examined volume.
3. Remove echo if any of the 4 criteria are satisfied:

   i $(Z_{top} < H3.or.\ Z_{max}(3\ km) \leq Z1)\ .and.\ (Z_{max}(H1) < Z3)$

   ii $Z_{top} < H2$

   iii $Z_{max}(1.5\ km) < Z0$

   iv $(Z > dBZ_{noise}\ .and.\ Z \leq Z2)$ in lowest tilt

The parameters H1, H2, and H3 represent echo height thresholds, Z0, Z1, Z2, Z3, and $dBZ_{noise}$ are the reflectivity thresholds, and Z is a reflectivity value.

The major limitation of this algorithm is that it is time consuming and tedious. It requires an experienced analyst who can select a different set of parameters for optimal performance. Also, the process must be repeated for every volume scan. In addition to this the process the literature shows [10] that it sometimes requires several iterations for every parameter until an optimal set of parameters is achieved. Thus, the shortcoming of the 1C-51 quality control algorithm is that it is not fully automated and requires human intervention.

### *3.1.3. Multifractal Analysis*

Radar images have shown to display extreme variability. It has a lot of irregular but essential information. Multifractals have been successfully used for characterizing meteorological radar data to characterize the inhomogeneities of the radar images [13-16]. The scale independent multifractal analysis of the radar images helps to study precipitation echoes at various scales. The multifractals formulation can be done by a variety of different techniques. The following describes the approach for QC from which is the basis for the QC algorithm proposed in this thesis.

#### *3.1.3.1. Scale-Invariant Multifractal Analysis*

Consider a N-dimensional signal denoted as $f(x_1, x_2, ....., x_N)$. The multifractal analysis of an N-dimensional signal $f(x_1, x_2, ....., x_N)$ is deployed to characterize the different statistical characteristics of the signal *f*. The signal is characterized by observing its behavior at different scales and establishing a scale-independent relationship. This is done by evaluating a statistical measure $(\mu_q)$ for every location with co-ordinates $(x_1, x_2, ..., x_N)$ in the signal at different scales '*s*'. A "*partition function*" denoted as $\langle \varepsilon^q_s \rangle$ is defined for this statistical measure. This partition function is actually the $q^{th}$ moment ensemble average of the measure which is scale dependent. The statistical measure $\mu_q(s,)$ is defined as

$$\mu_q(s, x_1, x_2, ...x_N) = \varepsilon_s^q(x_1, x_2, ...x_N) \qquad \text{……(2)}$$

where $\varepsilon_s$ is defined as

$$\varepsilon_s(x_1, x_2, ...x_N) = \sum_{x_1'=x_1-s/2}^{x_1+s/2} \cdots \sum_{x_N'=x_N-s/2}^{x_N+s/2} f(x_1', x_2', ...x_N') \qquad \text{……(3)}$$

and, s denotes the scale and q denotes the power

Eq. *(2)* described the ensemble average as the sum of the value of the function *'f'* inside a box of size *s* x *s* x *s* x *s* ...x *s* centered at location $(x_1, x_2, ..., x_N)$. The scale independent statistical behavior of the function *f* can be inspected by changing the statistical moments around the location $(x_1, x_2, ..., x_N)$ at every scale. A power-law

relation between the partition function and the scale parameter under consideration is developed. If a single power law exponent is adequate for describing the statistics of the function then the model is referred to as a monofractal. Since only a single scale can be used to describe the function statistics the model is said to have a monoscaling behavior. However, if more that one exponent is required to characterize the statistics of the function then the model is referred to as a multifractal and is said to have multiscaling behavior. For a discrete function the power law relation can be defined as

$$\left\langle \varepsilon_s^q \right\rangle \sim s^{K(q)} \qquad \ldots\ldots\ldots\ldots\ldots\ldots\ldots\ldots\ldots\ldots \quad (4)$$

where the function *K(q)* is the moment scaling function which is responsible for characterizing the multifractal behavior of the signal f. Similarly, if a single exponent is adequate to characterize all the statistics within the family that it's said to show *monofractal* behavior. On the other hand, if more than one exponent is enough to characterize all the statistics within the family than it shows *multifractality*. Appling a log on both the sides of equation (4) results in,

$$K(q) = \frac{\log\left\langle \varepsilon_s^q \right\rangle}{\log(s)} \qquad \ldots\ldots\ldots\ldots\ldots\ldots\ldots\ldots\ldots\ldots (5)$$

The slope of the line that best fits the points *(log(s), log‹$\varepsilon^q_s$›)* where, $s = s_1, s_2, \ldots\ldots s_L$ (shown in ascending order) can be an estimation of the function *K(q)*.

### *3.1.3.2. Multifractal Based QC*

The preceding section described how moments can be generation for of scale-independent multifractal analysis. This section explains how the multifractal analysis is used for QC as described in [1]. The QC algorithm in [1] is applied to both the textural and the intensity information. Only two radar reflectivity images acquired at two lower level elevations are used because they have the maximum information. It is in these elevations that non-precipitation echoes are present to a greater extent. Each radar pixel in the image corresponds to and area of 1 km$^2$. the textural information is significant for differentiating non-precipitation echoes from precipitation echoes. This information is characterized by the multifractal exponents given in equation (5). The non-precipitation

echoes exhibit a larger spatial variability in both the horizontal and vertical directions which produce more negative valued exponents. Precipitation echoes have a higher correlation with the neighboring pixels compared to the non-precipitation echoes. Intensity information is analyzed to exploit this feature. The objective of the algorithm is achieved by first extracting the textural information at different scales using multifractal exponents and then analyzing the intensity information of the radar image. Prior to processing it is necessary to convert the radar reflectivity image from the polar to the Cartesian form. This is done so that the conventional textural analysis can be performed in the image data. Also, for the computation of the multifractal exponents the reflectivity values are converted to linear units. The following sub-sections give a detailed description of the computation of the multifractal exponents and the steps involved in the QC algorithm in [1] in detail.

### *3.1.3.3. Description of the QC algorithm [1]*

The multifractal exponent *K(q)* characterizes the multifractal behavior of a given function – the function in this case being the two dimensional radar image. If the function is a temporally stationary signal, the ensemble average $\langle \varepsilon^q_s \rangle$ is practically approximated by a spatial filter. Since the images are considered at two different elevations, the multifractal exponent is computed in 3-dimensional blocks.

The multifractal QC algorithm uses two scales, $s_1$ and $s_2$, in which the $\mu_q$ measure is computed in a 3-D box expressed as:

$$\mu_q(s_1, x, y, z) = [f(x, y, z)]^q \qquad \ldots\ldots\ldots\ldots\ldots\ldots\ldots\ldots\ldots\ldots \quad (6)$$

$$\mu_q(s_2, x, y) = \left[ \sum_{x'=x-1}^{x+1} \sum_{y'=y-1}^{y+1} \sum_{z'=1}^{2} f(x', y', z') \right]^q \qquad \ldots\ldots\ldots\ldots\ldots\ldots\ldots\ldots\ldots\ldots \quad (7)$$

where, $x$ is the position in the x-direction, $y$ is the position in the y-direction, and $z$ is the elevation.

The measure $\mu_q\ (s_1,x,y,z)$ is essentially the reflectivity value of a pixel with coordinates $(x,y,z)$ in the radar image raised to a power $q$. The measure $\mu_q\ (s_2,x,y)$ derived at scale $s_2$ is eventually derived from a 2-D box which is explained further in the section.

To make the separation between the non-precipitation and precipitation echoes evident to a greater extent the multifractal exponent *K(q)* is computed in small windows of the radar image. To do so the ensemble average in equation *(4)* is approximated with a spatial average of the measures in small three-dimensional windows. The ensemble averages for the scales $s_1$ and $s_2$ are expressed as,

$$\left\langle \varepsilon_{s_1}^{q} \right\rangle_{x,y}^{\omega} = (1/2\omega^2) \sum_{x'=x-\omega/2}^{x+\omega/2} \sum_{y'=y-\omega/2}^{y+\omega/2} \sum_{z'=1}^{2} \mu_q(s_1, x', y', z') \qquad \ldots\ldots\ldots\ldots\ldots\ldots\ldots\ldots\ldots\ldots (8)$$

$$\left\langle \varepsilon_{s_2}^{q} \right\rangle_{x,y}^{\omega} = (1/\omega^2) \sum_{x'=x-\omega/2}^{x+\omega/2} \sum_{y'=y-\omega/2}^{y+\omega/2} \mu_q(s_2, x', y') \qquad \ldots\ldots\ldots\ldots\ldots\ldots\ldots\ldots\ldots\ldots (9)$$

where, *w* is window size. In this work two window sizes were selected: a 1x1x1 pixels window and 8x8x1 pixels window.

When using two scales the multifractal exponent *K(q)* in *(5)* is modified to

$$K(q) = \frac{\log\left\langle \varepsilon_{s_2}^{q} \right\rangle - \log\left\langle \varepsilon_{s_1}^{q} \right\rangle}{\log(s_2) - \log(s_1)} \qquad \ldots\ldots\ldots\ldots\ldots\ldots\ldots\ldots\ldots\ldots (10)$$

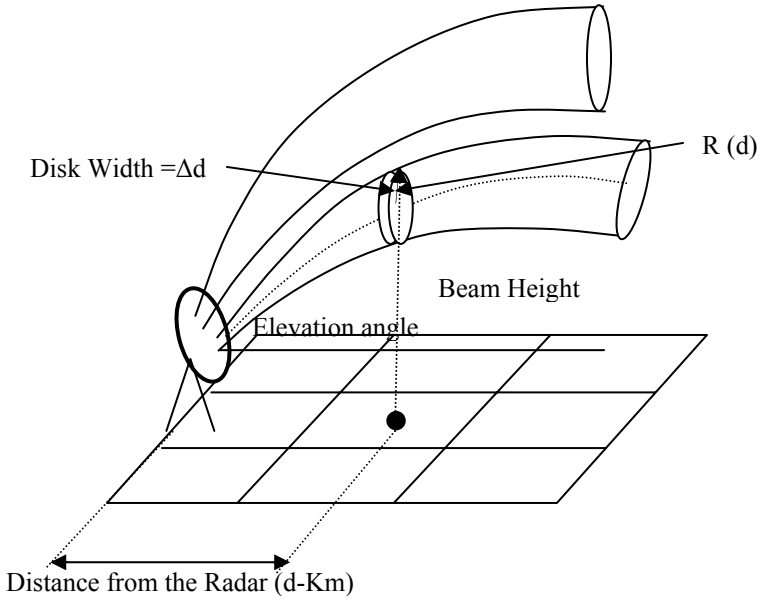


**Fig. 3.2 Radar volume scan**

The scale *s* can be related to the volume *(V)* of the three dimensional box as follows,

$$s = \sqrt[3]{V} \qquad \ldots\ldots\ldots\ldots\ldots\ldots\ldots\ldots\ldots\ldots (11)$$

and,

$$V = \pi \times R^2(d) \times \Delta d \qquad \ldots\ldots\ldots\ldots\ldots\ldots\ldots\ldots\ldots\ldots \quad (12)$$

where, $d$ denoted the distance from the radar ,$R(d)$ is the beam width at distance $d$ from the radar, and $\Delta d$ is the disk width of the radar beam as seen in Fig. 3.2.

Since the filter size used is 3 x 3, the number of pixels considered in every elevation is nine. The resulting equation after applying log to the above equation (11) becomes

$$\log(s_1) = (1/3)\log(\pi \times R^2(d) \times \Delta d) \qquad \ldots\ldots\ldots\ldots\ldots\ldots\ldots\ldots\ldots\ldots \quad (13)$$

$$\log(s_2) = 18 \times \pi \times R^2(d) \times \Delta d \qquad \ldots\ldots\ldots\ldots\ldots\ldots\ldots\ldots\ldots\ldots \quad (14)$$

where 18 represents the number of pixels considered from both elevations. Equation *(14)* can be written as follows,

$$\log(s_2) = (1/3)\log(18) + (1/3)\log(\pi \times R^2(d) \times \Delta d) \qquad \ldots\ldots\ldots\ldots\ldots\ldots\ldots\ldots\ldots\ldots \quad (15)$$

The difference between equation *(13)* and equation *(15)* is the constant *(1/3) log (18).* This proves that the exact knowledge of $s_1$ and $s_2$ is not required.

The multifractal QC algorithm computes the measures using two different powers, 2 and 8. The multifractal analysis yields four exponents corresponding to each scale and each power which are denoted as $K^{w}_{x,y}(q)$ where $w:(w_1, w_2)=(1,8)$ and $q:(q_1, q_2)=(2,8)$.

The flowchart in Fig. 3.2 depicts the final stages of the QC algorithm [1].

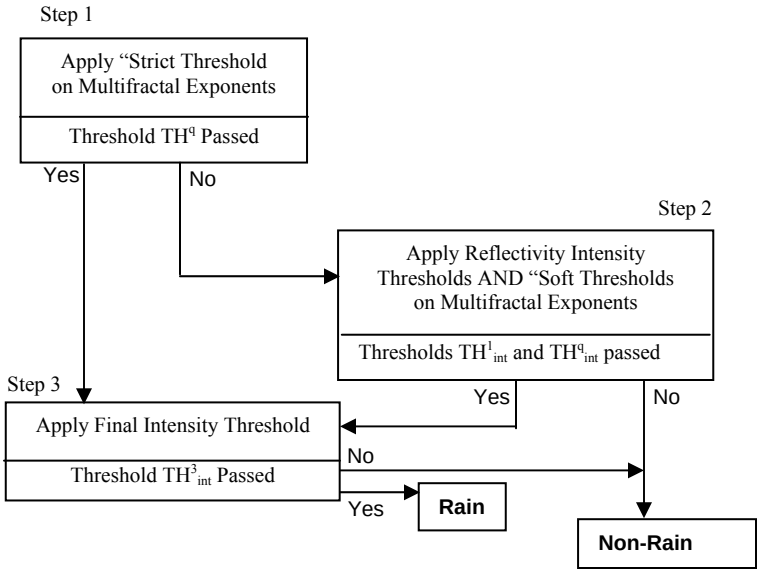


**Fig. 3.3 QC algorithm flow diagram**

*Step 1:* In this step each multifractal exponent is compared with a specific threshold. If any of the multifractal exponents have a value greater than the specified threshold the pixel is labeled as rain. These thresholds are crossover points of the histograms of rain versus non-rain events of the training images. These images are used with expert guidance that exactly identifies the areas of rain and non-rain.

*Step 2:* It is possible that the pixels which were actually rain were erroneously labeled as non rain. In step two a check is done to identify these pixels and to reactivate them. The original reflectivity image at elevation one is averaged by a window size of 20x20 and the center pixel value is compared with a specific predetermined threshold. Also, the original reflectivity image at elevation two is averaged by a window size of 5x5 and the center pixel value is compared with another specific predetermined threshold. If any pixel in any of the elevations has a value larger than the threshold the pixel is checked for each multifractal exponent value greater than the new respective 'soft' thresholds. In case the multifractal exponent value is smaller than the new thresholds the pixel is labeled as rain and reactivated. Again the thresholds are obtained from histograms of rain versus non-rain events in the training images.

*Step 3:* In this step non-rain pixels that were mislabeled by steps 1 and 2, are identified and eliminated. The thresholding in this step is applied only to the reflectivity image obtained from the lower radar elevation. This image is averaged by using a spatial filter of size 3x3 pixels and the center pixel value is compared with a noise threshold. If the pixel value is smaller than the threshold it is labeled as non-rain and eliminated.
The result is an image that shows the rain events with the non-precipitation echoes eliminated. This noise threshold is also evaluated from the training images.
Following Fig. 3.4 shows the raw radar images acquired at 02:19 hrs on March 31, 1999 at elevation 1. As seen it contains both the precipitation and the non-precipitation echoes, some of which are marked based on subjective analysis.

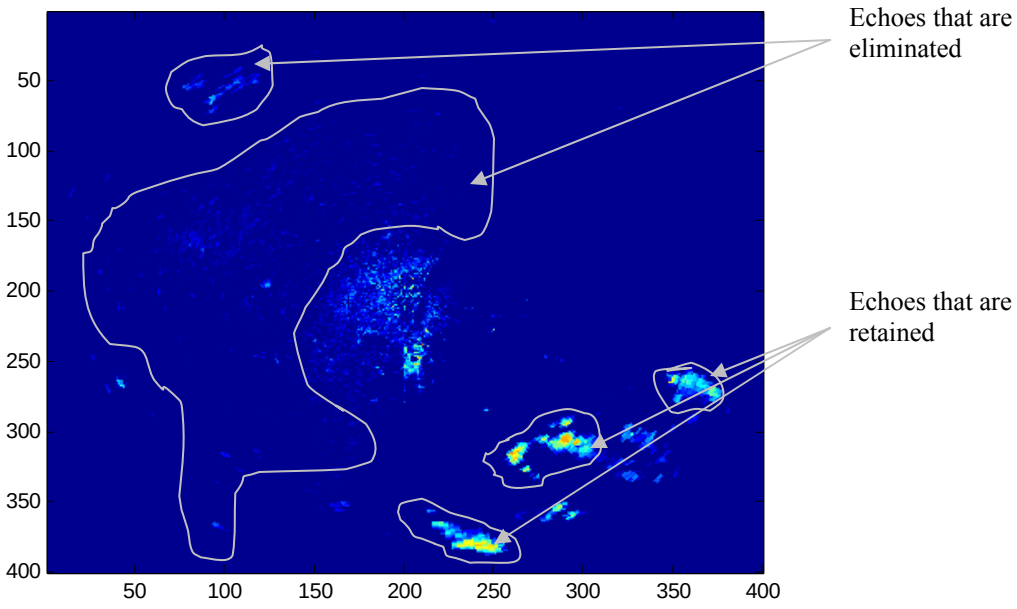


**Fig. 3.4 Original image at elevation 1**

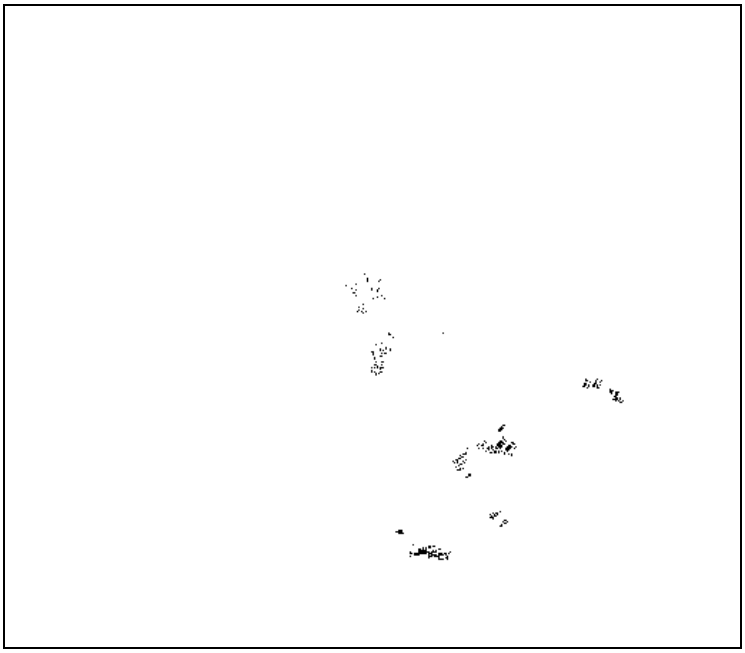

**Fig. 3.5 Result of Step 1**

**Fig. 3.6 Result of Step 2**

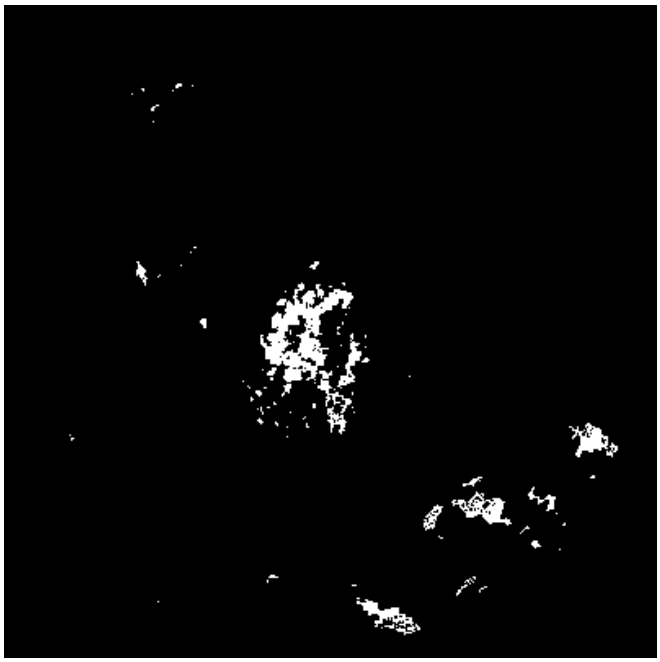

**Fig. 3.7 Result of Step 3**

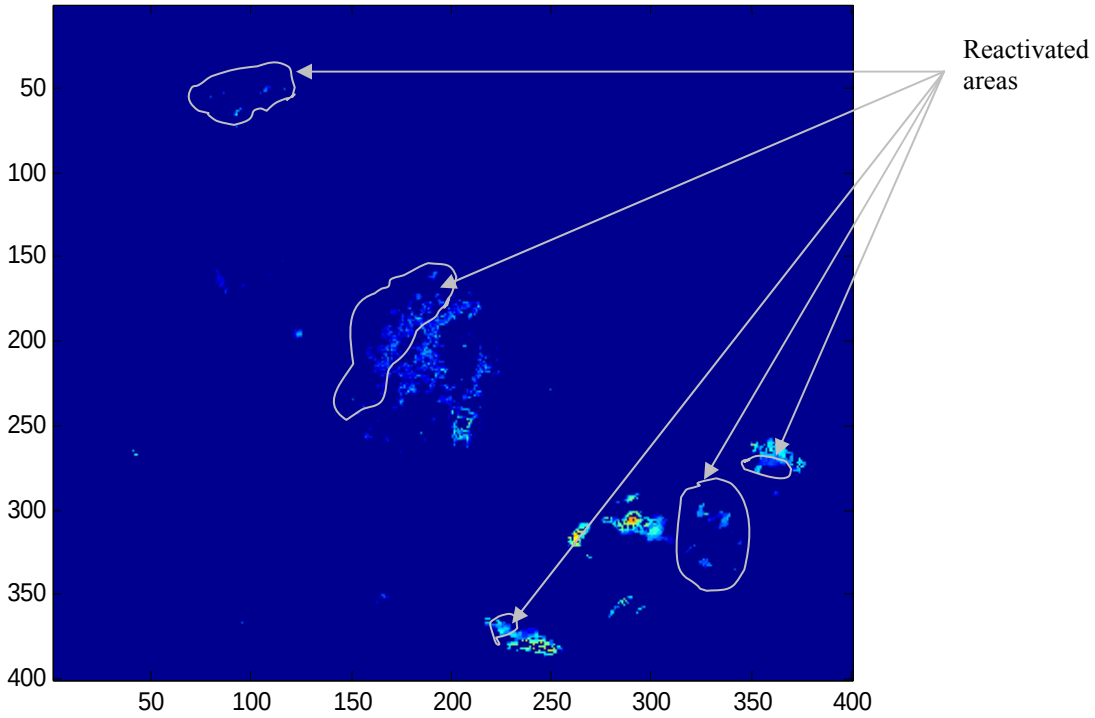


**Fig. 3.8 Final Result**

Figure 3.5 to 3.7 depict the intermediate results at various steps of the described process. Fig. 3.5 gives the results after the first thresholding in step 1. The white pixels are labeled as rain. Although, majority of the pixels are retained, due to values of the background pixels, this is taken care of in step 3. Fig. 3.6 shows the result after step 2. Although the difference is very difficult to view, some pixels that were eliminated as non-rain in step2 are reactivated back. Fig 3.7 depicts the results at the end of the last deactivation step. It can be clearly seen that most of the non-precipitation echoes are removed. Finally the last Fig. 3.8 shows the final result of the QC algorithm. The echoes that were identified by the QC algorithm as precipitation are marked in the original image given in Fig.3.4. Also, the marked areas also show the areas that are identified as non-precipitation echoes and eliminated by the QC algorithm, which can clearly be seen missing in the final result seen in Fig. 3.8. However, it should be understood that though the QC algorithm does remove or retain the pixels dependent on the values neither all actual rain pixels are retained nor all actual non-rain pixels are eliminated.

### *3.1.4. Proposed QC Algorithm*

Each of the QC algorithms described in the preceding sections 3.1.1-3.1.3 requires numerous parameters to optimize the performance of the QC algorithm. The QC algorithm described in Section 3.1.3 overcomes this limitation but uses average spatial filters which take into account the intensity of the textural features only. The presence of the sharp edges in these filters introduces high frequency components adding false information. Another very significant textual feature exhibited by the precipitation echoes in radar images is directionality. Directionality basically refers to the orientation of the echoes in certain direction. Exploitation of this aspect in radar images can better improve the detection of precipitation echoes. However, none of the aforementioned QC algorithms make an attempt to utilize this aspect of the radar images. The textural feature of the radar images is important for discriminating between precipitation echoes and non-precipitation echoes for the following reason. Non-precipitation events occur in a random fashion. This is due to the fact that they are dependent on various factors that do not have any structure. These factors are explained in section 2.1.3. As opposed to this, the

precipitation echoes occur in a more spatially correlated manner. This is because the cause of precipitation has a typical pattern as explained in section 2.1.2. Thus precipitation echo events exhibit a particular directionality in their texture. However the non-precipitation echoes do not demonstrate any such behavior. Thus the directionality of the precipitation echoes in the radar images enhances its distinction from non-precipitation echoes. The main motivation behind the development of the proposed algorithm was to exploit this feature in the texture of the precipitation echoes in radar images to achieve superior QC.

The idea is implemented by applying various directional wavelets to the radar images to better differentiate the precipitation echoes from other directionless non-precipitation echoes. The algorithm eliminates the use of average spatial filters assuring that no additional undesired information is introduced in the data.

#### *3.1.4.1. Gabor Wavelets*

Gabor wavelets have proven to be a very useful tool in image processing especially for the texture analysis and are widely adopted in the literature [17, 19]. They have been demonstrated to be very useful in detection of the texture direction. The major advantage of the Gabor wavelet analysis over the Fourier Transform is that it can achieve optimal direction in both spatial and frequency domain. The Gabor filters are band pass filters with tunable center frequency, orientation and bandwidth. The Gabor wavelets are a set of filters that have the ability to analyze the directional aspect of a given data. Properly tuned Gabor wavelets react strongly to specific texture and weakly to others. These basic characteristics of the Gabor wavelets served the purpose of the proposed algorithm, i.e. of exploiting the directionality of the radar images. A Gabor function is a Gaussian function modulated by an oriented complex sinusoidal signal.

A 2-D Gabor wavelet in the spatial domain is defined as:

$$g(x,y) = s(x,y)w_r(x,y) \qquad \ldots\ldots\ldots\ldots\ldots\ldots\ldots\ldots\ldots \quad (16)$$

where, $s\ (x,y)$ denotes the complex sinusoidal carrier and $w_r(x,y)$ is the 2-D Gaussian shaped envelop. The carrier $s\ (x,y)$ the envelop $w_r(x,y)$ are expressed as,

$$s(x,y) = \exp(j(2\pi(u_0 x + v_0 y) + P)) \quad \ldots\ldots\ldots\ldots\ldots\ldots\ldots\ldots\ldots\ldots (17)$$

$$w_r(x,y) = K \exp(-\pi(a^2 (x-x_0)_r^{\,2} + b^2 (y-y_0)_r^{\,2})) \quad \ldots\ldots\ldots\ldots\ldots\ldots\ldots\ldots\ldots\ldots (18)$$

As evident from the equations (16) to (18) the complex Gabor wavelet can be defined by using the following nine parameters,

***$(u_0, v_0)$*** denotes the spatial frequency in the Cartesian coordinates

***$(x_0, y_0)$*** denotes the peak of the function

***P*** is the phase of the sinusoidal carrier

**a, b** are the scaling parameters of the Gaussian in (3)

**θ** is the rotation angle of the Gaussian envelope

**r** subscript stands for a rotation operation such that,

$$(x-x_0)_r = (x-x_0)\cos\theta + (y-y_0)\sin\theta \quad \ldots\ldots\ldots\ldots\ldots\ldots\ldots\ldots\ldots\ldots (19)$$

$$(y-y_0)_r = -(x-x_0)\sin\theta + (y-y_0)\cos\theta \quad \ldots\ldots\ldots\ldots\ldots\ldots\ldots\ldots\ldots\ldots (20)$$

The following Fig. 3.9 depicts a Gabor wavelet of size 21, scaling parameters x and y direction as 8 and 2 respectively in three different orientations ***(θ).***

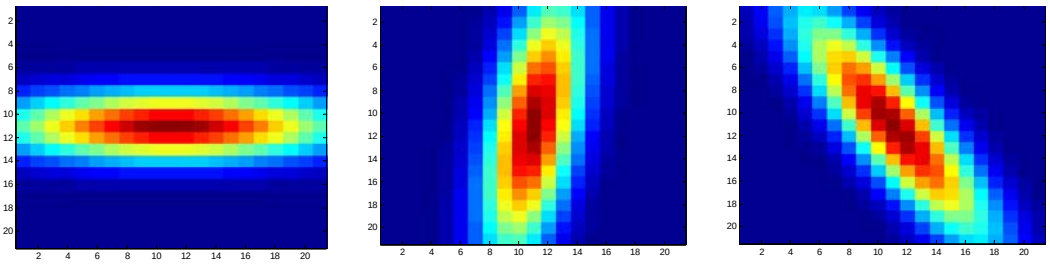

***(a) θ = 0 º*** ***(b) θ = 30 º*** ***(c) θ = 45 º***

**Fig. 3.9 Gabor filter at different orientations**

In this thesis the Gabor wavelets are used at different orientations to analyze the radar images. It is obvious that, the process would produce a large response when the wavelet is more finely tuned to frequency and orientation characteristics of the echoes. Thus, the Gabor wavelet tuned at optimal settings would exploit the directionality of

precipitation echoes present in the radar images. The approach was to use the Gabor wavelets in conjunction with the multifractal analysis to characterize the directionality of the texture of the radar images. The obtained textural information would aid in a more comprehensible distinction between the precipitation and the non-precipitation echoes.

Gabor wavelets with optimal set of orientations were used to filter the radar images. These filtered results were then used further to compute multifractals. Echoes which were oriented with a particular wavelet would give better response.

The replacement of the spatial average filter by a Gabor wavelet and Gaussian filter also eliminated the high frequency components that were introduced by the averaging square filter. This is a result of the smoothness due to the absence of sharp edges in the Gabor and Gaussian filter

### *3.1.4.2. The Proposed QC algorithm*

The proposed QC algorithm uses similar multifractal analysis as used in the QC algorithm in [1]. The computations of the two scales used for the construction of the multifractals are very similar to that of the previous algorithm. However there are some modifications that have been implemented to extract more useful information that can help better discriminate between precipitation echoes and non-precipitation echoes. The proposed QC algorithm uses Gabor wavelets to exploit the directionality in the precipitation echoes. It then applies multifractal analysis for scale-invariant characterization of radar images. The proposed QC algorithm uses two different scales to extract the textural information in the radar images. The radar images used are acquired from two elevations. The multifractal behavior in the radar images is characterized by multifractal exponents. The multifractal exponents at each scale are computed and used to categorize a pixel as rain or non-rain. The description of the process involved at the two scales is given below and the corresponding flowchart depicted in Figs. 3.10 and 3.11.

*Scale 1* (Refer to Fig. 3.10)*:* This scale is used to enhance the local irregularities in the textures of the images. Every pixel in the radar images at the elevation 1 (Im1) and

elevation 2 (Im2) is raised to a power q. These images are placed one over the other to form a 3-D box then convolved with the Gabor wavelet (denoted as Gabor (θ) in Fig. 3.10) at different orientations instead of a simple average filter as described in [1]. The result at every orientation (M1) is eventually used to compute a multifractal exponent *K(q)* as described in section 3.1.3.3. From section 3.1.3.2 we are well acquainted with the fact that the non-precipitation echoes have larger variability than a rain event. Also, a rain event doesn't show sudden changes in values. They rather, vary uniformly over a certain area. It was observed that depending on the type of echoes and their directionality, the multifractals will consequently have lower values for non-precipitation echoes while the rain echoes will have high values. However, this would not be the case for all multifractals as it also depends on the direction of the different echoes. The basic difference between the proposed QC algorithm and the QC algorithm mentioned in section 3.1.3.2 is the replacement of the average filter by Gabor wavelets. Also, unlike a single multifractal exponent obtained in the previous QC algorithm, a multifractal exponent corresponding to every orientation is obtained in the proposed QC algorithm.

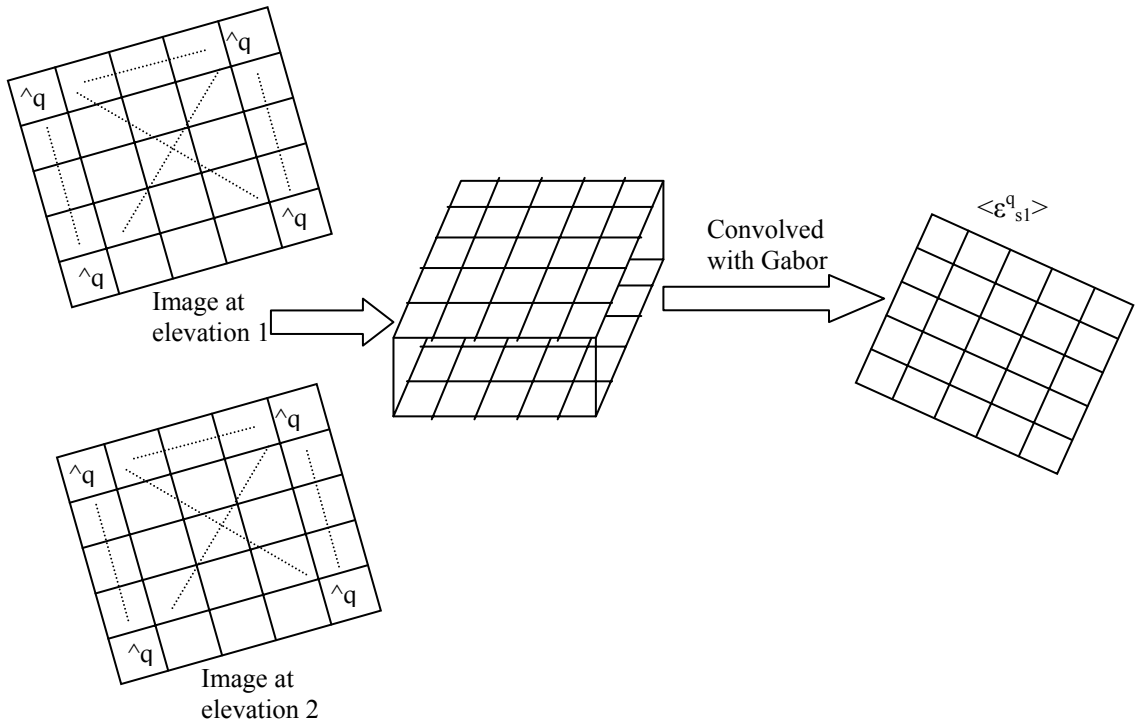


**Fig. 3.10 Steps in Scale 1**

Scale 2 (Refer to Fig. 3.11): In this scale the variation of the texture over a larger area, i.e. the global distinction of the texture, is obtained. As seen in Fig.3.11 the images at two lower elevations (Im1 and Im2) are added together and the result is filtered with a Gaussian filter (denoted as Gaussian in the flowchart in Fig.3.12) instead of the average filter described in section 3.1.3.3. The lower radar elevation image depicts non-rain echoes to a greater extent than the radar image at higher elevation. Although, most of the non-rain echoes visible in the lower elevation are eliminated in the higher elevation, there is a high possibility of certain rain echoes being absent in it. Hence, the two elevations are combined together so that the resulting image has values contributed by both elevations. Also, it is considered that rain reflectivity values do not have abrupt alteration [1]. Hence, to enhance this characteristic a small Gaussian averaging window of size 3x3 is used. The advantage of using a Gaussian filter is that, unlike the averaging filter in QC algorithm in mentioned in section 3.1.3.2 is that, it does not artificially introduce any high frequency components into the output due to its smooth edges. Thus it reduces the chances of erroneous results.

The resulting image is then raised to the power q to enhance the variation of the values. This is then filtered using a Gabor wavelet with same set of orientations as used for scale 1. The result would eventually produce a multifractal (M2), which would make the discrimination between the rain and non-rain event more evident. Fig.3.11 depicts the steps that are involved in computing the ensemble average.

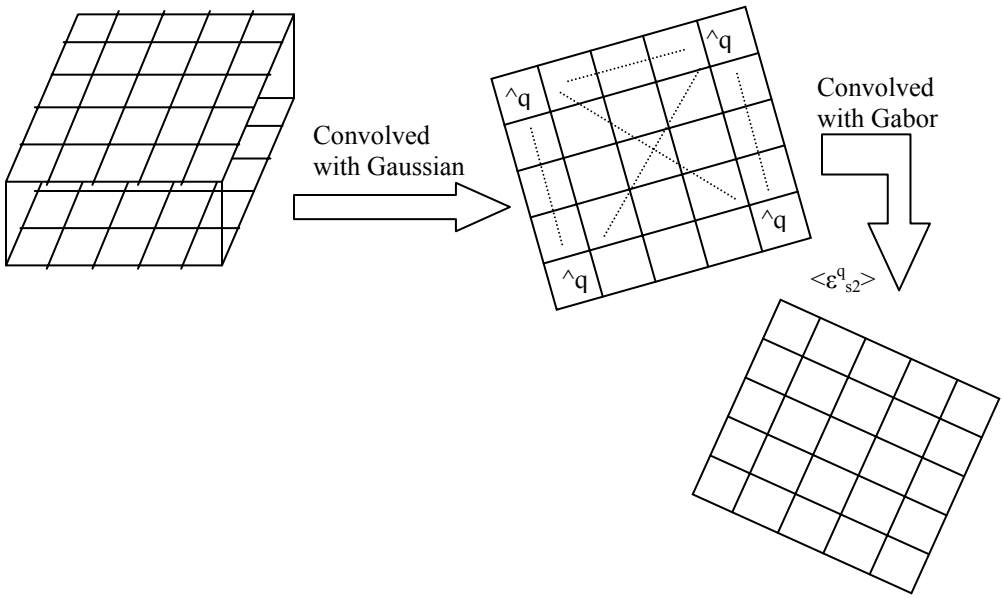


**Fig. 3.11 Steps in Scale 2**

A local multifractal (L1 and L2) is obtained by filtering the images obtained at each scale using a 1x1x2 average filter to produce the local information in the two radar elevation images. As apparent from the preceding section another set of multifractals (M1 and M2) is obtained as result of the filtering using Gabor filter for each orientation. The flowchart in Fig. 3.12 summarizes the process.

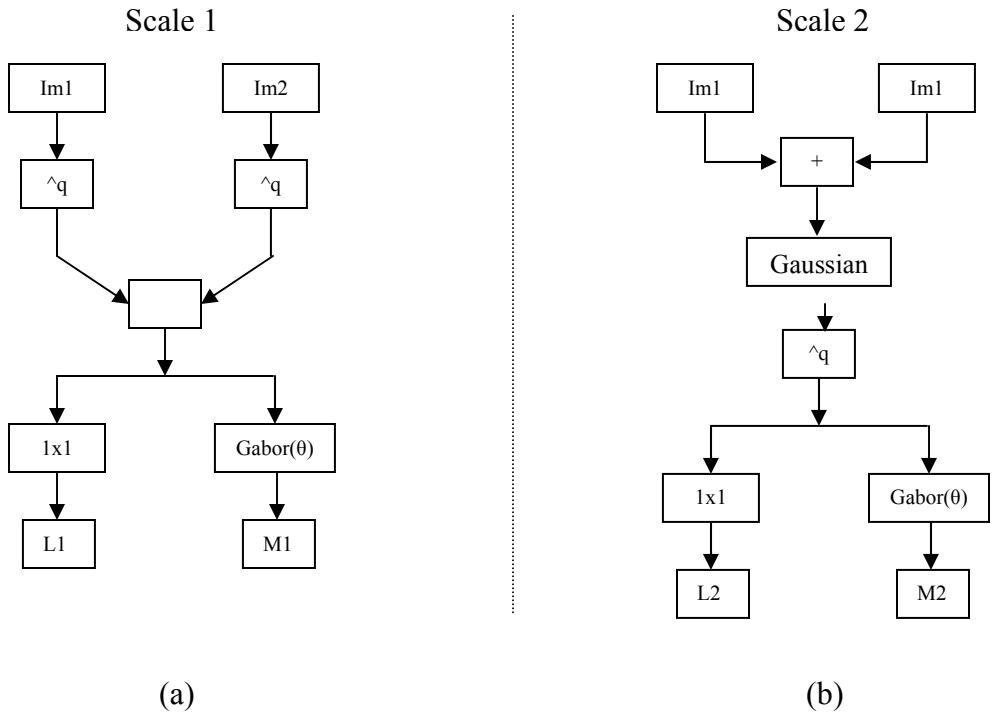


**Fig. 3.12 Flowchart of steps at scales**

It was observed that each multifractal enhanced the difference between rain events and the non-rain events depending on the orientation of the Gabor filter. It was a difficult and a complex task to extract out the best multifractal to be further used. Hence, a new concept of computing a maximum multifractal was applied. This can be supported by the fact that the nature of the precipitation echoes would result in the multifractal exponents having a relative larger value as compared to the non-precipitation echoes. This is unlike the QC algorithm in [1] which does not use such a concept as it does not involve multiple orientations. A maximum multifractal is essentially the multifractal, which contains only the maximum values amongst the multifractals obtained for all the orientations. This multifractal still retains the characteristics of the radar images that are necessary for the rain and non-rain discrimination.

After the computation of the multifractal exponents i.e. local as well as the Gabor filtered multifractals, they are passed through different thresholding steps. The decision is based on the textural multifractal exponents as well as the intensity data from reflectivity images. The original reflectivity images are also passed through some of these

thresholding steps. The QC algorithm uses this combined information and makes a decision at the end of every step. This decision results in a pixel being identified as either rain or non-rain.

After the development of the algorithm the subsequent segments comprised of two main parts which are the training and the testing of the algorithms. The database used constituted of radar reflectivity images which were acquired on March 31, 1999 from the site Melbourne, Florida. It was a typical day which comprised of varying degree of rainfall over the 24 hours. The following sections provide a detailed description of the training stage involved in development of the algorithm.

*3.1.4.3. Training*

Training is a vital part of the algorithm development wherein selection of the different parameters is done to achieve best quality results. The advantage of training is the reduction of the algorithmic complexity. The choice of the parameters is a trade off between the quality of the results and the complexity of the algorithm. The training of the images for the proposed algorithm involves computation of the optimal thresholds for the different steps, optimal parameters for the Gabor filter. The training set consisted of five images which were randomly chosen from the data base. All the images had varying amount of precipitation which assisted to improve the robustness of the algorithm. The training set consisted of the 5 images acquired at the following hours: 01:09hrs, 06:09hrs, 10:09 hrs, 18:09 hrs, 23:09 hrs shown in the order 1 to 5.

The thresholds are determined based on the normalized histograms of the two multifractals i.e. local multifractals and the maximum multifractal. First the histograms for the rain and the non-rain events were computed from the multifractal exponents. The histograms are estimates of the probability density functions of the two multifractal exponents. The performance of the proposed algorithm was evaluated by evaluating how well the two histograms were separated from each other. For this evaluation the following two techniques were used.

*3.1.4.4. t-test*

The t-test is commonly used for statistical analysis. It is used in this thesis to evaluate the performance of the proposed algorithm. The t-test is used to determine whether there is a significant difference between the means of two samples. Usually the test works well for normally distributed data, which is not strictly the case in the thesis. However, we conveniently assumed that the samples in this case are normally distributed.

The t-value, which deter mines the degree of separation between the two samples, is defined as:

$$t = \left| \frac{(\mu_1 - \mu_2)}{\sqrt{(\sigma_1^2 + \sigma_2^2)}} \right| \qquad \text{.....(21)}$$

where, $\mu_1$ and $\mu_2$ are the means of the two distributions and $\sigma_1^2$ and $\sigma_2^2$ are the standard deviations of the two distributions.

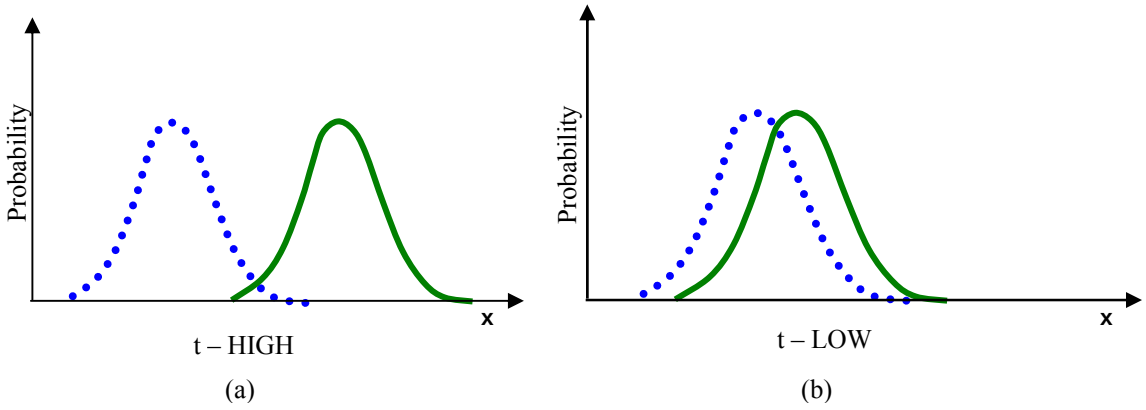


**Fig. 3.13 Examples of distributions**

The distribution shown in Fig 3.13(a) has less overlap which denotes that both of them have significantly different means. However, in Fig. 3.13(b) the two distributions have a high overlap due to closely similar means. Thus, the t-value gives a measure of the difference between the means of two distributions. A smaller t-value signifies a higher overlap while a higher t-value reflects a greater separation between the two distributions. This is the measure used to evaluate the separation between the normalized histograms of the rain and the non-rain events.

*3.1.4.5. Receiver operating characteristics (ROC) test*

ROC curves are commonly used in the field of communications to estimate the ability of a feature to discriminate between the data samples of two classes ($c_1$,$c_2$). The classifier employs a hard threshold to classify this data. If $x^*$ is the threshold used to compute the probability of a sample belonging to any of the above class then, the following four probabilities exist,

$P(x > x^* \mid x \in c_2)$: a hit, *i.e.* a data sample of $c_2$ is classified as that of $c_2$.
$P(x > x^* \mid x \in c_1)$: a false alarm, *i.e.* a data sample of $c_1$ is classified as that of $c_2$.
$P(x < x^* \mid x \in c_2)$: a miss, *i.e.* a data sample of $c_2$ is classified as that of $c_1$.
$P(x < x^* \mid x \in c_1)$: a correct rejection, *i.e.* a data sample of $c_1$ is classified as that of $c_1$.

The ROC curve is computed by increasing the threshold $x^*$ from the start of the $c_2$ range to its end and plotting the correct rejection rate against the miss rate. Accordingly, the curves for the three different cases are shown in Fig.3.14. The y-axis in the ROC curves represents the probability of correct rejection. This is the probability that a sample belonging from class $c_1$ is correctly identified and rejected as not belonging to class $c_2$.

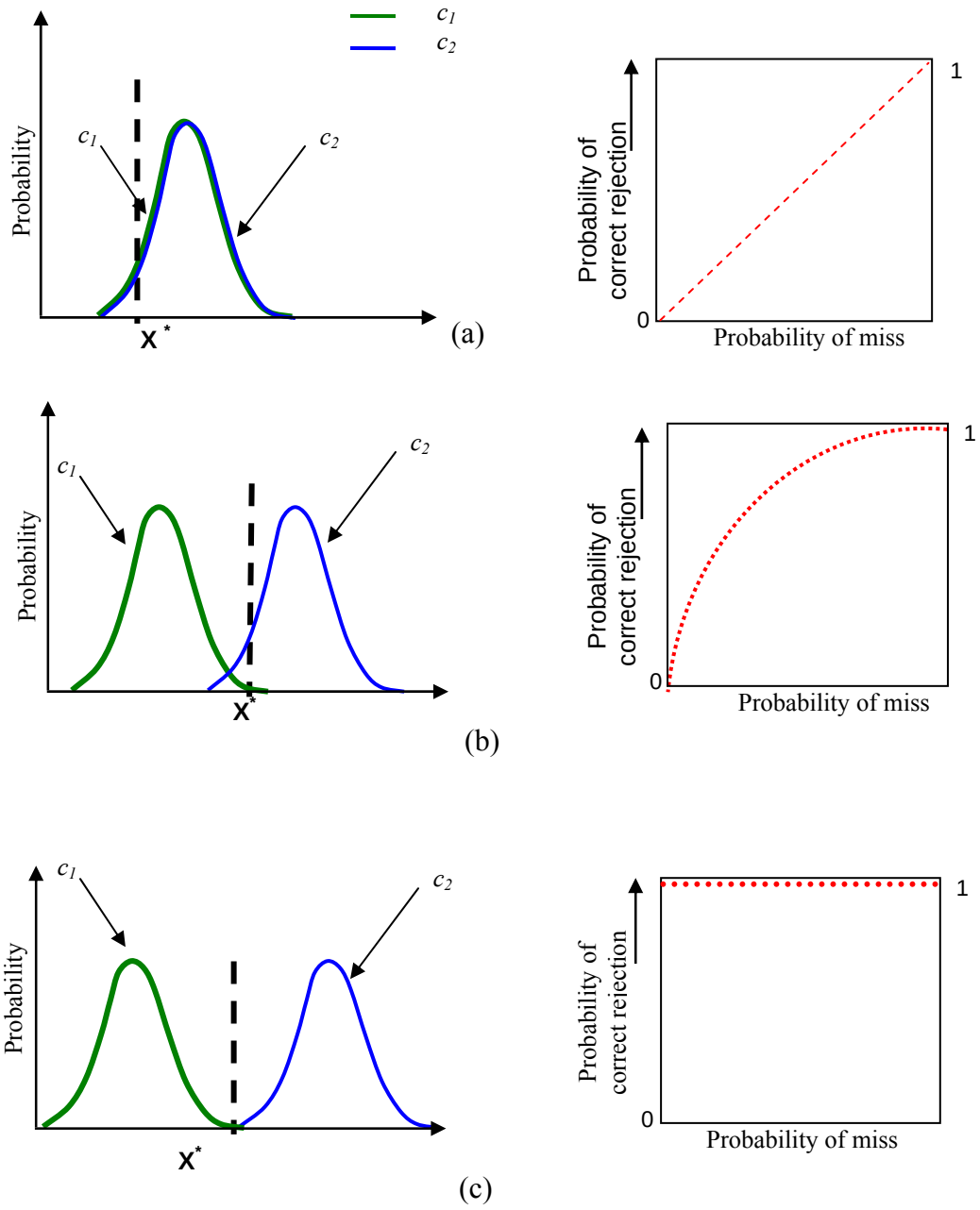


**Fig. 3.14 Different ROC curves (a) Case 1 (b) Case 2 (c) Case 3**

The classes in Fig.3.14 (a) show a complete overlap resulting in the ROC curve being a straight line. This is the worst case and the area under the ROC curve will have a value of 0.5. In other words the probability of a sample being actually from class $c_1$ but identified erroneously as from class $c_1$ *is 50%.* The case in Fig. 3.14 (c) shows no

overlap at all between the two classes. This is the best case and results in a ROC curve area of 1.0. Fig 3.14 (b) is an intermediate case wherein there is a partial overlap between the two classes resulting in a smooth ROC curve. Thus depending on the different cases the area under the ROC curve will vary between 0.5 to 1.0. In this thesis the value of the area under the ROC curve is desired as close as possible to 1.0 ensuring maximum separation between the two classes (histograms).

The above two tests were used to evaluate the training images. In other words evaluation was based on how well the histograms were separated. The normalized histograms for the five training images were computed for the local multifractal exponent and the maximum multifractal exponent. The average of all the normalized histograms was computed and the results are shown in Figs. 3.15 and 3.16.

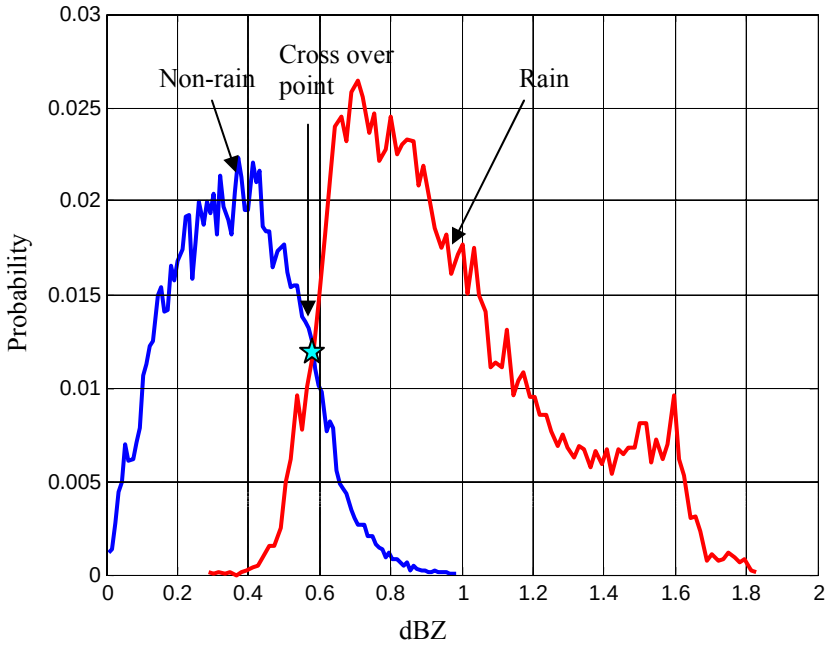


**Fig. 3.15 Normalized histogram for local multifractal exponents**

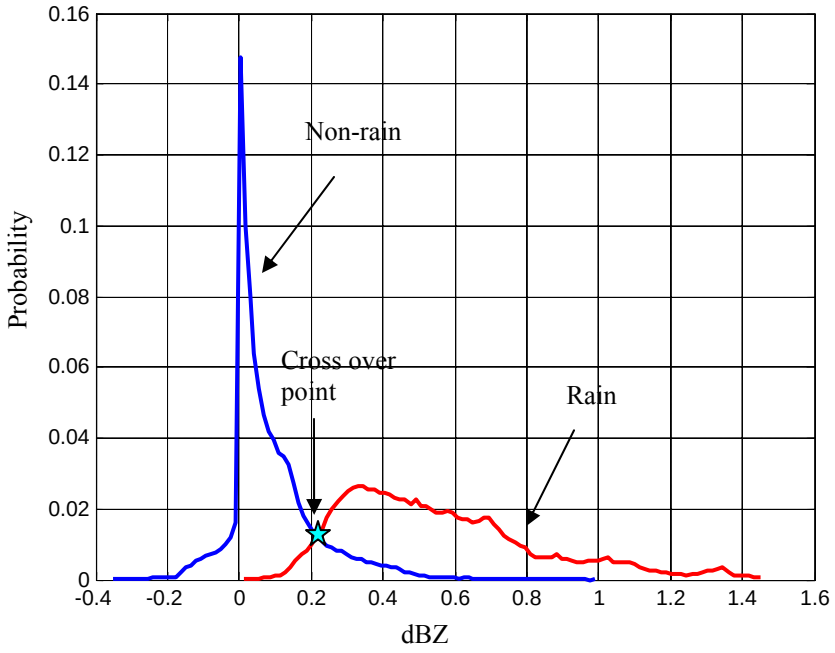


**Fig. 3.16 Normalized histogram for Maximum Multifractals exponent**

The blue curve represents the normalized histogram for non-rain and the red curve on the other hand represents the normalized histogram for rain. From Fig.3.15 and Fig.3.16 it can be observed that the two histograms in are well separated. This can be proved by the t-test values and the ROC values given in the table 3.2.

**Table 3.2 t-test and ROC values**

| Histograms | t-test value | ROC value |
|---|---|---|
| Local multifractal exponent | 1.726 | 0.957 |
| Max. multifractal exponent | 1.569 | 0.944 |
| Crossover | 0.582 | 0.216 |

As evident from the figures in Table 3.2 the t-test values, for normalized histograms of both the local multifractal exponent maximum multifractal exponent is acceptable. Also, the ROC values for the normalized histograms of the local and maximum multifractal exponent are very much closer to 1.0. These results verify the

adequate separation between the rain and non-rain events in the radar images. Thus it can be noticed that the multifractal exponents can discriminate between the precipitation and the non-precipitation echoes.

The normalized histograms are estimates of probability density functions of two exponents. Assuming that the occurrence of the rain and non-rain echoes has 'equal' probability the optimal threshold estimate is the one for which the probability density functions are equal. Thus the optimal threshold is the crossover point of the two histograms. Thus the strict thresholds used in the Step 1 over the multifractal exponents is chosen as the crossover points for both the local and maximum multifractal exponent. The relaxed thresholds in step 2 used for reactivation of the rain pixels are values chosen left of the crossover points on the left. This increases the probability of more rain pixels being reactivated. The thresholds used for the reflectivity images used in step 2 and the noise threshold used in step 3 are similar to those used in [1].

The thresholds used for neighboring pixel activation in step 4 were based on the fact that precipitation values occurred between 0-75dB. Hence, to avoid abrupt edges of the precipitation echoes detected in steps 1-3 the threshold chosen was a low value of 5 dB. The choice of the threshold in the last step 5 was a trade off as; in the centre area of 200x200 pixels the intensity was higher for non-precipitation echoes. However, they follow a random pattern and so a threshold that differentiates between the precipitation and non precipitation echoes within the area was chosen which was 0.12 dB.

**Table 3.3 Thresholds for different steps**

| ***Thresholds for steps*** | ***Multifractal exponents*** | | ***Reflectivity images*** |
|---|---|---|---|
| | *Local* | *Maximum* | |
| Strict | 0.6 | 0.2 | NA |
| Relaxed | 0.5 | 0.1 | |
| Reactivation of edge pixels | NA | NA | 4 |
| Clutter mask | NA | 0.12 | NA |

Table 3.3 shows the thresholds values that were chosen for multifractal exponents or reflectivity images for every corresponding step. Some of the cells are blank as not every step involves computation of threshold on multifractal exponents and the reflectivity images. For example the last step i.e. in the clutter mask removal the thresholding is done only on the maximum multifractal exponent and hence corresponding threshold is included. Thus, only the thresholds involving a particular image for every step is tabulated.

Another significant section of the training was the evaluation of optimal parameters for the Gabor wavelets.

**Table 3.4 Parameters values for Gabor wavelets**

| ***Parameters for Gabor wavelets*** | | | |
|---|---|---|---|
| *Size* | *Scale* | | *Steps of angles* |
| | x | y | degrees |
| 21 | 8 | 2 | 15 |

These parameters related to the Gabor wavelets were essentially the step changes in the orientations and the variances of the Gaussian window in both the x and y direction. The orientation step sizes were analyzed ranging from 1 degree to 30 degrees. The various combinations of the x and y direction variances, ranging from 2 to 20, were analyzed. After multiple attempts and satisfactory results the optimal set of parameters were chosen to be, an orientation step size of 15 degrees, variance in x-direction as 8 and variance in y-direction as 2. All these values corresponding to each parameter are clearly tabulated in Table. 3.4

A detailed description of different steps involved in the proposed QC algorithm follows below. Steps 1-3 are essentially similar to the steps used in QC algorithm in [1].

*Step 1:* After all the multifractals corresponding to the combination of the different filter orientation and the power '*q*' =2 are computed, they are passed through a strict

thresholding. These thresholds, $TH_1$ =0.6 dBZ and $TH_2$ =0.2 dBZ, are computed from the training process that is explained in section 3.1.4.3

*Step 2:* The possibility of an actual rain pixel being labeled as non-rain and eliminated in step 1 cannot be ruled out completely. The basic reason for this is the application of strict thresholds used in step 1. Hence, it is necessary to find and reactivate these pixels. This is done using the actual reflectivity images and the multifractal exponents.

A window p1 of size 20x20 is used to average the image obtained at first elevation and is compared with a specific threshold THint1 =25 dBZ. Another window p2 of size 5x5 is used for averaging the image obtained at the second elevation and the values below the threshold THint2 =20 are clipped. The choice of the window sizes is based on the nature of the precipitation echoes present in both the elevations. The precipitation reflectivity values are expected to be high and widespread in the first (lower) elevation as compared to that in the higher elevation. Thus a large averaging window is used. This is empirically chosen to be 20 based on the training data set. However, in the second (higher) elevation image, the precipitation echoes are lower and less widespread than the lower elevation image. Thus the size of the averaging window is smaller. This is empirically chosen to be 5 based on the training data set.

Hence, thresholding on the reflectivity images selects these pixels which have the probability of being precipitation echoes. These are then cross checked by comparing the pixels in the multifractal exponents with new thresholds TH1rex=0.5 and TH2rex =0.1 These thresholds are relaxed thresholds compared to the ones used in step 1. If any of the values in the multifractal exponent is smaller than these thresholds then the pixel at that particular location is identified as rain and is reactivated. Once again the thresholds are calculated from the normalized histograms of the rain and non-rain events.

*Step 3:* There is also a possibility that the pixels, which were actually non-rain, passed through the above steps and were mislabeled. To eliminate these pixels the lower elevation image is averaged using a window size 3x3 and is compared to a noise

threshold $TH^{int}_3$ =4. If the value is smaller than the noise threshold those pixels are identified as non-rain and are removed.

Step 4: Echoes belonging to rain event have smooth edges do not exhibit sudden changes. Therefore, the algorithm reactivates pixels neighboring the rain events. These pixels are identified and reactivated if they are greater than a particular threshold $TH^{n}_4$=5 dBZ. The threshold chosen is a little higher then the noise threshold used in step 3. This threshold needs to be low enough such that even the mild rain events surrounding the strong rain events are reactivated. However it should not be as low as the noise threshold, else the random noise surrounding the main rain event will also be identified as rain. Thus the threshold $TH^{n}_4$ was chosen to be 5 dBZ.

*Step 5:* It is observed that in many cases a lot of non-precipitation clutter is located in the center 200x200 pixel area. This clutter is inevitable and is present in almost all of the images. A lot of these events do have high intensity values and can be mistaken as rain. Thus, a lot of these clutter pixels are labeled as rain in the previous steps and it is important that these pixels be identified and deactivated. Hence, an additional step was included in the proposed QC algorithm. For these 200x200 pixels around the radar center, the multifractal exponents are checked for values less than a new threshold $TH^{clut}_5$ =0.12. If the pixels have values less than this threshold they are identified as non-rain and are eliminated to obtain the final product.

Step 5 yields the final image that comprises of only the rain events identified by the proposed QC algorithm. Fig.3.17 depicts the flowchart showing the different steps involved in the QC algorithm after the computation of the multifractal exponents.

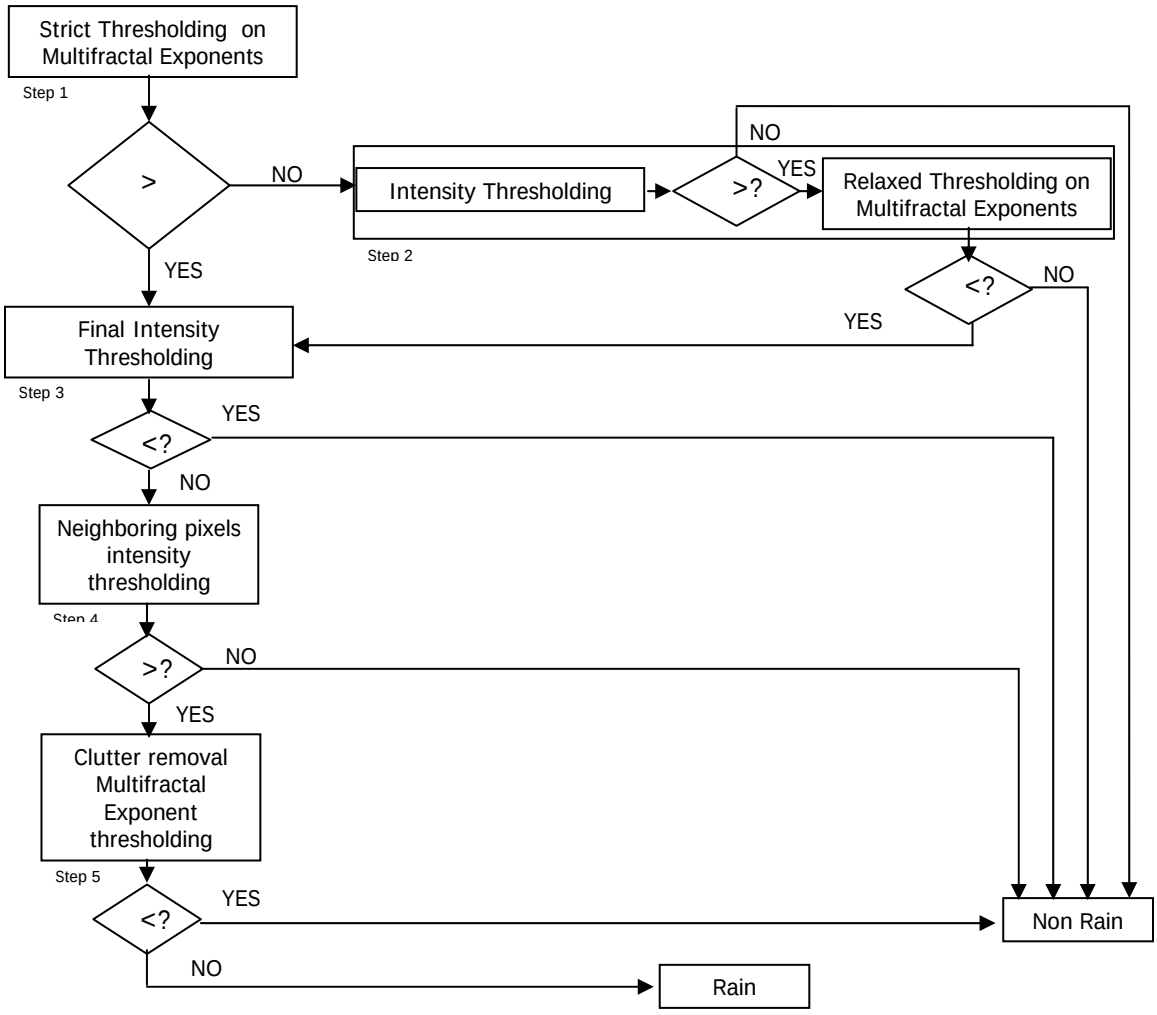


**Fig. 3.17 Flowchart after computation of multifractals.**

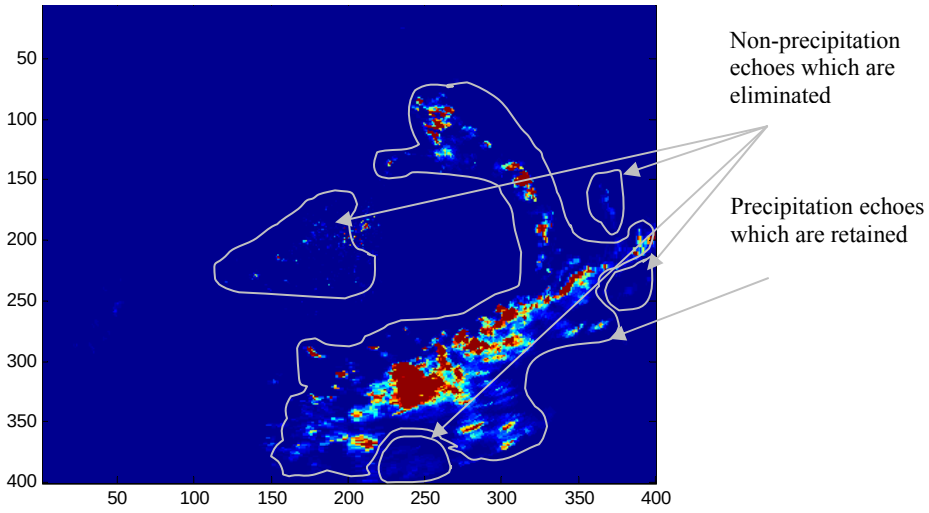


**Fig. 3.18 Original reflectivity image at elevation 1**

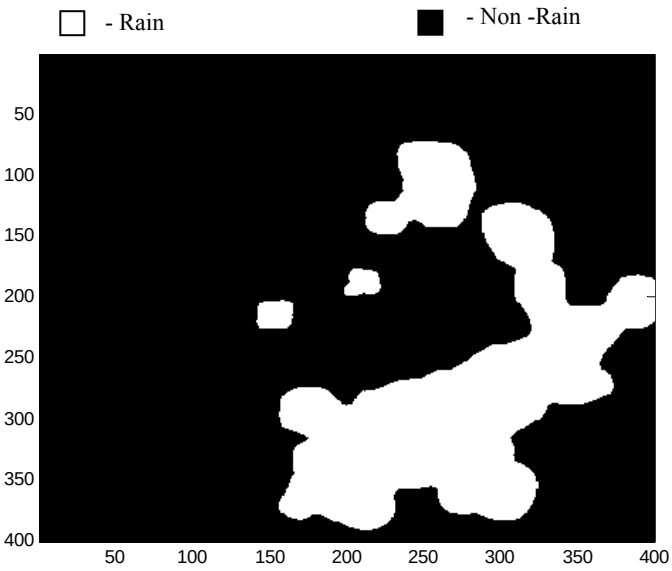


**Fig. 3.19 Output image after step 1**

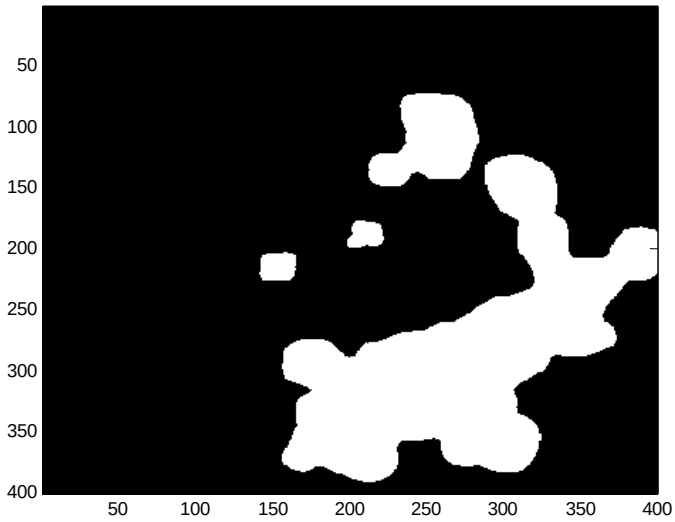


**Fig. 3.20 Output image after step 2**

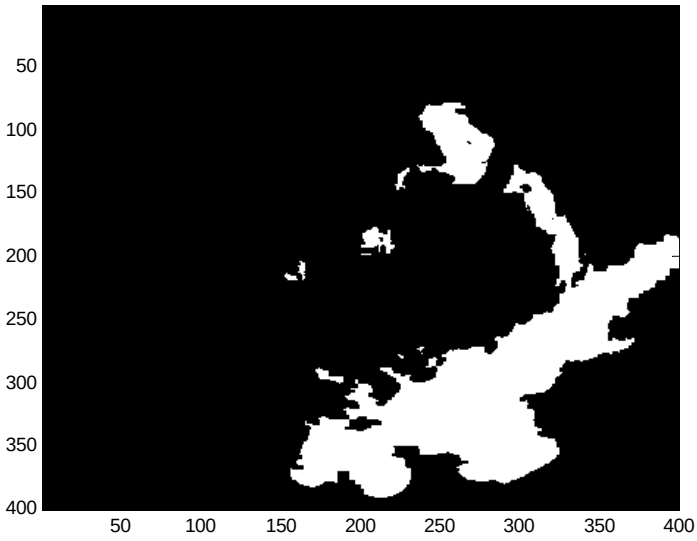


**Fig. 3.21 Output image after step 3**

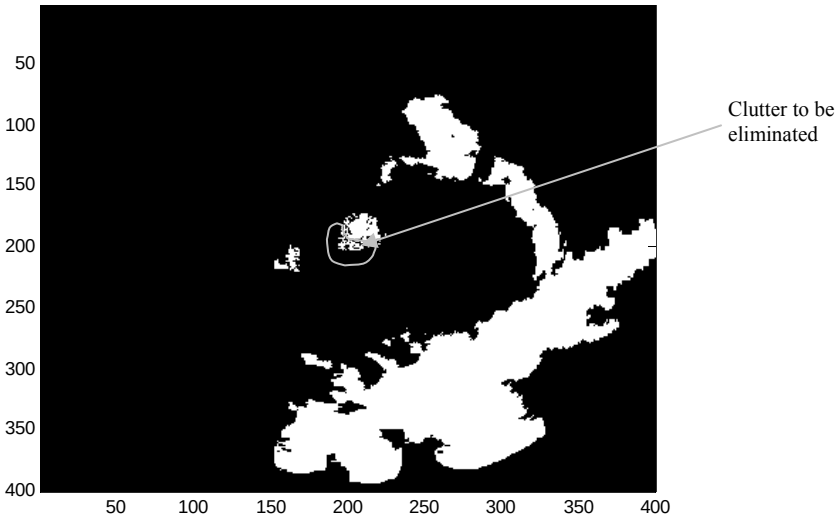


**Fig. 3.22 Output image after step 4**

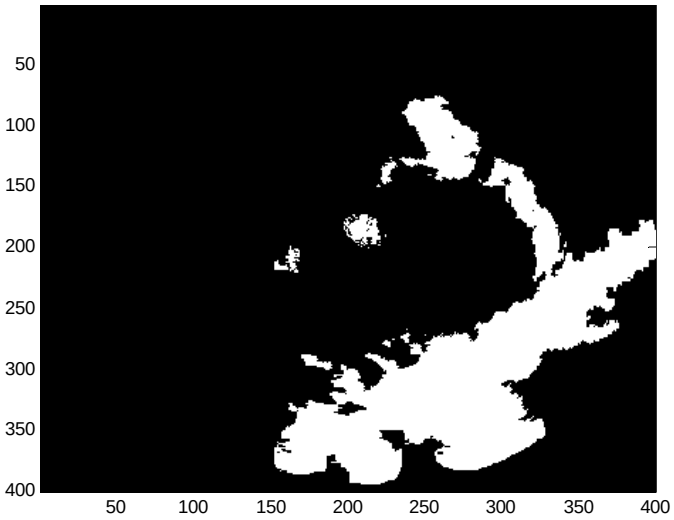


**Fig. 3.23 Output image after step 5**

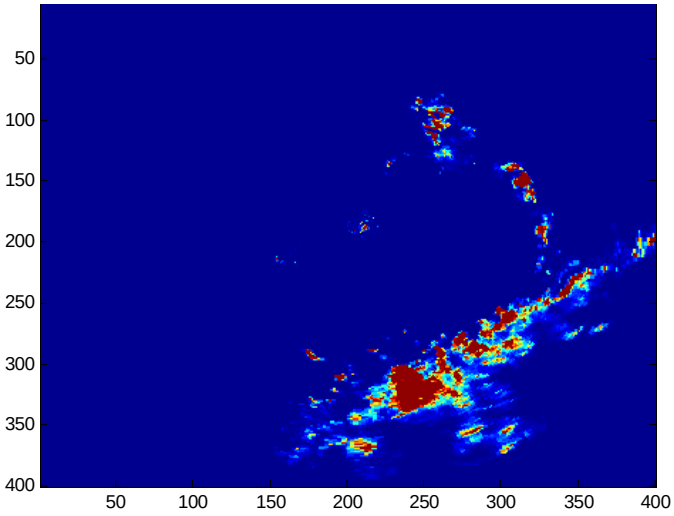


**Fig. 3.24 Final Output image**

Fig.3.18 shows the original reflectivity image obtained at 15:09 hrs on March 31,1999 at the lowest elevation. The precipitation and the non-precipitation echoes which are retained and eliminated respectively by the proposed QC algorithm are clearly marked in the figure. Figures 3.19 through 3.24 show the outputs at each step of the algorithm and the final output obtained. As explained before the image in step 1 is result of a hard thresholding done on the multifractal exponents. The result is depicted in Fig. 3.19 where the white areas are the ones identified as rain by the QC algorithm while the rest is labeled as non-rain. Result after the end of Step 2 which is pixel reactivation is depicted in Fig. 3.20. It can be seen that there is not much difference in the two images. The reason being the choice of threshold in step 1 due to which, most of the rain pixels are already chosen. Thus, very few pixels are left to be reactivated back in step2. The results at the end the final thresholding step 3 is given in Fig. 3.21 It is obvious that several pixels are eliminated as they are identified as non-rain in step 3. In Fig.3.22 it can be seen that the pixels surrounding the rain events are activated back in the image in step 4. The last step is the clutter removal step 5 in which the clutter pixels in the centre 200 x 200 area in the image are identified and eliminated. This result is given in Fig.3.23 and the pixels which were removed are marked in Fig. 3.22. Finally, the Fig. 3.24 shows the

image which is the final output of the proposed QC algorithm. The difference between the original reflectivity image in Fig.3.8 and the final processed image in Fig. 3.24 can clearly be seen. It can be observed that the non-precipitation echoes are removed while the precipitation echoes are retained. These are correspondingly marked in Fig.3.18

#### *3.1.4.6. Testing*

The testing set comprised of 15 images which were selected randomly from the database. None of these test images were the ones selected as training images. The images were selected so that the amount of precipitation ranged from low to high. Following list depicts the hours at which the test images were acquired.
02:09 hrs,04:09 hrs,05:09 hrs,07:09 hrs,08:09 hrs,11:09 hrs,12:09 hrs,14:09 hrs,15:09 hrs,16:09 hrs,17:09 hrs,20:09 hrs,21:09 hrs,22:09 hrs,24:09 hrs

##### *3.1.4.6.1. Evaluation of the Performance of the proposed algorithm*

The evaluation of performance of the proposed algorithm is done by comparing the accurate rain events with the results obtained by using each of the following algorithms

- the proposed QC algorithm : These are the results obtained by using the QC algorithm proposed in this thesis discussed in section 3.1.4.2
- the GVS (Ground Validation Software) : These are the results obtained by the QC algorithm used by the TRMM project discussed in section 3.1.2.1
- the QC algorithm in [1]: These are the results obtained by the QC algorithm described in [1] which is also discussed in section 3.1.3.2

As discussed before the images used for these evaluations were obtained from the NEXRAD site located in Melbourne, FL.

Although, a comparison can be made between the results of the GVS, QC algorithm in [1] and the proposed algorithm, it is understood that these results are not perfect. This implies that not all the non-rain is removed and not all rain is retained [1]. Hence, accurate rain events were computed on subjective analysis under expert supervision and all the three algorithm results were compared with the same.

The images worked on were taken from a set of radar images acquired on a particular day. Several images were chosen for the training and testing from the early and end hours of the day, which comprise of a varied amount of rainfall.

#### *3.1.4.6.2. Statistical Measures*

As subjective analysis of the results do not distinctly convey the performance of the proposed QC algorithm, some statistical measures were required for evaluation of the performance of the proposed QC algorithm. The a description of the statistical measures used for the analysis in the testing and training stages is given below;

[i] Errors:

Errors are classified in two categories as given below

- Misses:
  This measure gives the percentage of the pixels that were missed by the proposed QC algorithm. These are the number of pixels, which were identified as rain pixels by the accurate rain events but were missed by the QC algorithms.
- False Alarms:
  This measure gives the percentage of the pixels that were erroneously retained by the QC algorithms. It gives the number of pixels, which were identified as non-rain pixels by the accurate rain events but were detected as rain pixels by the other QC algorithms.

[ii] Accuracy

This measure evaluates the accuracy of the QC algorithms. It is the number of pixels, which are identified as rain or non-rain pixels in the accurate rain events and were respectively detected correctly as rain and non-rain pixels by the QC algorithms.

[iii]Signal to Noise Ratio

This is the usual signal to noise ratio of the results obtained by the QC algorithm as compared to the accurate rain events.

It is acknowledged that the significance of precipitation is directly proportional to the value of reflectivity. Thus, it is fair to evaluate the above statistical measure for different ranges of reflectivity values. Another, basis of this evaluation is that the reflectivity values less than 20dB do not contribute a lot to the rainfall whereas, greater values make a major contribution towards rainfall in the radar image. And hence, the ranges above 20 dB are of interest and are significant in evaluating the performance of the algorithm.

The testing images were processed using the proposed QC algorithm and the different statistical measures extracted. The statistical measures were also extracted for the results of the other two QC algorithms. All the results and the corresponding statistical measures are given in the chapter 5.

# CHAPTER 4

# 4. OPTICAL PROCESSING

## 4.1. Introduction

The roots of optical processing extend back to the late 1850's [26].1 Since then optical signal processing technology continues to grow at a rapid pace. The development of the laser in 1960 initiated a revolution in this field. The consequences of that revolution are still unfolding. Another application of optics signal processing is optical image processing. Vander Lugt [27, 28] introduced the first optical correlator in 1963 containing the spatial matched filter which opened the era of coherent optical image processing. Last decade has witnessed the development of the traditional area of optical information processing using Fourier optics. Hybrid optoelectronic systems that use optics and electronic comprise a powerful processing technology. The quality control algorithm proposed in this thesis is a combination of optical and digital processing

## 4.2. Advantages of Optics

Numerous advantages of light over the conventional electronic systems have enhanced the efficacy and the need for the optical system today. Following are listed the major benefits offered by the optical processing systems which give them an edge over electronic systems when it comes to image processing.

*High Speed:* The information in the optical systems is carried by photons. These photons have a very high information carrying capacity. They travel at the speed of light ($3 \times 10^8$ m/sec) thus transmitting the information encoded onto them at the same speed. This results in the processing taking place at the speed of light which is the major advantage of optical processing.

*Massive Parallelism:* In optical processing systems the entire pattern can be processed at the same time. The data encoded onto the photons is processed simultaneously at the same instant. Parallel processing can be implemented without a cost to computation time or complexity. This is much quicker as compared to the electronic systems where each pixel or picture element is processed sequentially. Also, different images can be processed simultaneously. This is definitely a vital feature since the processing time is minimized significantly.

*Real time:* Due to the features like higher bandwidth and connectivity of the optical systems many image processing can be implemented in real time. The NEXRAD acquires each image every 5 minutes. Hence, it is extremely necessary that the processing of an image is fully completed before the next image is acquired. The real time response of optical processing makes these systems more advantageous over their electronic counterpart.

*Design Complexity:* The optical processing is easy to realize once the optical setup is ready. Once the optical system is set up no new adjustments are necessary. The images can be simply loaded /unloaded changed and the processing takes place without any difficulty. The system involves simple and very low cost optical components which make its use very economic.

## 4.3. Optical Components

An optical processing system comprises of numerous components. This section discusses the different and important components encompassed in the optical system in the thesis.

### *Light Source*

In an optical system the information/data is carried by the light. There are different types of light sources available and the most common amongst all are the light emitting diodes (LED's), lasers, and laser diodes. The sources are chosen based on compactness, response speed, bandwidth, and application.

*Mirrors*

Mirrors are used to steer light beams. They can be flat or have curved surfaces designed to converge or diverge beams. The mirrors are employed to control the direction of the light beam.

*Beam Splitters*

Beam splitters are devices comprised of prisms or two-way mirrors used to split the incoming light beams into two directions or combine incoming beams into a single beam. These optical devices control the flow of light in an optical system.

*Lenses*

The lenses are an integral part of any optical system. Converging lens can perform two main tasks:

a) Collimation of the light beams: The lenses are used to collimate the light beams so as to focus them in the desirable direction in an optical system.

b) Compute the 2-D Fourier transform and in its inverse transform: This is one of the properties of the lens that make them significant in optical systems used for image processing. It forms the basis for most of the analog optical processing

A converging lens when placed at a distance of focal length from an image produces its Fourier transform at a distance of one focal length away from the lens. Fig 4.1 depicts this property of the lens. The transparency has the input image $p(x,y)$, loaded onto it. When the light beams from the coherent light source with wavelength $\lambda$ passes through the transparency, it is modulated by the contents of the transparency resulting in the image encoded on the light beam.

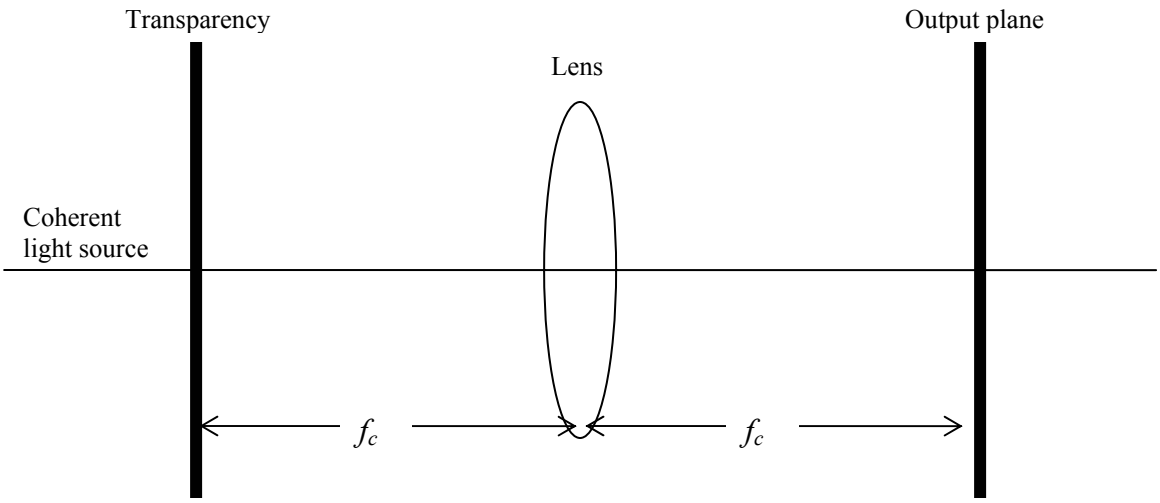


**Fig. 4.1 Fourier transform property of a lens**

When light beam passes through an ordinary converging lens it is integrated and converged onto the focal point on the output. The lens acts as a phase element causing a phase delay in each segment of light. This phase delay is dependent on the thickness of the lens. This effect is equivalent to a linear phase factor present in the integral form of the corresponding Fourier transform. Thus the combined effect of the phase factor on the corresponding integral generates the effect similar to that of Fourier transform on the input.

This operation can be mathematically expressed as follows,

$$P(x_2, y_2) = A \int_{-\infty}^{\infty} \int_{-\infty}^{\infty} p(x_1, y_1) \exp\left[ -j \frac{2\pi}{\lambda f_c} (x_1 x_2 + y_1 y_2) \right] dx_1 dy_1 \quad \text{.....(21)}$$

where, $A$ is the amplitude of the wave, $\lambda$ is the wavelength of the light, $f_c$ is the focal length of the lens, $P$ is the image, $x_1, y_1$ are the coordinates in the x and y -direction respectively of the input image and $x_2, y_2$ are the coordinates in the x and y -direction respectively of the output image. The following variables are defined:

$$u = \frac{x_2}{\lambda f_c} \quad \text{.....(22)}$$

$$v = \frac{y_2}{\lambda f_c} \quad \text{.....(23)}$$

By substituting the Eq. (22) and (23) in Eq. (21) and assuming a normalized wave amplitude the P observed at the output plane can be expressed

$$P(u,v) = A\int_{-\infty}^{\infty}\int_{-\infty}^{\infty} p(x\ ,y\ )\exp\left[-j2\pi(xu+yv)\right]dxdy \qquad \text{……...……..(24)}$$

Eq. (24) is actually a 2-D Fourier transform.

Thus, light source when placed at the focal point $f_c$ of a converging lens can be used to collimate light beams passing through it. Also, converging lens can perform the 2-D Fourier transform and its inverse transform.

*Spatial Light Modulator (SLM)*

The SLM is an optoelectronic input device for the optical processing system. The SLM essentially acts much like a transparency that encodes the input data on the light beam. The data are loaded onto an SLM and the intensity of the pixels of the SLM modulates the frequency of this light that passes through the SLM. In other words, in case of intensity SLM the amount of modulation of the light is determined by the write image intensity at the corresponding pixel on the SLM. The SLM's are available in single pixel one-dimensional (1-D), 2-D (2-D) or three-dimensional (3-D) based on the requirement of the system. The modulation of light by the SLM's is obtained by exploiting several different parameters like intensity, phase, polarization and spatial frequency. Different types of SLM's are available amongst which few common 2-D SLM's are: Liquid Crystal Television (LCTV), Magneto-optic SLM (MOSLM), and Deformable Mirror Device (DMD) [26].

*Charged Coupled Device (CCD) Detector*

The CCD detector is also known as a square-law device. It uses an array of light detectors for recording optical input and converting it to an electronic signal. This output can then be stored digitally in storage devices like computers. The SLM and the CCD detector provide the interface between the electronic and optical systems.

Thus, the SLM and the CCD together provide an interface between the optical and the electronic systems. The hybrid use of optics along with the electronic system helps achieve an optimal operation in terms of performance, speed and cost.

## 4.4. Joint Transform Correlator (JTC)

Optical correlaters are designed to perform the correlation between two input patterns optically. The Vander Lugt correlator requires the generation of complex valued input data and require meticulous alignment along the optical axis. The Joint Transform Correlator (JTC) is an improvement over such correlators since all input is generated in the spatial domain and there is no need for multiple optical components that require strict alignment conditions.

In a JTC, the two images to be correlated - referred to as the target image *t(x,y)*and the reference image *r(x,y)* - are placed side by side in the same input plane with a separation between them,. The joint image *f(x,y)* comprising of these two images can be represented by the equation below,

$$f(x,y) = r(x, y - y_0) + t(x, y + y_0) \quad \text{.....(25)}$$

where the displacement between the two images is $2y_0$.

Then the 2-D Fourier transform *F(u,v)* of the input joint image *f(x,y)* is expressed as,

$$F(u,v) = \Im\{f(x,y)\} = T(u,v)\exp[-jy_0v] + R(u,v)\exp[jy_0v] \text{.....(26)}$$

$$= |R(u,v)|\exp[\phi_r(u,v)]\exp[jy_0v] + |T(u,v)|\exp[\phi_t(u,v)]\exp[-jy_0v]$$

$$\text{.....(27)}$$

where, $|R(u,v)|$ and $|T(u,v)|$ are the magnitudes of the reference and the target images respectively. The phases $\phi_r(u,v)$ and $\phi_t(u,v)$ are the phases of the Fourier transforms of the reference and the target images respectively. As the CCD is a square law device it captures the intensity of the output. Then the intensity of the Fourier Transform defined in Eq. (26) known as the joint Power Spectrum (JPS) is given as,

$$G(u,v) = |F(u,v)|^2$$

$$= |R(u,v)|^2 + |T(u,v)|^2 + 2|R(u,v)|^2|T(u,v)|^2 x\cos[\phi_r(u,v) - \phi_t(u,v) + 2vy_0]$$

……..(28)

The inverse Fourier transform (IFT) of the JPS in equation (28) is the correlation output and is given as,

$$c(x,y) = r(x,y) \otimes r^*(x,y) + t(x,y) \otimes t^*(x,y) + r(x,y-2y_0) \otimes t^*(x,y-2y_0) + r^*(x,y+2y_0) \otimes t(x,y+2y_0)$$

……..(29)

where, $\otimes$ denotes the correlation and * denotes the complex conjugate.

As can be seen from equations (28) and (29) the first two terms in the JPS represent the autocorrelation terms in IFT i.e. equation (29). Also the cosine term in the JPS converts into two cross-correlation terms in the IFT equation which are the only desired terms.

Fig. 4.2 shows the setup for a classical joint transform correlator. The input scene or the target image is loaded onto the upper part (or the lower part) of the SLM via the switching interface. The reference image (filter) which is already available in the digital system is loaded via the switching interface onto the lower (upper) part of the SLM. The light source LS provides the light and the light beam is collimated by lens L1. The light beam passing through the SLM is modulated by the joint images and passes through the second lens L2. This lens performs the Fourier transform of the joint image and the JPS of the resulting image is captured by the CCD1. The CCD1 transfers the image to the digital system where it is stored. The previous images are now replaced by this JPS onto the SLM. Similar operation takes place where the light source illuminates the SLM and the light beams are modulated by the new image. The light passes through the second lens L2 which now performs the inverse Fourier transform on the image and the power of the output is recorded by the CCD1 and again sent to the digital system for storage and further processing.

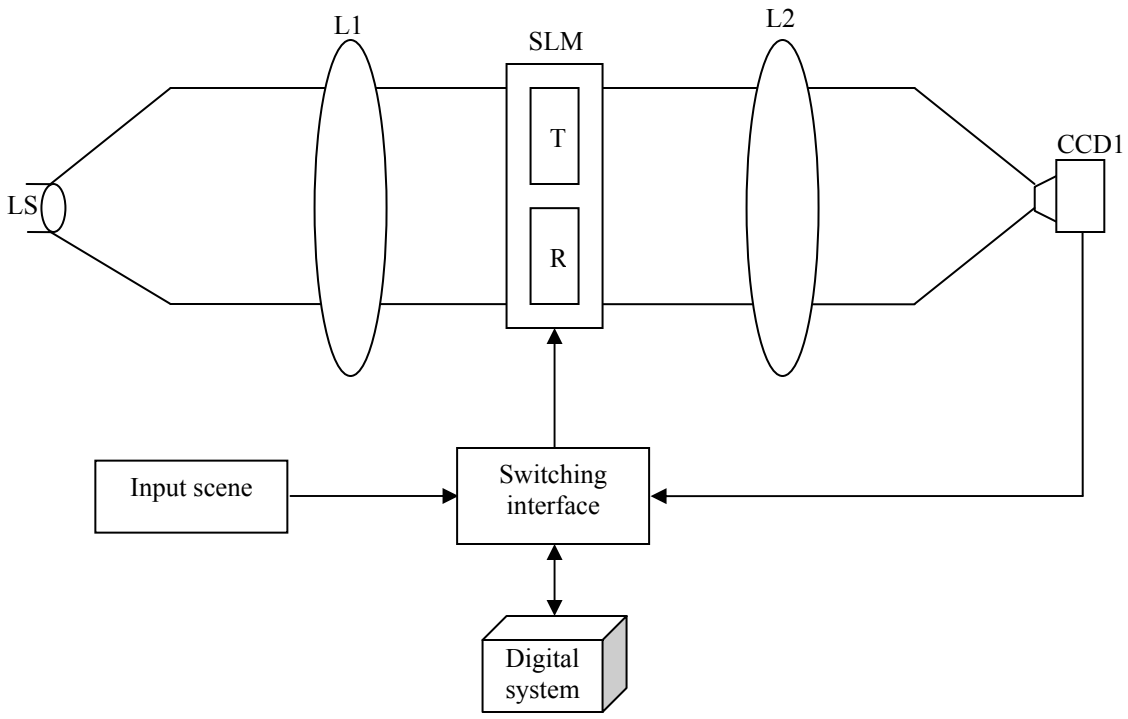


**Fig. 4.2 Classical JTC setup**

## 4.5. Fourier plane Image subtraction

It is observed that the first two terms in the JPS in equations (28) and (29) represented the autocorrelation terms. The cosine term in the JPS converts into two cross-correlation terms in the IFT equation which are the only desired terms. The additional autocorrelation terms are undesirable as they produce a very high zero order peak which overshadows the required cross-correlation peaks in presence of noise or distortion. Moreover, it becomes more dominant with the decreasing displacement between the two images. This can be improved by having a larger separation between the images but is not economical as it requires a larger size SLM. Also, a larger separation between images would mean sacrificing the image size leading to lower image resolution. This would create a constraint on the speed when it comes to correlating multiple images simultaneously. One effective technique for the elimination of the autocorrelation peaks is referred to as Fourier Image subtraction. It is especially useful when correlating more than two images simultaneously. For $N$ number of multiple targets equation (25) becomes,

$$f(x,y) = r(x, y + y_0) + \sum_{i=1}^{N} t_i(x, y - y_i) \qquad \text{.....(30)}$$

The Fourier transform of the above equation can be given by,

$$F(u,v) = |R(u,v)| \exp[j\phi_r(u,v) + jy_0 v] + \sum_{i=1}^{N} |T_i(u,v)| \exp[\phi_{ti}(u,v)] - jux_i - juy_i]$$

$$\text{.....(31)}$$

Then the JPS of the above equation is given by,

$$|F(u,v)|^2 = |R(u,v)|^2 + \sum_{i=1}^{N} |T_i(u,v)|^2$$

$$+ 2\sum_{i=1}^{N} |T_i(u,v)||R(u,v)| \cos[\phi_{ti}(u,v) - \phi_r(u,v) - ux_i - vy_i - 2vy_0]$$

$$k \neq i$$

$$+ 2\sum_{i=1}^{N}\sum_{k=1}^{N} |T_i(u,v)||T_k(u,v)| \cos[\phi_{ti}(u,v) - \phi_{tk}(u,v) - ux_i + ux_k - vy_i + vy_k]$$

$$\text{.....(32)}$$

As seen in equation (32) the third term corresponds to the cross-correlation between the reference and the different targets and is the significant term. The first term is the autocorrelation of the reference and the target image while the second term corresponds to the cross-correlation between the different targets. As discussed in the previous section these terms are unnecessary and must be discarded. It can be seen from equation (32) that the subtraction of the intensity of the reference and the target images can easily eliminate both these terms. However, an additional step is required which involves the capturing of the power spectra of all the target images. This classical JTC with Fourier image subtraction is the technique used for the optical processing in this thesis.

## 4.6. Optoelectronic Implementation

The idea behind the algorithm proposed in this thesis is to exploit the directionality in the texture of the radar images. However, the hindrance in the implementation of this algorithm was that it was computationally extensive. The complexity of our algorithm lies in the computation of the filtering operation for the Gabor filter at different orientations. Every different orientation added an additional

filtering operation. The filtering operation adds to processing time of the radar images. The satellite scans the scene every 6 to10 minutes. Hence, the processing time should be such that the images acquired are processed by the time the new set of images are acquired and loaded in the system. Performing the filtering operation digitally consumed a lot of time. Hence, processing the images digitally wasn't a good idea, as it did not serve our purpose of faster processing.

As discussed in section 4.3.4, the 2-D Fourier transform can be computed by optical correlation. This is done by using optical correlators as explained in sections 4.4 and 4.5. The optical correlators use simple multiplication in the frequency domain to correlate two images. One of the interesting properties of the optical implementation is that the correlation between different filters and different images can be computed in one single step. This is a major advantage over the electronic processing which would perform the operations sequentially at the expense of processing time.

The optoelectronic system performs the most time consuming filtering operations of the QC algorithm optically while the rests of the thresholding processes are executed digitally. Finally, the combination of the optical and the electronic implementation explained below provides an optimal performance in terms of quality and processing time.

Following explains the Optoelectronic implementation used in the proposed algorithm.

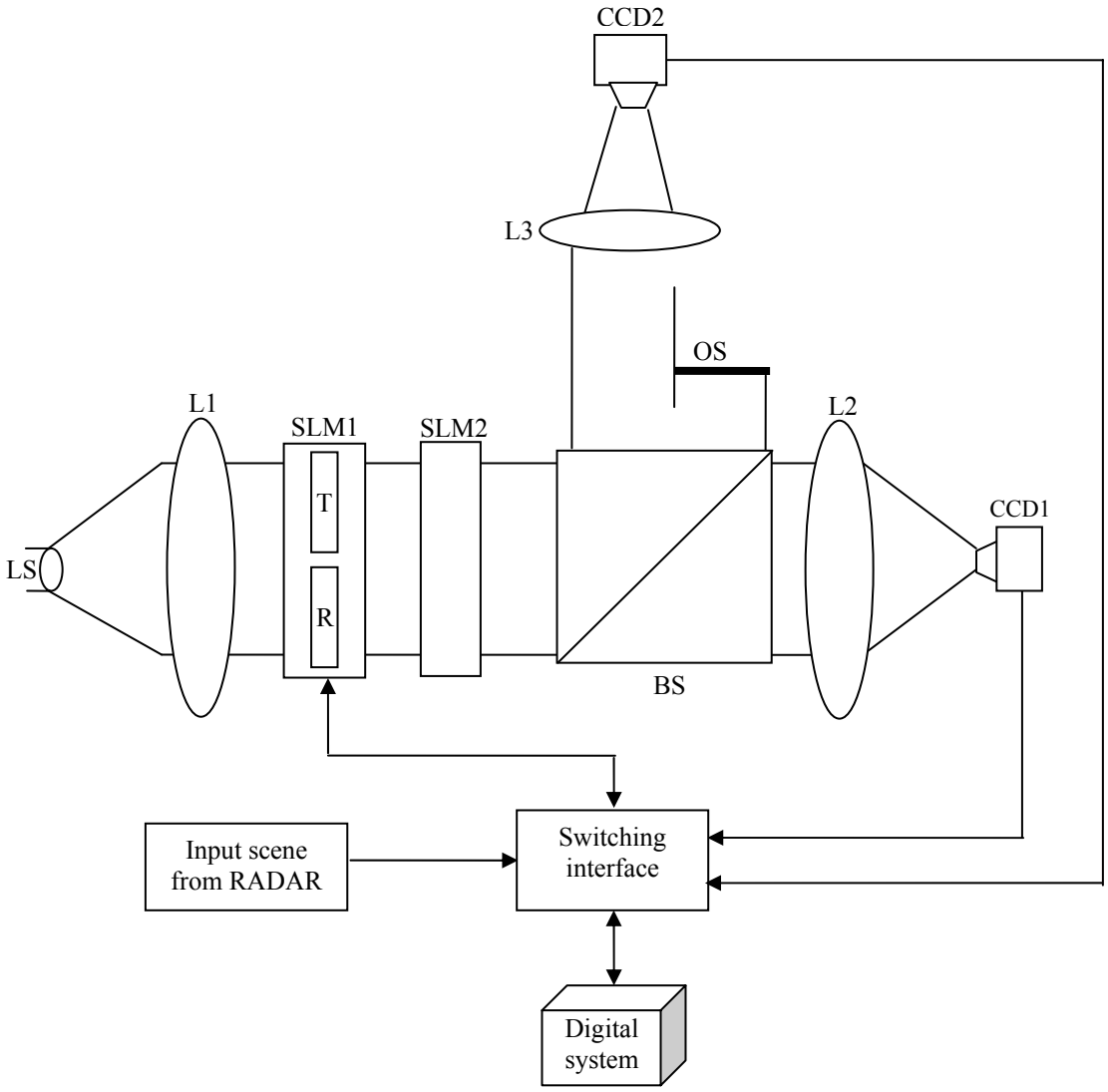


**Fig. 4.3 Optoelectronic set up**

The classical Joint Transform Correlator (JTC) with Fourier image subtraction shown in Fig.4.2 was chosen to perform the filtering operation. The complete optoelectronic implementation involved in this thesis is comprised of the steps discussed in section 3.1.4.2 and depicted in Fig.3.10 to Fig.3.12. The radar reflectivity images acquired from the radar at the two lower elevations are in polar coordinates. They are first converted to the Cartesian coordinates and then to a linear form in the digital system. This is done so that the conventional textural analysis can be performed in the image data. The addition of the images and computation of their power $q$ is done digitally. Also, the reference image which is the Gabor Filter with different orientations is computed

offline and stored in the digital system. Also, the intensities of the already available reference images required for the Fourier subtraction are also computed prior to initiation of the optical processing.

The functions of the different elements in the Optoelectronic set up depicted in Fig. 4.3 are given below.

*Light source (LS)*: Provides the coherent light needed for the optical system.

*Lens (L1):* It performs the function of collimating the light beams from the light source LS.

*Spatial Light Modulator (SLM1):* The target and the reference images are loaded onto this SLM.

*Spatial Light Modulator (SLM2):* This is an phase only SLM. It depicts two phases 0 and $\pi$, to denote positive and negative amplitudes respectively. It is necessary to represent the negative values which might be present in the result obtained after Fourier image subtraction. These negative values cannot be represented by SLM1 and hence the phase only SLM2 is required.

*Beam Splitter (BS):* The beam splitter splits the beam into two beams; the horizontal and the vertical beam. The horizontal beam is incident on lens L2 while the vertical beam encounters a optical stop and incidents beam on the Lens L3.

*Lens (L2 and L3):* These lenses perform the Fourier transform as well as the inverse Fourier transform of the modulated light beam incident on them.

*Optical Stop (OS):* The optical stop as the name suggests obstructs the lower part of the vertical light beam transmitting only the upper part. This upper part basically consists of the target image which is incident on the lens L3.

*Charged Couple Device (CCD1 and CCD2):* These capture the JPS of the Fourier transform performed by the leans L2 and L3.

*Switching Interface:* This is an interface between the optical system and the digital system. It aids the transfer of images from the digital system onto the SLM1 and from the CCD's to the digital system. Also, it transfers the images acquired from the radar to the digital system. In short it provides a connection between all these components.

*Digital system:* The digital system is responsible for the storage of images, the filters including the Gabor at different orientations and Gaussian. It also performs certain preprocessing on the image which is required to be done digitally and offline. Basically the addition, computation of the power of the images is all done digitally in the digital system.

The complete process involved in the opto electronic implementation of the proposed algorithm is explained in detail below.

*1.* The two radar images are preprocessed as explained above so that they are ready for further processing. This involves computing the power $q = 2$ of the two images and adding them up. This is done digitally and the resulting images are used for optical processing.

*2.* The addition of the images in analysis in scale 1 is performed digitally in the digital system. The result is stored in the digital system. The Gaussian filter is also precomputed and available in the digital system. The reference image (R) which is the precomputed Gaussian filter in the spatial domain and the target image (T) which is the added result of the radar images at the two elevations is uploaded onto the SLM via the switching interface. The target and reference images are placed next to each there with a certain separation. The light source LS emits the light necessary which is collimated by the lens L1. When the light travels through the SLM1 and phase only SLM2 it is modulated by the images and data encoded onto it. Here the phase only SLM2 acts as a simple clear transparency. The light beam splits into two beams by the beam splitter BS. The horizontal beam passes through the lens L2 which performs the Fourier transform of the joint image (target and reference image together). The power of this result also

referred as the JPS is captured by the CCD1 and sent to the digital system. At the same time the vertical beam encounters an optical stop OS. This optical stop obstructs the transmission of the reference image further and only the target image passes through the lens L3. The Fourier transform of the target image is generated by the lens and its JPS is recorded by the CCD2 and sent to the digital system and stored. The Fourier transform of the result and the intensities of the two images now available, the Fourier image subtraction is performed digitally. The result of the Fourier image subtraction is then loaded onto the SLM1 via the switching interface. The similar process again takes place where the light source LS illuminates the SLM1while passing through the collimating lens L1. The light passes through the SLM2 which is now a phase only SLM to represent negative values and is then incident on the lens L2. Lens L2 now performs the inverse Fourier transform of the image which is the desired correlated output. The CCD1 captures the power of this output. This output is then stored into the digital system

*3.* The outputs obtained at the end of part 1 and part 2 stored in the digital system are required further to compute the multifractals. Also, they need to be filtered by the Gabor filters at different orientations. This whole process of filtering the images by Gabor wavelets is done optically as is explained in this section. The Gabor filter with the optimal settings and different orientations is computed and stored in the digital system before hand. The Gabor filter with a particular orientation which is the reference image and both the target images i.e. outputs of part 1 and 2 and is loaded onto the SLM. The position of the target and the reference images loaded onto the SLM are seen in the Fig. 4.4. The reference though present exactly at the centre of the SLM is not visible due to its very small size.

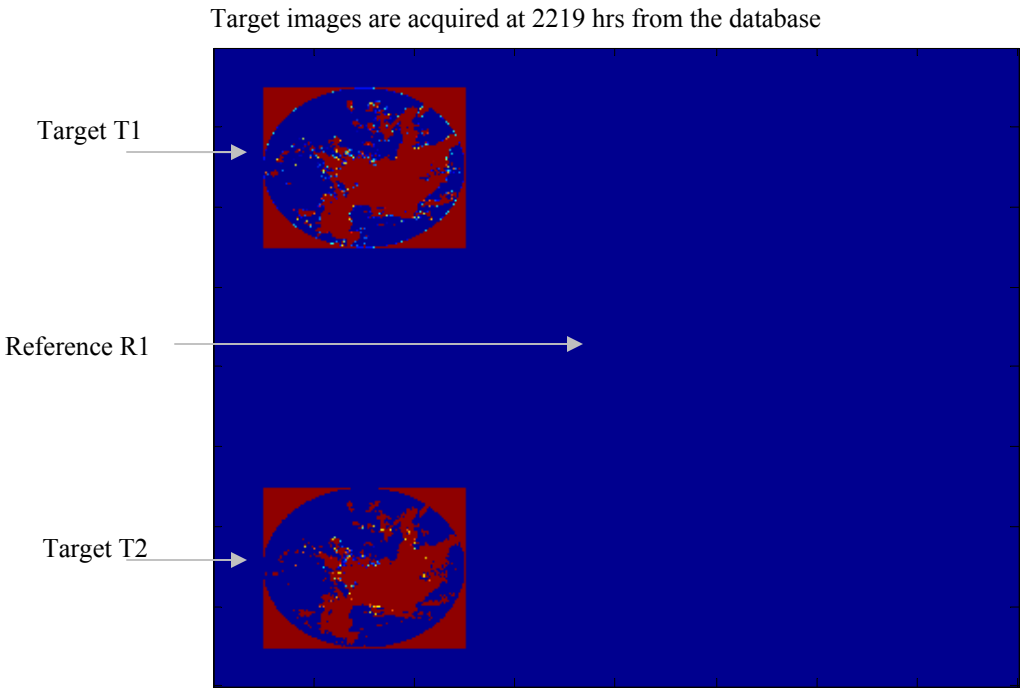


**Fig. 4.4 Images on the SLM**

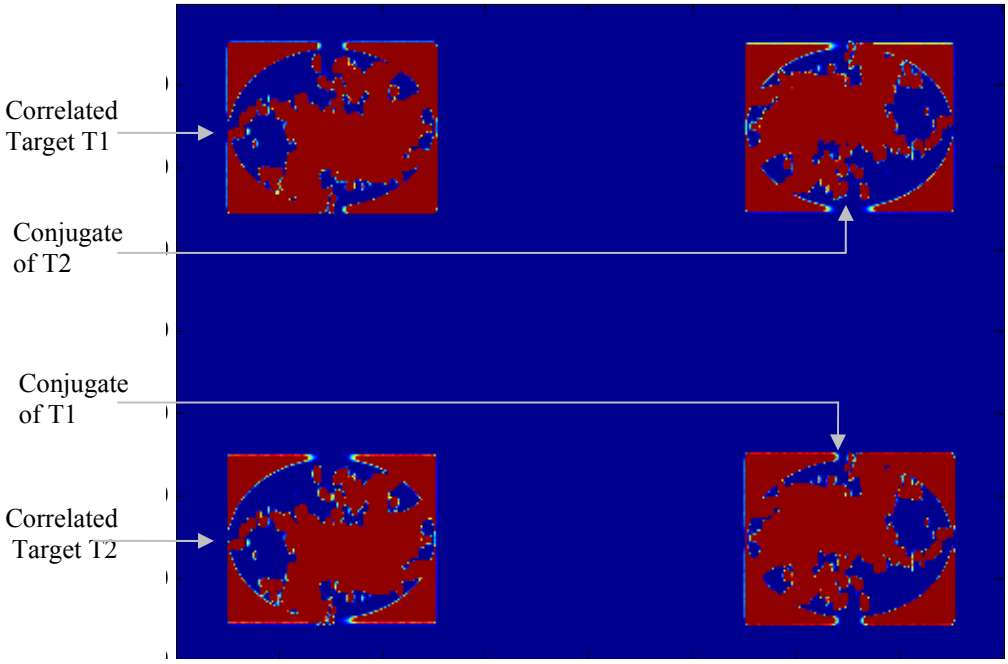


**Fig. 4.5 Correlation output of the images**

Fig.4.5 shows how the correlation outputs appear for the same target images. As can be seen the correlation output for both the targets are achieved in a single output. The other two images are the conjugates of the output and are not required and hence discarded.

As the Gabor filter is used to filter two different images as explained earlier, the final target image is a joint image containing both the processed radar reflectivity images. This facilitates similar operation on two different images to be done in a single step. The light source (LS) gives a coherent light beam which is collimated by the lens LI. The beam is modulated by the SLMI so that the joint image comprising of the target image and the reference image is encoded onto it. The beam splitter (BS) splits the beam into two. The lens L2 performs Fourier transform of the horizontal beam and its JPS is captured by the CCD1. This is then stored to the digital system via the switching interface. At the same time, the second vertical beam encounters an optical stop, which is moved in such a position so that it obstructs the lower part of the beam, which essentially contains the reference image. Thus, only the input scene i.e. the joint target image is transmitted onto lens L3 which performs the Fourier transform of the joint target image. This power spectrum is then recorded by CCD2 and sent to the digital system via the switching interface. The power spectrum of the reference image is precomputed and stored in the digital system. As the power spectrums of both the target image and the reference image are acquired, the Fourier image subtraction is done digitally. Further, this result replaces the previous image onto the SLM1 and the light beam from the light source LS is modulated. The lens L2 performs the inverse Fourier transform of this image incident on it which is essentially the filtered joint target image using the Gabor filter. The power spectrum of this result is then captured by CCD1 and sent to the digital system. For the new orientation of the Gabor filter the filter is just rotated by a $15^0$ step and the same process, as explained above is carried out for different filter orientations and all the results are stored in the digital system.

The other filtering operations involved are the filtering in the steps (1-3) explained in section 3.1.4.2. They are filtering operations used to filter the multifractals and the reflectivity images by simple average filters. The operations are carried exactly the same

way as explained above with the reference and the target images replaced by the desired ones. The results are stored in the digital system and used for further analysis.

This concludes the optical processing involved in the proposed algorithm. The subsequent operations involving the computation of the multifractals using the above optically obtained results, the maximum multifractal and thresholding are all done digitally which do not consume a lot of time.

The final result is an image comprising only the rain events or precipitation echoes present in the original radar image.

# CHAPTER 5

# 5. RESULTS

As discussed in section 3.1.4.6 several testing images were processed using the proposed QC algorithm and the different statistical measures extracted. For comparison, the statistical measures were also extracted for the GVS algorithm and the QC algorithms in [1]. All the results and the corresponding statistical measures are tabulated below.

Five images were used for training the algorithm. These were at times 01:09 hrs, 06:09 hrs, 10:09 hrs, 18:09 hrs and 23:09 hrs. Fifteen images were used for testing. These were at times 02:09 hrs, 04:09 hrs, 05:09 hrs, 07:09 hrs, 08:09 hrs, 11:09 hrs, 12:09 hrs, 14:09 hrs, 15:09 hrs, 16:09 hrs, 17:09 hrs, 20:09 hrs, 21:09 hrs, 22:09 hrs and 24:09 hrs. The training images were chosen from different times of the day so as to better train the algorithm. The idea here is to expose the algorithm to a data set that is an exhaustive representation on the entire data. Also the test images were chosen from different times of the day to evaluate the ability of the algorithm to work in varied conditions. Table 5.1 gives the statistical measures calculated for each of the test images using the proposed QC algorithm. All of these statistical measures are calculated for different dB ranges. Followed by this table are the corresponding plots shown in Fig.5.1 to 5.4 of each statistical measure for every test image. Table 5.2 is the average of these statistical measures in different ranges. The plots of these values follow the table given in Fig. 5.5 to 5.8

Table 5.3 gives the different statistical measures obtained for the GVS algorithm. The corresponding figures are shown in Fig. 5.9 to 5.12. The average computed for these statistical measures for different ranges is depicted in Table 5.4. and the relative plots are shown in Fig. 5.13 to 5.16

The statistical measures obtained for the QC algorithm in [1] are tabulated in Table5.5 and the corresponding plots are shown in Fig. 5.17 to 5.20. The average of these statistical measures is given in Table 5.6 and the plots shown in Fig. 5.21 to 5.24.

Finally, Table.5.7 shows the rain rates computed for results obtained by the three algorithms, accurate rain events and also the original reflectivity images. Fig.5.25 shows the corresponding rain rate plots assembled together.

**Table 5.1 Comparison results between accurate rain event and proposed algorithm results for each test image**

| *Test image 02:09 hrs* | | | | |
|---|---|---|---|---|
| ***Range (dB)*** | ***Error misses (%)*** | ***Error false Alarms (%)*** | ***Accuracy (%)*** | ***SNR (dB)*** |
| **0 – 10** | 0.000 | 3.712 | 96.288 | -Inf |
| **10-20** | 3.018 | 26.154 | 70.828 | 3.715 |
| **20-30** | 4.200 | 0.000 | 95.800 | 14.964 |
| **30-40** | 0.000 | 0.000 | 100.000 | Inf |
| **40-50** | 0.000 | 0.000 | 100.000 | Inf |
| *Test image 04:09 hrs* | | | | |
| **0 – 10** | 1.721 | 8.038 | 90.241 | -2.696 |
| **10-20** | 8.352 | 14.210 | 77.438 | 6.088 |
| **20-30** | 6.632 | 2.007 | 91.361 | 12.021 |
| **30-40** | 0.000 | 0.214 | 99.786 | 35.875 |
| **40-50** | 0.000 | 0.000 | 100.000 | Inf |
| *Test image 05:09 hrs* | | | | |
| **0 – 10** | 1.1889 | 12.6459 | 86.1652 | -4.2774 |
| **10-20** | 6.1732 | 21.3283 | 72.4985 | 4.7635 |
| **20-30** | 5.4511 | 6.203 | 88.3459 | 9.5724 |
| **30-40** | 0.2685 | 1.4765 | 98.255 | 20.0362 |
| **40-50** | 0 | 0 | 100 | Inf |
| *Test image 07:09 hrs* | | | | |
| **0 – 10** | 0.9223 | 24.4451 | 74.6326 | -4.8663 |
| **10-20** | 1.6872 | 29.1378 | 69.175 | 6.0521 |
| **20-30** | 1.0198 | 3.7296 | 95.2506 | 16.4652 |

| | | | | |
|---|---|---|---|---|
| **30-40** | 0.2398 | 1.3589 | 98.4013 | 22.6766 |
| **40-50** | 0 | 0.5236 | 99.4764 | 30.6474 |
| *Test image 08:09 hrs* | | | | |
| **0 – 10** | 0 | 24.0437 | 75.9563 | -Inf |
| **10-20** | 0.5381 | 45.5768 | 53.8851 | 4.9973 |
| **20-30** | 0.6402 | 1.9739 | 97.386 | 18.6926 |
| **30-40** | 0 | 0.7056 | 99.2944 | 21.0601 |
| **40-50** | 0 | 0.9756 | 99.0244 | 25.4961 |
| *Test image 11:09 hrs* | | | | |
| **0 – 10** | 1.2746 | 23.5942 | 75.1312 | -4.8314 |
| **10-20** | 2.0652 | 28.186 | 69.7489 | 6.4963 |
| **20-30** | 2.5774 | 1.9926 | 95.4299 | 17.303 |
| **30-40** | 0.3871 | 0.3226 | 99.2903 | 28.7298 |
| **40-50** | 0 | 0 | 100 | Inf |
| *Test image 12:09 hrs* | | | | |
| **0 – 10** | 5.393 | 12.1178 | 82.4892 | 0.671 |
| **10-20** | 0.0364 | 22.1966 | 77.767 | 6.0702 |
| **20-30** | 0.0454 | 6.7196 | 93.235 | 14.685 |
| **30-40** | 0.0867 | 1.2132 | 98.7002 | 21.6619 |
| **40-50** | 0 | 0 | 100 | Inf |
| *Test image 14:09 hrs* | | | | |
| **0 – 10** | 7.3265 | 26.4167 | 66.2568 | -2.0994 |
| **10-20** | 6.8554 | 21.1763 | 71.9683 | 6.8226 |
| **20-30** | 0.8689 | 3.1716 | 95.9595 | 17.2671 |
| **30-40** | 0 | 1.2715 | 98.7285 | 16.0867 |
| **40-50** | 0 | 1.1834 | 98.8166 | 22.1463 |
| *Test image 15:09 hrs* | | | | |
| **0 – 10** | 5.7533 | 30.3772 | 63.8695 | -2.6132 |
| **10-20** | 11.5634 | 17.3368 | 71.0999 | 7.3334 |
| **20-30** | 1.4552 | 1.8088 | 96.736 | 18.1283 |

| | | | | |
|---|---|---|---|---|
| **30-40** | 0.2711 | 0.723 | 99.0059 | 16.3798 |
| **40-50** | 0 | 0 | 100 | Inf |
| *Test image 16:09 hrs* | | | | |
| **0 – 10** | 10.2133 | 21.0538 | 68.7329 | 0.3308 |
| **10-20** | 8.9859 | 13.6647 | 77.3494 | 8.2386 |
| **20-30** | 1.171 | 1.3889 | 97.4401 | 18.6488 |
| **30-40** | 0 | 0.3047 | 99.6953 | 29.9134 |
| **40-50** | 0 | 0.495 | 99.5049 | 18.7082 |
| *Test image 17:09 hrs* | | | | |
| **0 – 10** | 2.549 | 33.0619 | 64.3891 | -6.4894 |
| **10-20** | 5.083 | 34.6374 | 60.2795 | 5.067 |
| **20-30** | 1.4868 | 3.2896 | 95.2236 | 16.1758 |
| **30-40** | 0.0555 | 1.2215 | 98.7229 | 15.8076 |
| **40-50** | 0 | 1.6393 | 98.3607 | 21.2187 |
| *Test image 20:09 hrs* | | | | |
| **0 – 10** | 12.8495 | 9.4799 | 77.6707 | 2.191 |
| **10-20** | 10.2005 | 7.8092 | 81.9903 | 8.7746 |
| **20-30** | 1.5622 | 2.7079 | 95.7299 | 15.9046 |
| **30-40** | 0 | 3.1731 | 96.8269 | 12.5667 |
| **40-50** | 0 | 7.3333 | 92.6667 | 9.4951 |
| *Test image 21:09 hrs* | | | | |
| **0 – 10** | 6.6745 | 11.239 | 82.0865 | 0.1533 |
| **10-20** | 16.022 | 10.138 | 73.84 | 7.3481 |
| **20-30** | 1.805 | 2.9037 | 95.2913 | 15.5961 |
| **30-40** | 0 | 2.4201 | 97.5799 | 15.6968 |
| **40-50** | 0 | 2.7211 | 97.2789 | 23.2162 |
| *Test image 22:09 hrs* | | | | |
| **0 – 10** | 7.9055 | 16.4339 | 75.6606 | 0.1459 |
| **10-20** | 11.7273 | 10.595 | 77.6776 | 8.5448 |
| **20-30** | 1.8394 | 3.2062 | 94.9544 | 12.9456 |

| | | | | |
|---|---|---|---|---|
| **30-40** | 0 | 2.9 | 97.1 | 19.6301 |
| **40-50** | 0 | 1.5504 | 98.4496 | 22.8224 |
| *Test image 24:09 hrs* | | | | |
| **0 – 10** | 3.9285 | 15.6624 | 80.409 | 0.028 |
| **10-20** | 0.0401 | 19.0656 | 80.8943 | 8.0067 |
| **20-30** | 0 | 2.0922 | 97.9078 | 22.3113 |
| **30-40** | 0 | 0.4108 | 99.5892 | 28.901 |
| **40-50** | 0 | 0 | 100 | Inf |

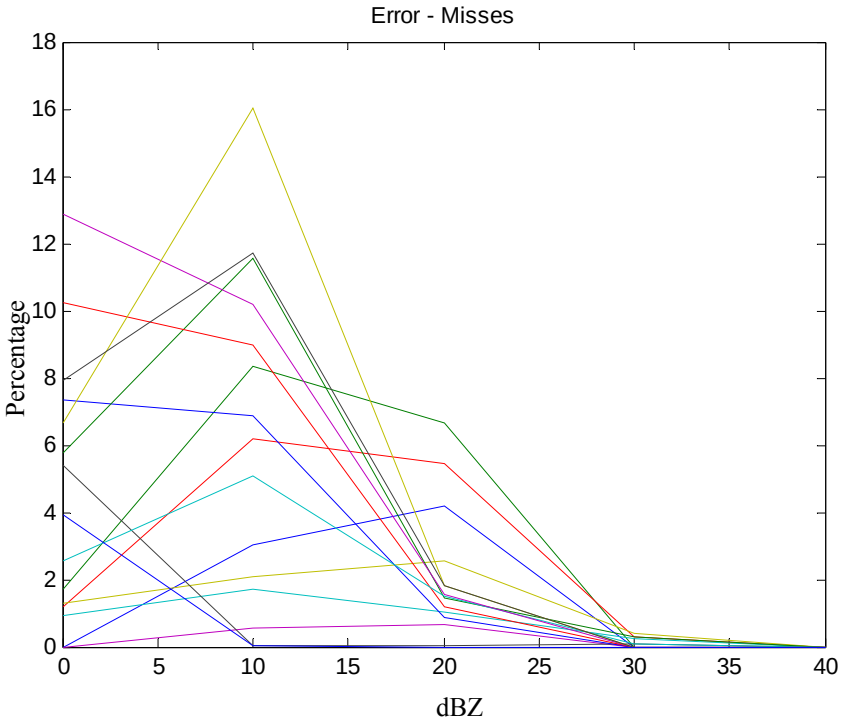


**Fig. 5.1 Proposed algorithm results - Percentage of misses**

Fig. 5.1 displays the compilation of plots of the percentages, for different image cases, when a pixel was actually a precipitation pixel according to the accurate rain event information and was mislabeled as a non-precipitation pixel. Every plot represents the percentage of misses for a test image at different reflectivity ranges. These plots show that though the algorithm has a high miss error rate for the low-intensity pixels, it works

much better for the high-intensity pixels. The proposed algorithm does not miss as much of the high intensity pixels. This is a comforting fact as the high intensity pixels are characteristics of precipitation.

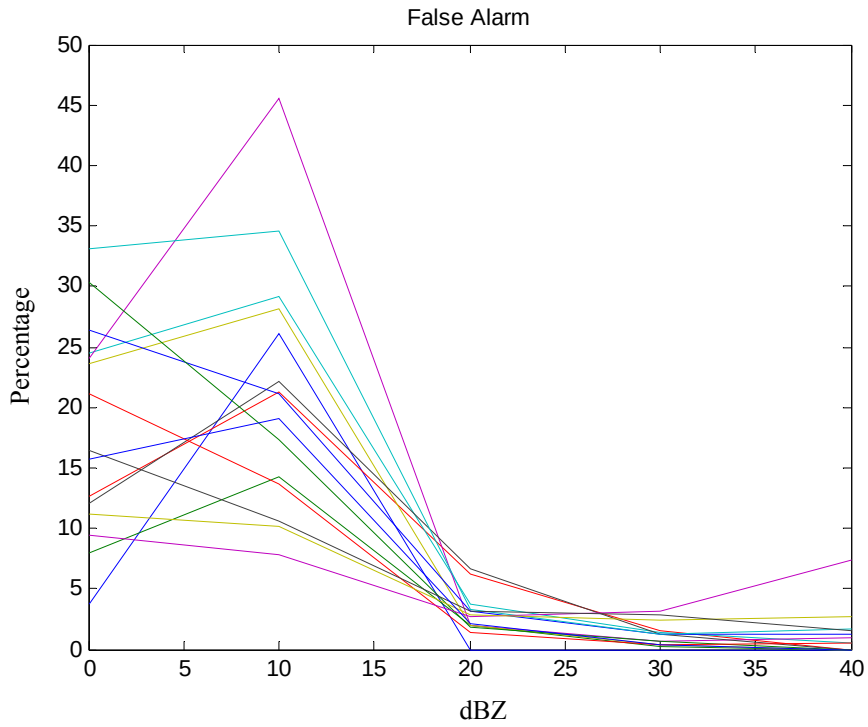


**Fig. 5.2 Proposed algorithm results - Percentage of false alarms**

Fig. 5.2 displays the plots of the percentages, for different image cases, when a pixel was actually a non-precipitation pixel according to accurate rain events and was mislabeled as a precipitation pixel. It shows every plot corresponding to every test image. These plots also show that though the algorithm has a high false alarm error rate for the low-intensity pixels, it works a lot better for the high-intensity pixels. This shows that the proposed algorithm does not misidentify a non-precipitation pixel as precipitation for the high intensity pixels, which are characteristics of precipitation.

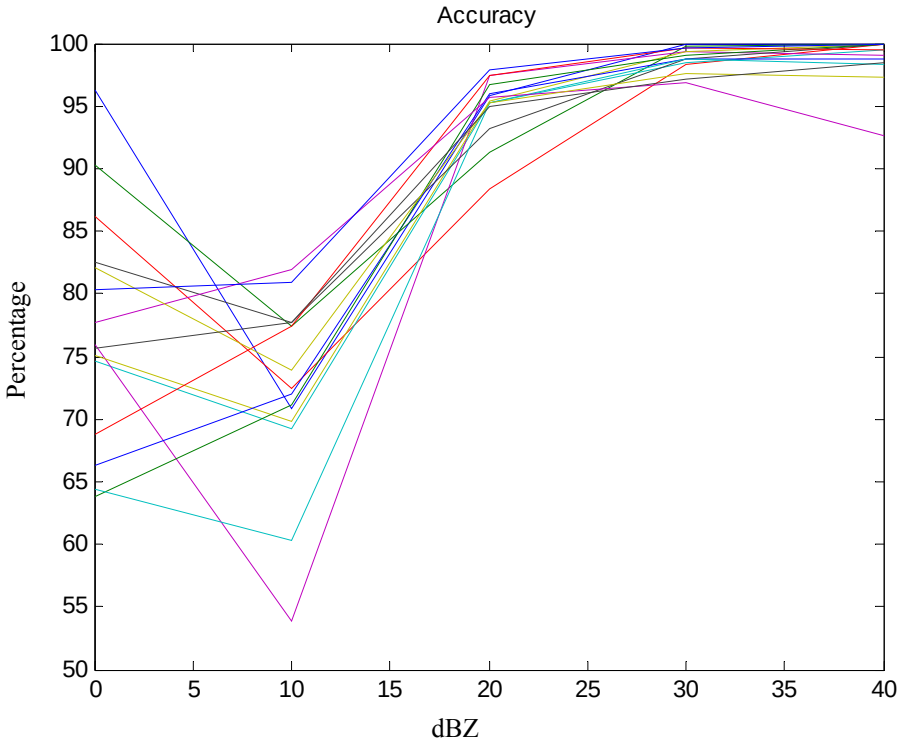


**Fig. 5.3 Proposed algorithm results – Accuracy**

Fig. 5.3 displays the plots of the percentages, for different image cases, when a pixel was actually a precipitation pixel according to the accurate rain event and was correctly labeled as a precipitation pixel, or when a pixel was actually a non-precipitation pixel according to the accurate rain event and was labeled appropriately as a non-precipitation pixel. These plots also show that though the proposed algorithm has a low accuracy for the low-intensity pixels, it works desirably for the high-intensity pixels that are characteristics of precipitation.

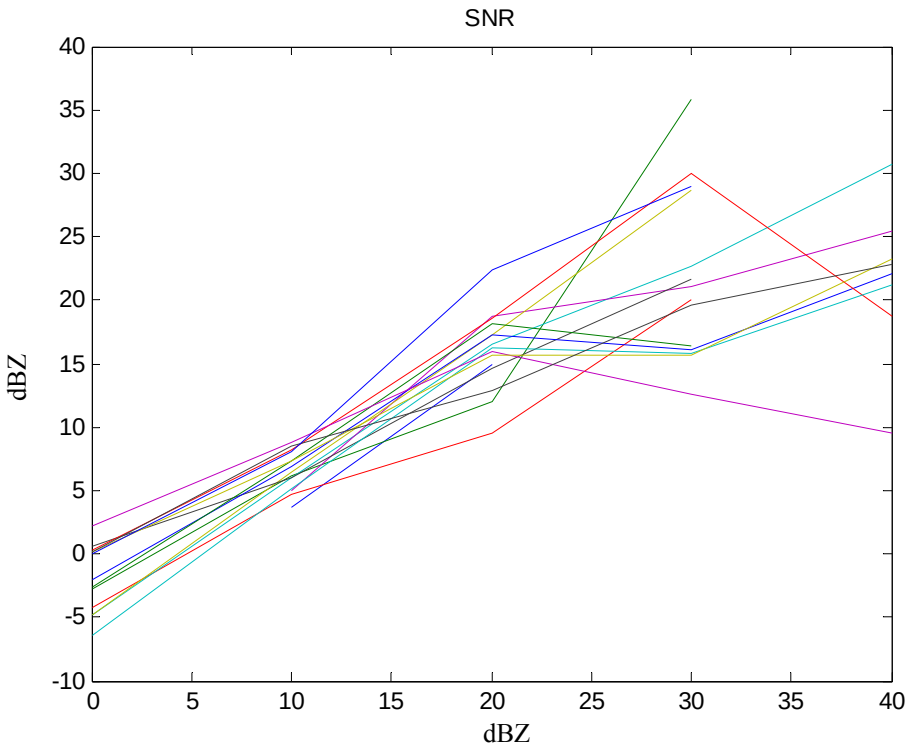


**Fig. 5.4 Proposed algorithm results – SNR**

Fig. 5.4 displays the plots of the signal to noise ratios (SNR), for different image cases. Here the precipitation in the accurate rain event image is considered as the signal and the difference in the final result image and the ground truth is considered as the noise. These plots also show that though the proposed algorithm has a low accuracy for the low-intensity pixels, it works better for the high-intensity pixels that are characteristics of precipitation. The abrupt changes seen in some of these plots indicate an SNR value of either -∞ (for low intensities) or +∞ (for high intensities).

**Table 5.2 Comparison results between accurate rain event and proposed algorithm results for testing set (average of 15 test image)**

| Testing Set | | | | |
|---|---|---|---|---|
| Range (dB) | Error misses (%) | Error false Alarms (%) | Accuracy (%) | SNR (dB) |
| **0 – 10** | 4.513 | 18.155 | 77.332 | -Inf |
| **10-20** | 6.157 | 21.414 | 72.429 | 6.555 |
| **20-30** | 2.050 | 2.880 | 95.070 | 16.045 |
| **30-40** | 0.087 | 1.181 | 98.732 | Inf |
| **40-50** | 0 | 1.095 | 98.905 | Inf |

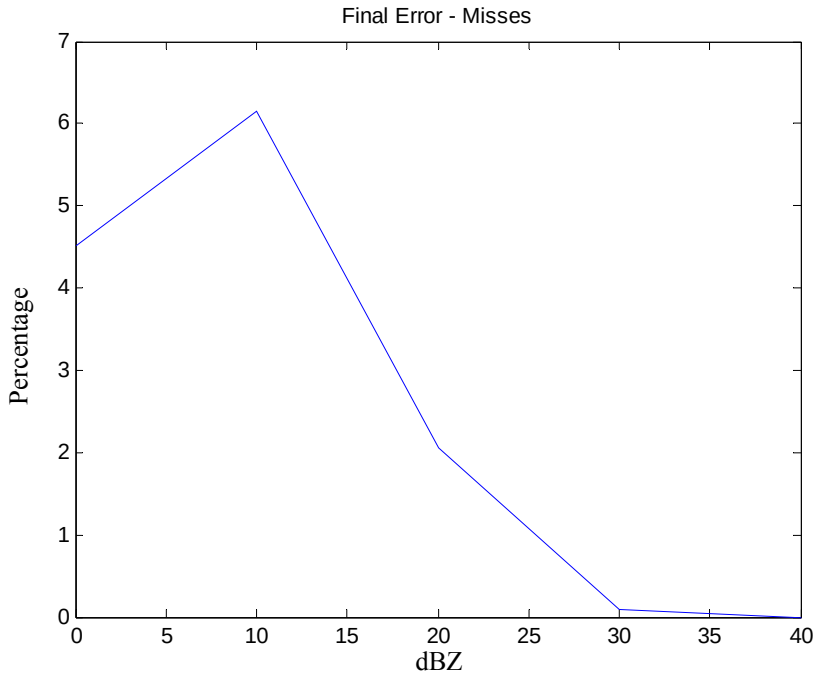


**Fig. 5.5 Proposed algorithm results - Percentage of misses (Average of 15 images)**

Fig. 5.5 shows the plot for the average miss error for all the fifteen test images. This clearly shows a general trend of improvement of the working of the algorithm with increasing pixel intensity.

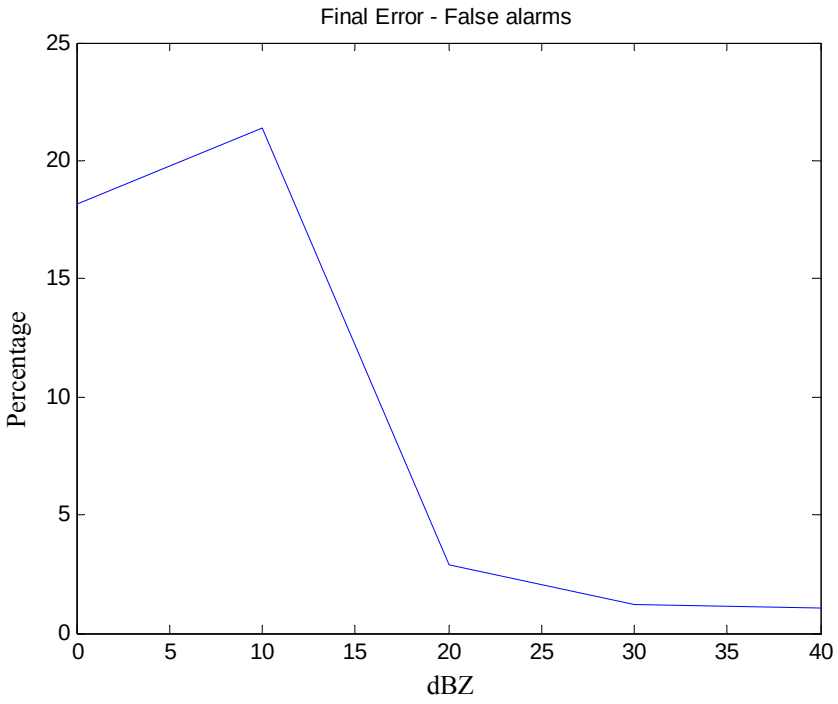


**Fig. 5.6 Proposed algorithm results - Percentage of False Alarms (Average of 15 images)**

Fig. 5.6 shows the plot for the average false alarm error for all the fifteen test images. Again this figure shows the improvement of the working of the algorithm with increasing pixel intensity in general.

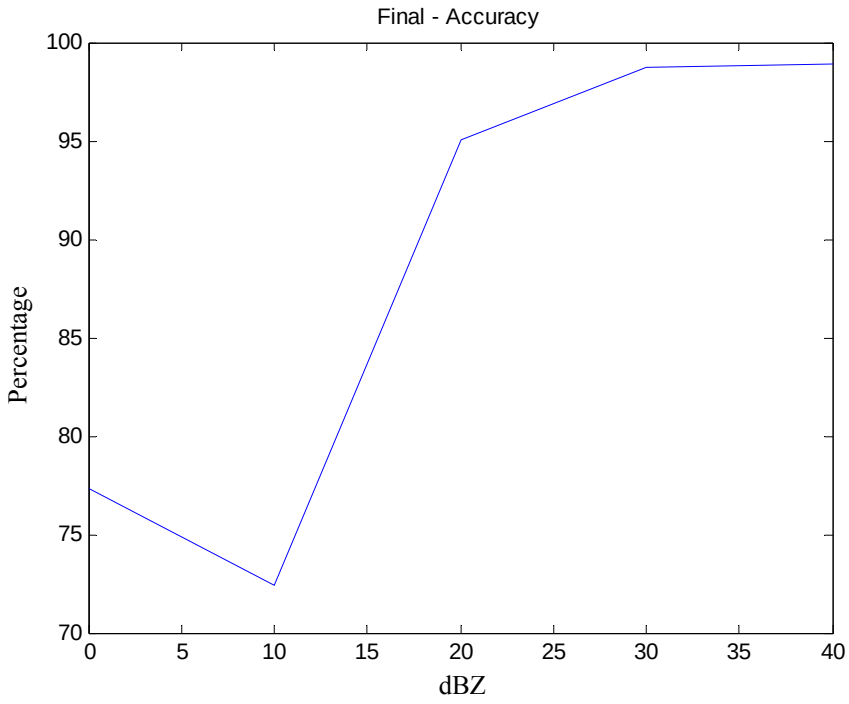


**Fig. 5.7 Proposed algorithm results - Accuracy (Average of 15 images)**

Fig. 5.7 shows the plot for the average accuracy for all the fifteen test images. This figure indicates the high performance of the proposed algorithm for high intensity pixels.

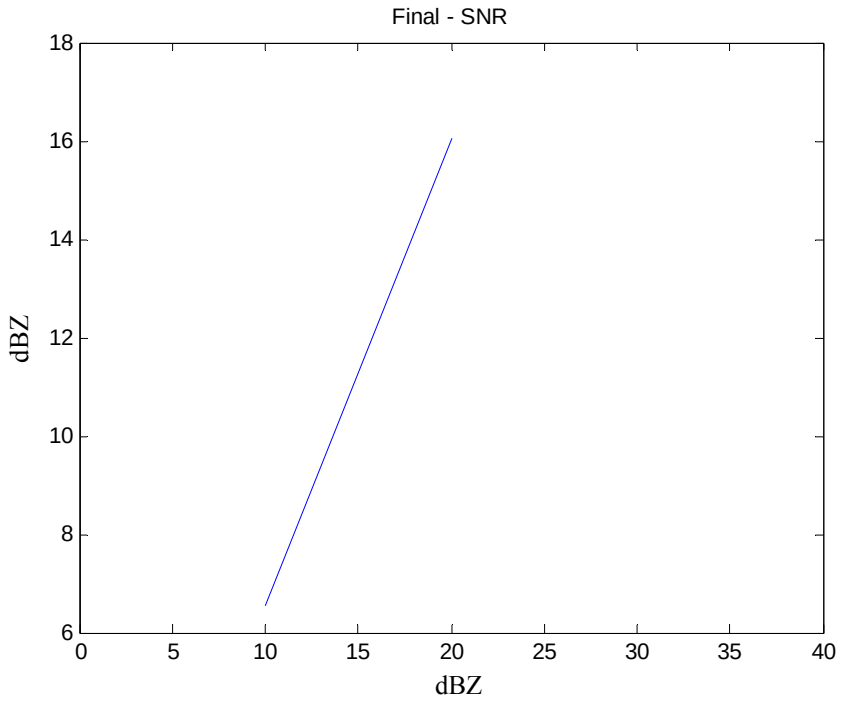


**Fig. 5.8 Proposed algorithm results – SNR (Average of 15 images)**

Fig. 5.8 shows the plot for the average SNR for all the fifteen test images. This figure also confirms that the for high intensity pixels, the proposed algorithm works so well that the SNR actually reaches $+\infty$.

**Table 5.3 Comparison results between accurate rain event and GVS results for each test image**

| Test image 02:09 hrs | | | | |
|---|---|---|---|---|
| Range (dB) | Error misses (%) | Error false Alarms (%) | Accuracy (%) | SNR (dB) |
| **0 – 10** | 0 | 73.4061 | 73.4061 | -Inf |
| **10-20** | 1.7466 | 33.2962 | 41.0256 | 2.2635 |
| **20-30** | 1.7982 | 13.5864 | 60.04 | 22.3033 |
| **30-40** | 0 | 9.4241 | 75.1309 | 416.8279 |
| **40-50** | 0 | 7.3684 | 97.8947 | 427.9789 |
| Test image 04:09 hrs | | | | |

| | | | | |
|---|---|---|---|---|
| **0 – 10** | 0.3493 | 60.0452 | 63.0865 | -2.3845 |
| **10-20** | 0.7318 | 19.4832 | 47.2445 | 6.5284 |
| **20-30** | 0 | 8.5119 | 64.3891 | 16.4734 |
| **30-40** | 0 | 3.6145 | 79.8623 | 30.0946 |
| **40-50** | 0 | 4.386 | 98.2456 | 427.4191 |
| Test image 05:09 hrs | | | | |
| **0 – 10** | 0.1511 | 47.6291 | 50.5057 | -4.6721 |
| **10-20** | 0.1841 | 16.7392 | 41.4463 | 5.4021 |
| **20-30** | 0 | 5.5164 | 57.1596 | 10.4122 |
| **30-40** | 0 | 2.0833 | 76.4583 | 19.7267 |
| **40-50** | 0 | 0 | 96.2791 | 22.4922 |
| Test image 07 09 hrs | | | | |
| **0 – 10** | 0.2129 | 32.7221 | 35.7848 | -4.3997 |
| **10-20** | 0.3611 | 11.8508 | 37.5613 | 5.0453 |
| **20-30** | 0 | 3.8982 | 67.0497 | 15.949 |
| **30-40** | 0 | 1.8031 | 85.1595 | 21.2024 |
| **40-50** | 0 | 4.712 | 99.4764 | 30.0082 |
| Test image 08:09 hrs | | | | |
| **0 – 10** | 0 | 36.1432 | 36.1432 | -Inf |
| **10-20** | 0.4479 | 17.3399 | 28.4857 | 3.2929 |
| **20-30** | 0.3808 | 6.437 | 65.5666 | 16.7306 |
| **30-40** | 0 | 2.0385 | 87.7123 | 19.4385 |
| **40-50** | 0 | 5.7971 | 98.0676 | 25.4961 |
| Test image 11:09 hrs | | | | |
| **0 – 10** | 0.3081 | 31.4768 | 34.6022 | -4.9542 |
| **10-20** | 0.6741 | 11.3771 | 40.412 | 5.3058 |
| **20-30** | 0.2244 | 0.7855 | 71.9141 | 17.2399 |
| **30-40** | 0 | 0.7403 | 95.3115 | 30.8786 |
| **40-50** | 0 | 0 | 100 | Inf |
| Test image 12:09 hrs | | | | |

| | | | | |
|---|---|---|---|---|
| **0 – 10** | 2.7502 | 38.2259 | 45.8959 | 0.6035 |
| **10-20** | 1.0498 | 8.4628 | 40.1424 | 3.6375 |
| **20-30** | 0.2114 | 0.8455 | 71.0763 | 13.709 |
| **30-40** | 0.2358 | 0 | 89.3868 | 20.22 |
| **40-50** | 0 | 0 | 98.3051 | Inf |
| Test image 14:09 hrs | | | | |
| **0 – 10** | 2.2231 | 21.8028 | 26.2587 | -1.4782 |
| **10-20** | 2.2513 | 8.3686 | 43.7376 | 7.8972 |
| **20-30** | 0.5665 | 1.5378 | 77.9396 | 19.8157 |
| **30-40** | 0 | 0.6881 | 89.6789 | 19.4671 |
| **40-50** | 0 | 0 | 97.6608 | 22.1463 |
| Test image 15:09 hrs | | | | |
| **0 – 10** | 0.8658 | 15.6737 | 19.7909 | -2.3128 |
| **10-20** | 1.7979 | 4.6809 | 43.2454 | 8.6415 |
| **20-30** | 0.8445 | 0.999 | 73.4706 | 17.6642 |
| **30-40** | 0 | 0.4243 | 93.1269 | 19.2908 |
| **40-50** | 0 | 1.3889 | 98.6111 | 436.5306 |
| Test image 16:09 hrs | | | | |
| **0 – 10** | 3.3092 | 16.7611 | 24.2579 | 0.0986 |
| **10-20** | 2.6626 | 6.5246 | 50.305 | 9.2079 |
| **20-30** | 0.7396 | 1.5336 | 78.1162 | 17.8832 |
| **30-40** | 0.1622 | 0.8108 | 88.3243 | 27.0829 |
| **40-50** | 0 | 0.9569 | 96.6507 | 442.3445 |
| Test image 17:09 hrs | | | | |
| **0 – 10** | 0.501 | 21.3225 | 23.4698 | -6.5516 |
| **10-20** | 1.4555 | 7.2886 | 37.1014 | 4.6177 |
| **20-30** | 0.3396 | 1.3582 | 77.7872 | 17.3926 |
| **30-40** | 0 | 0.8738 | 86.6019 | 20.2624 |
| **40-50** | 0 | 0.3861 | 92.6641 | 20.8017 |
| Test image 20:09 hrs | | | | |

| | | | | |
|---|---|---|---|---|
| **0 – 10** | 7.8893 | 26.9427 | 34.7449 | 0.7752 |
| **10-20** | 8.0262 | 6.3228 | 53.1418 | 7.4305 |
| **20-30** | 3.5088 | 1.136 | 76.9341 | 13.5363 |
| **30-40** | 0.1676 | 0.6706 | 83.8223 | 12.7171 |
| **40-50** | 0 | 2.6144 | 90.8497 | 9.4951 |
| Test image 21:09 hrs | | | | |
| **0 – 10** | 3.7473 | 36.3439 | 40.5402 | -1.1787 |
| **10-20** | 13.0909 | 7.7815 | 45.9785 | 6.143 |
| **20-30** | 3.0737 | 1.1308 | 76.6046 | 14.0852 |
| **30-40** | 0.5922 | 1.4382 | 85.8714 | 19.5676 |
| **40-50** | 0 | 2.0134 | 97.9866 | 28.1047 |
| Test image 22:09 hrs | | | | |
| **0 – 10** | 3.0313 | 27.0327 | 33.2116 | 0.1331 |
| **10-20** | 9.6573 | 6.7187 | 53.6138 | 7.7175 |
| **20-30** | 3.0617 | 1.9702 | 79.8724 | 14.5515 |
| **30-40** | 0 | 2.3915 | 88.2197 | 32.4509 |
| **40-50** | 0 | 0.7752 | 99.2248 | 26.3615 |
| Test image 24:09 hrs | | | | |
| **0 – 10** | 3.2952 | 26.9096 | 31.8651 | -1.6038 |
| **10-20** | 3.778 | 9.9272 | 38.2182 | 4.4094 |
| **20-30** | 2.2106 | 0.1906 | 79.1005 | 16.6333 |
| **30-40** | 0 | 0.0784 | 95.1373 | 29.0094 |
| **40-50** | 0 | 0 | 100 | Inf |

In table 5.3, the results for the miss errors, the false alarm errors, the accuracies and the SNRs for all the fifteen test images are reported for the GVS results. All these results are also plotted in Figs. 5.9 to 5.12. Here it can be observed that the overall accuracy is lower that that of the results of the proposed algorithm for any pixel intensity range. The overall errors are also higher than the corresponding errors in the results of the proposed algorithm. Similar relationship between the performances can be observed between the two results while comparing the SNR results.

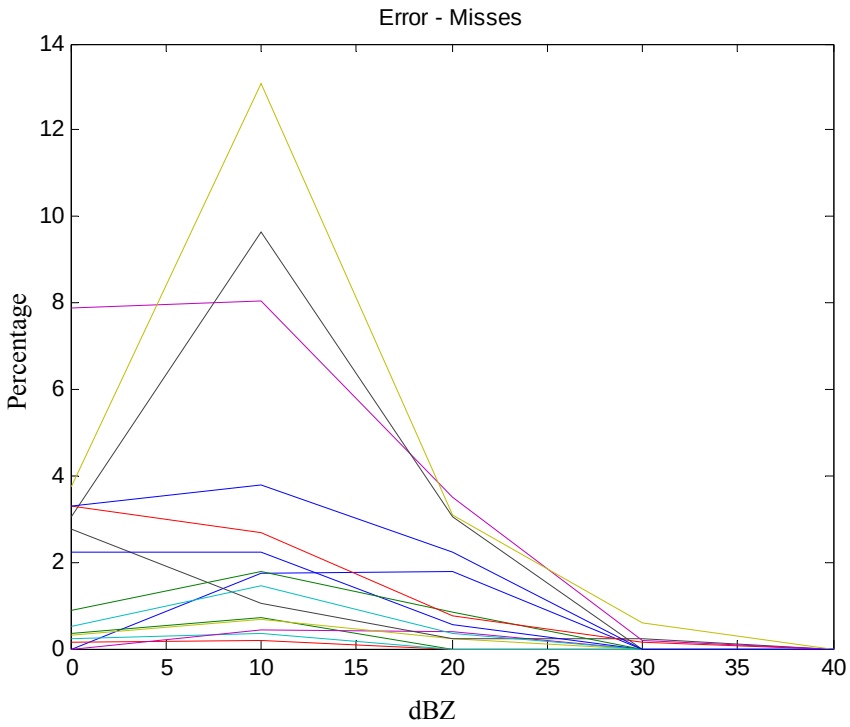


**Fig. 5.9 GVS results - Percentage of misses**

Fig. 5.9 displays the compilation of plots of the percentages, for different image cases, when a pixel was actually a precipitation pixel according to the accurate rain event information and was mislabeled as a non-precipitation pixel, for the GVS results.

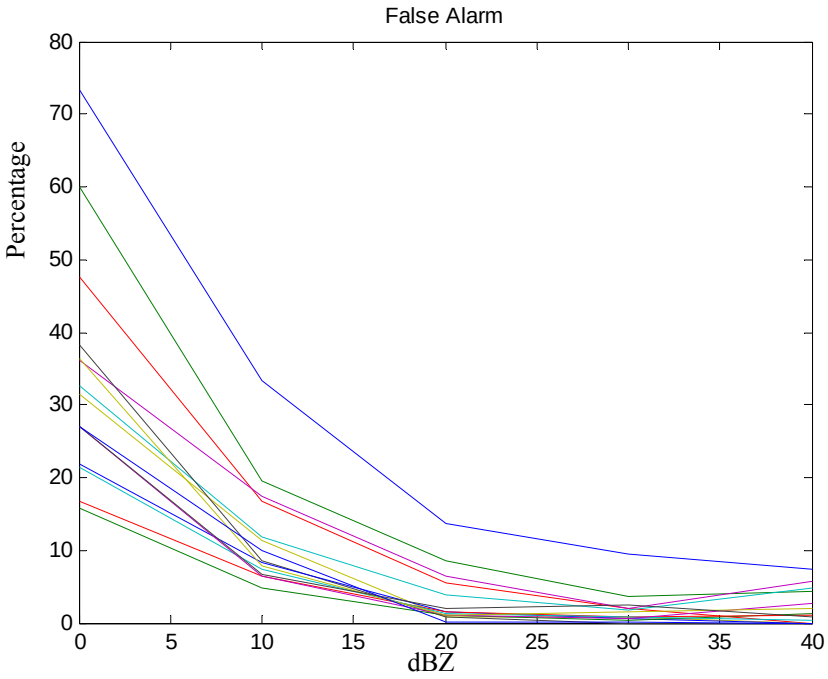


**Fig. 5.10 GVS results - Percentage of False Alarms**

Fig. 5.10 displays the plots of the percentages, for different image cases, when a pixel was actually a non-precipitation pixel according to accurate rain events and was mislabeled as a precipitation pixel, for the GVS result. This plot shows that the false alarms are about 10 % for pixels with intensity of 20 dBZ. This is inferior as compared to the results of the proposed QC algorithm where, as seen in Fig. 5.2, the false alarms are under 5 % for pixels with intensity of 20 dBZ.

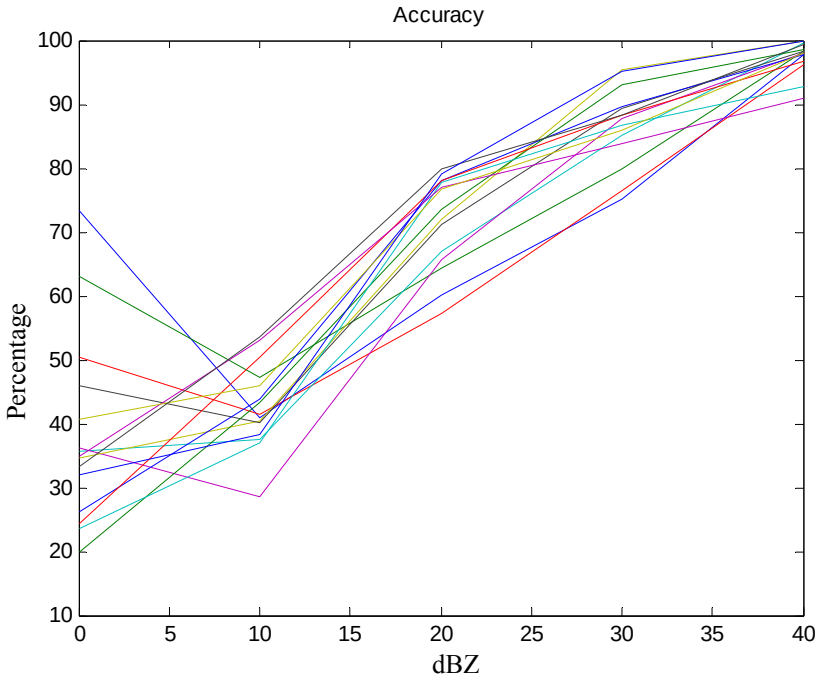


**Fig. 5.11 GVS results – Accuracy**

Fig. 5.11 displays the plots of the percentages, for different image cases, when a pixel was actually a precipitation pixel according to the accurate rain event and was correctly labeled as a precipitation pixel, or when a pixel was actually a non-precipitation pixel according to the accurate rain event and was labeled appropriately as a non-precipitation pixel, for the GVS results. Here it can be observed that the overall accuracies don't rise beyond 80% where as from Fig. 5.3 it can be seen that the accuracies rise past 90 % for the results of the proposed algorithm.

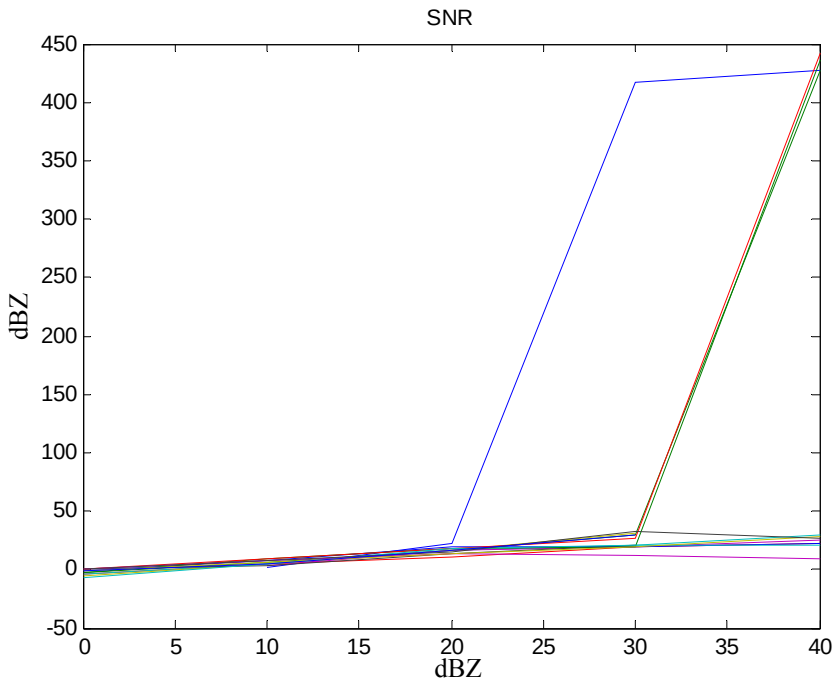


**Fig. 5.12 GVS results – SNR**

Fig. 5.12 displays the plots of the signal to noise ratios (SNR), for different image cases, for the GVS results. Here the precipitation in the accurate rain event image is considered as the signal and the difference in the final result image and the ground truth is considered as the noise. All the images exhibit finite SNR as seen in the plot above, which indicates some residual error. However, in the proposed QC algorithm, most of the cases do not have any errors, which are demonstrated by an infinite SNR as seen ion Fig. 5.4.

**Table 5.4 Comparison results between accurate rain event and GVS results for testing set (average of 15 test image)**

| Testing Set | | | | |
|---|---|---|---|---|
| Range (dB) | Error misses (%) | Error false Alarms (%) | Accuracy (%) | SNR (dB) |
| **0 – 10** | 1.909 | 34.162 | 38.238 | -Inf |
| **10-20** | 3.194 | 11.744 | 42.777 | 5.836 |
| **20-30** | 1.131 | 3.296 | 71.801 | 16.292 |

| | | | | |
|---|---|---|---|---|
| **30-40** | 0.077 | 1.805 | 86.654 | 49.216 |
| **40-50** | 0.000 | 2.027 | 97.461 | Inf |

In table 5.4, the averages for the miss errors, false alarm errors, accuracies and SNRs for the fifteen test images are presented. These results, also plotted in Figs. 5.13 to 5.16, also support the above discussion.

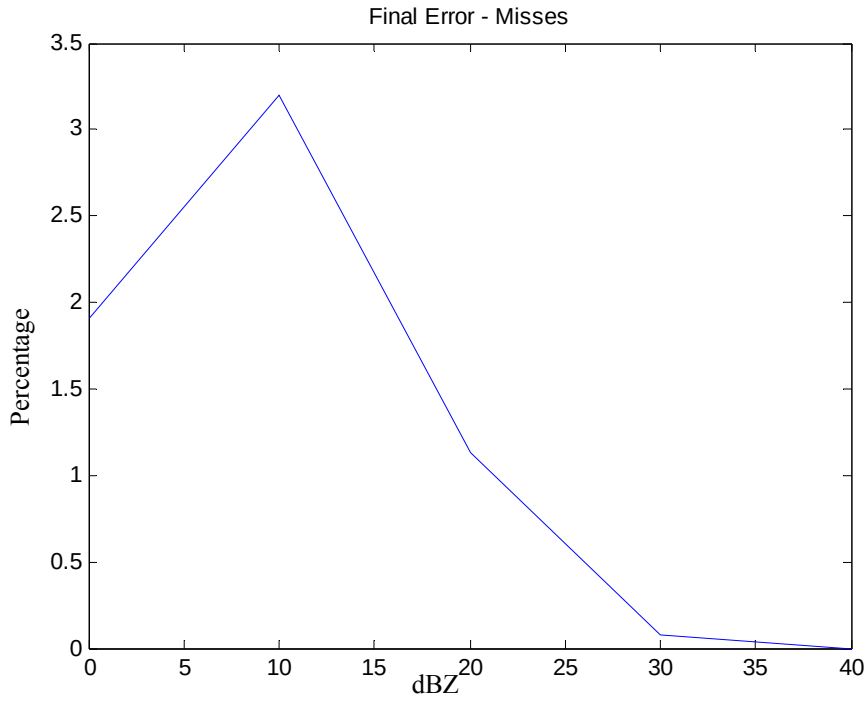


**Fig. 5.13 GVS results - Percentage of misses (Average of 15 images)**

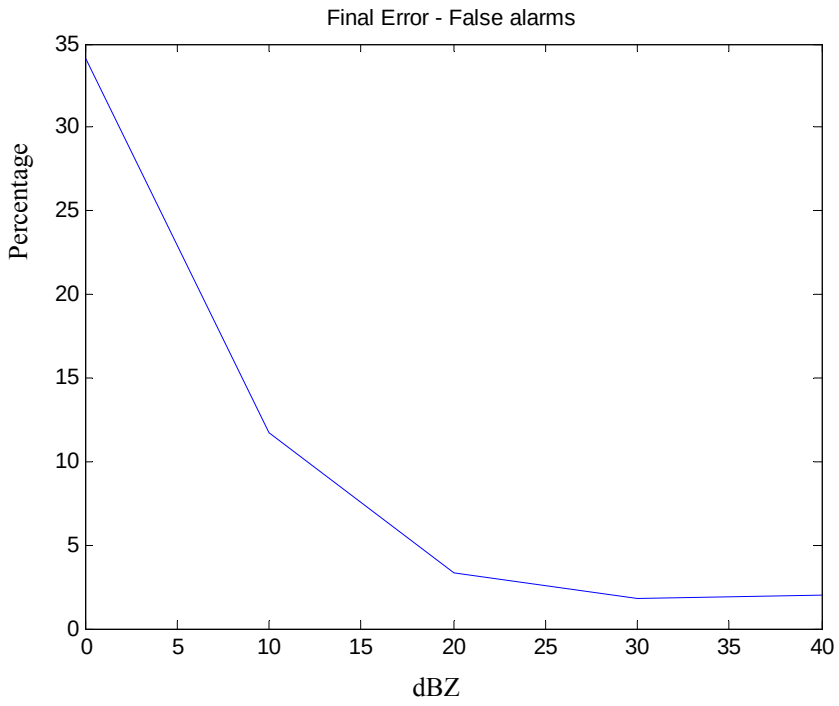


**Fig. 5.14 GVS results - Percentage of False Alarms (Average of 15 images)**

Fig. 5.14 shows the plot for the average false alarm error for all the fifteen test images, for the GVS results. Again this figure shows that the GVS results are inferior as compared to those of the proposed QC algorithm as seen in Fig. 5.6.

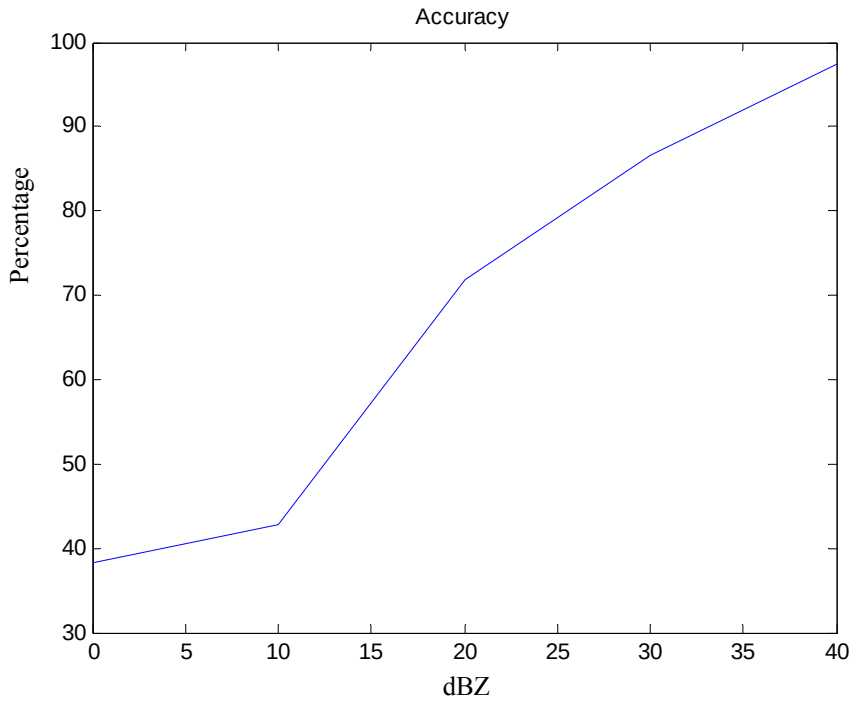


**Fig. 5.15 GVS results – Accuracy (Average of 15 images)**

Fig. 5.15 shows the plot for the average accuracy for all the fifteen test images, for the GVS results. As compared to the results of the proposed QC algorithm shown in Fig. 5.7, these average accuracies are lower for any given pixel intensity level.

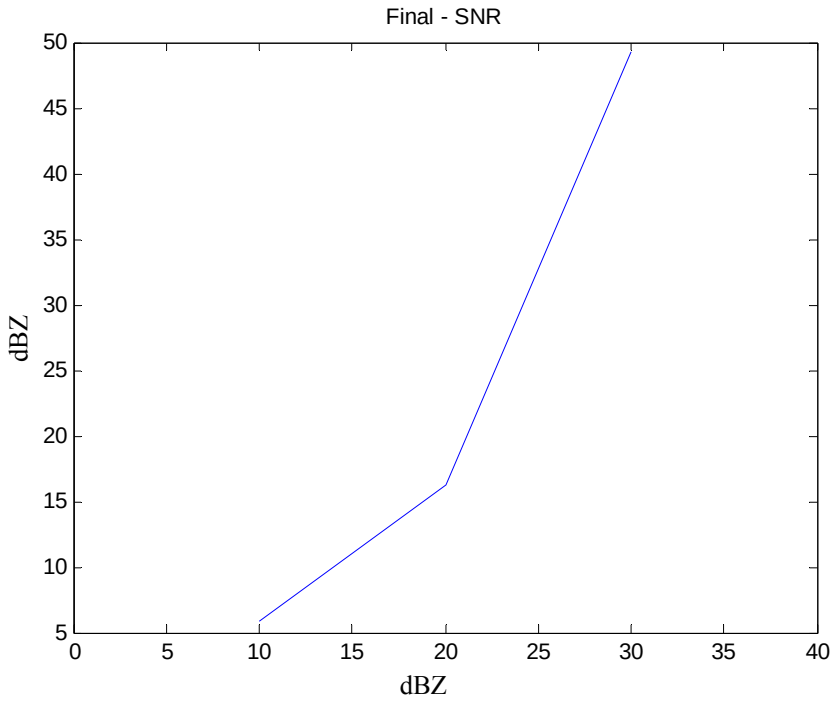


**Fig. 5.16 GVS results - SNR (Average of 15 images)**

Fig. 5.16 shows the plot for the average SNR for all the fifteen test images, for the GVS results. This figure also confirms that the average SNR is +∞ only for pixels with intensity greater than 30 dBZ as compared to the results of the proposed QC algorithm where the average SNR reaches +∞ after only 20 dBZ as seen in Fig. 5.8.

**Table 5.5 Comparison results between accurate rain event and QC algorithm in[1] for each test image**

| Test image 02:09 hrs | | | | |
|---|---|---|---|---|
| Range (dB) | Error misses (%) | Error false Alarms (%) | Accuracy (%) | SNR (dB) |
| **0 – 10** | 0 | 15.5057 | 84.4943 | -Inf |
| **10-20** | 5.2071 | 47.4556 | 47.3373 | -0.0291 |
| **20-30** | 14.378 | 11.9548 | 73.6672 | 6.1254 |
| **30-40** | 4.5296 | 6.6202 | 88.8502 | 10.5356 |
| **40-50** | 0 | 5.3763 | 94.6237 | 9.8206 |

| | | | | |
|---|---|---|---|---|
| Test image 04:09 hrs | | | | |
| **0 – 10** | 2.5523 | 18.0129 | 79.4348 | -4.9709 |
| **10-20** | 10.2419 | 30.9902 | 58.768 | 3.1277 |
| **20-30** | 6.6318 | 7.7661 | 85.6021 | 9.3048 |
| **30-40** | 2.3555 | 2.1413 | 95.5032 | 17.2044 |
| **40-50** | 0 | 1.7857 | 98.2143 | 23.8023 |
| Test image 05:09 hrs | | | | |
| **0 – 10** | 1.8807 | 23.1518 | 74.9676 | -5.9377 |
| **10-20** | 8.309 | 35.1082 | 56.5828 | 2.8005 |
| **20-30** | 5.3885 | 11.0276 | 83.584 | 8.9183 |
| **30-40** | 0.9396 | 1.8792 | 97.1812 | 18.2731 |
| **40-50** | 0.4808 | 0.4808 | 99.0385 | 17.7279 |
| Test image 07:09 hrs | | | | |
| **0 – 10** | 2.2803 | 35.4718 | 62.2479 | -6.0156 |
| **10-20** | 5.534 | 39.4297 | 55.0363 | 3.45 |
| **20-30** | 2.9429 | 7.3718 | 89.6853 | 11.6391 |
| **30-40** | 0.4796 | 2.558 | 96.9624 | 17.5778 |
| **40-50** | 0 | 2.6178 | 97.3822 | 17.5994 |
| Test image 08:09 hrs | | | | |
| **0 – 10** | 0 | 37.2907 | 62.7093 | -Inf |
| **10-20** | 2.0098 | 61.9085 | 36.0817 | 1.8148 |
| **20-30** | 3.1475 | 9.5759 | 87.2766 | 10.9073 |
| **30-40** | 0.5773 | 1.6677 | 97.755 | 16.6159 |
| **40-50** | 0 | 2.9268 | 97.0732 | 17.0067 |
| Test image 11:09 hrs | | | | |
| **0 – 10** | 3.1639 | 32.6586 | 64.1775 | -6.1155 |
| **10-20** | 5.4483 | 41.2723 | 53.2794 | 4.4687 |
| **20-30** | 3.5737 | 2.6424 | 93.7838 | 14.2818 |
| **30-40** | 0.9677 | 0.6452 | 98.3871 | 15.7334 |
| **40-50** | 1.4085 | 0 | 98.5915 | 27.2975 |

| | | | | |
|---|---|---|---|---|
| Test image 12:09 hrs | | | | |
| **0 – 10** | 10.2723 | 33.6777 | 56.0499 | -3.3068 |
| **10-20** | 7.7876 | 37.869 | 54.3433 | 3.2042 |
| **20-30** | 2.8377 | 8.1725 | 88.9898 | 12.1526 |
| **30-40** | 2.253 | 0.7799 | 96.9671 | 17.4108 |
| **40-50** | 0.8621 | 0 | 99.1379 | 21.7977 |
| Test image 14:09 hrs | | | | |
| **0 – 10** | 6.6558 | 35.6179 | 57.7264 | -2.7661 |
| **10-20** | 3.7327 | 27.1213 | 69.146 | 6.9468 |
| **20-30** | 1.4193 | 2.7227 | 95.8581 | 16.1915 |
| **30-40** | 1.335 | 1.0807 | 97.5842 | 13.924 |
| **40-50** | 0 | 0.5917 | 99.4083 | 29.9364 |
| Test image 15:09 hrs | | | | |
| **0 – 10** | 5.1706 | 34.2234 | 60.6061 | -2.8344 |
| **10-20** | 3.2148 | 21.0915 | 75.6936 | 8.6459 |
| **20-30** | 0.8568 | 2.4072 | 96.736 | 17.4158 |
| **30-40** | 0.5423 | 0.9941 | 98.4636 | 17.1223 |
| **40-50** | 0.7042 | 0.7042 | 98.5915 | 22.6017 |
| Test image 16:09 hrs | | | | |
| **0 – 10** | 9.8746 | 26.7479 | 63.3775 | -0.1608 |
| **10-20** | 4.0948 | 18.3767 | 77.5285 | 8.4944 |
| **20-30** | 1.811 | 2.2603 | 95.9286 | 14.84 |
| **30-40** | 0.6703 | 0.6094 | 98.7203 | 19.5421 |
| **40-50** | 0 | 0 | 100 | Inf |
| Test image 17:09 hrs | | | | |
| **0 – 10** | 2.2233 | 45.9448 | 51.8319 | -7.7629 |
| **10-20** | 1.6844 | 42.3426 | 55.973 | 5.2106 |
| **20-30** | 0.9248 | 3.8047 | 95.2704 | 15.1835 |
| **30-40** | 0.3887 | 1.4436 | 98.1677 | 14.4753 |
| **40-50** | 0 | 1.6393 | 98.3607 | 21.2187 |

| Test image 20:09 hrs | | | | |
|---|---|---|---|---|
| **0 – 10** | 9.411 | 29.9637 | 60.6253 | -0.3374 |
| **10-20** | 2.7401 | 17.4742 | 79.7858 | 9.9681 |
| **20-30** | 1.2324 | 3.2112 | 95.5563 | 14.55 |
| **30-40** | 0.2885 | 3.6538 | 96.0577 | 12.4698 |
| **40-50** | 0 | 8.6667 | 91.3333 | 9.3693 |
| Test image 21:09 hrs | | | | |
| **0 – 10** | 2.0316 | 40.2738 | 57.6947 | -2.8276 |
| **10-20** | 2.2735 | 20.7192 | 77.0072 | 9.5129 |
| **20-30** | 1.0202 | 2.2366 | 96.7432 | 16.2829 |
| **30-40** | 1.1617 | 1.7425 | 97.0958 | 14.9412 |
| **40-50** | 0.6803 | 0.6803 | 98.6395 | 26.4989 |
| Test image 22:09 hrs | | | | |
| **0 – 10** | 3.84 | 37.8464 | 58.3136 | -1.715 |
| **10-20** | 1.6869 | 17.2617 | 81.0514 | 10.553 |
| **20-30** | 0.9112 | 3.1387 | 95.9501 | 13.7862 |
| **30-40** | 0.4 | 2.4 | 97.2 | 17.4409 |
| **40-50** | 0 | 1.5504 | 98.4496 | 22.8224 |
| Test image 24:09 hrs | | | | |
| **0 – 10** | 8.0513 | 43.7253 | 48.2234 | -4.7041 |
| **10-20** | 3.4117 | 43.7344 | 52.8538 | 5.1336 |
| **20-30** | 0.9551 | 2.8805 | 96.1643 | 18.2211 |
| **30-40** | 0.493 | 0.2465 | 99.2605 | 26.1795 |
| **40-50** | 0 | 0 | 100 | Inf |

In table 5.5, the results for the miss errors, the false alarm errors, the accuracies and the SNRs for the entire fifteen test images are reported for the results of the QC algorithm proposed in [1]. All these results are also plotted in Figs. 5.17 to 5.20. Here also it can be observed that the overall accuracy is lower that that of the results of the proposed algorithm for any pixel intensity range. The overall errors are also higher than the corresponding errors in the results of the proposed algorithm. Similar relationship

between the performances can be observed between the two results while comparing the SNR results where the proposed algorithm exhibits an SNR of $+\infty$ more frequently than that of the QC algorithm proposed in [1].

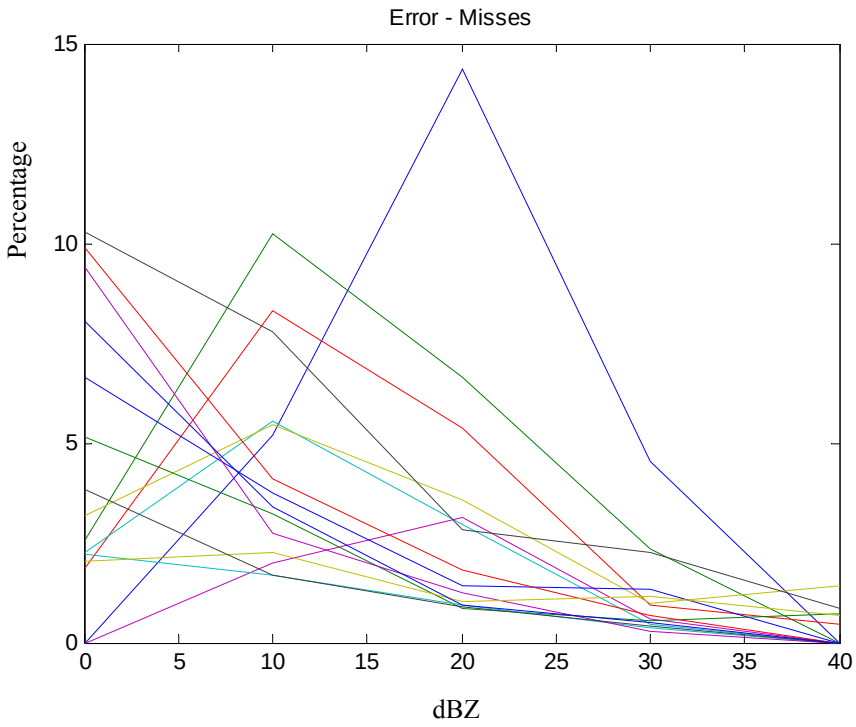


**Fig. 5.17 QC in[1] results - Percentage of misses**

Fig. 5.17 displays the compilation of plots of the percentages, for different image cases, when a pixel was actually a precipitation pixel according to the accurate rain event information and was mislabeled as a non-precipitation pixel, for the results of the QC algorithm proposed in [1]. As can been seen these results are comparable to those of the proposed QC algorithm.

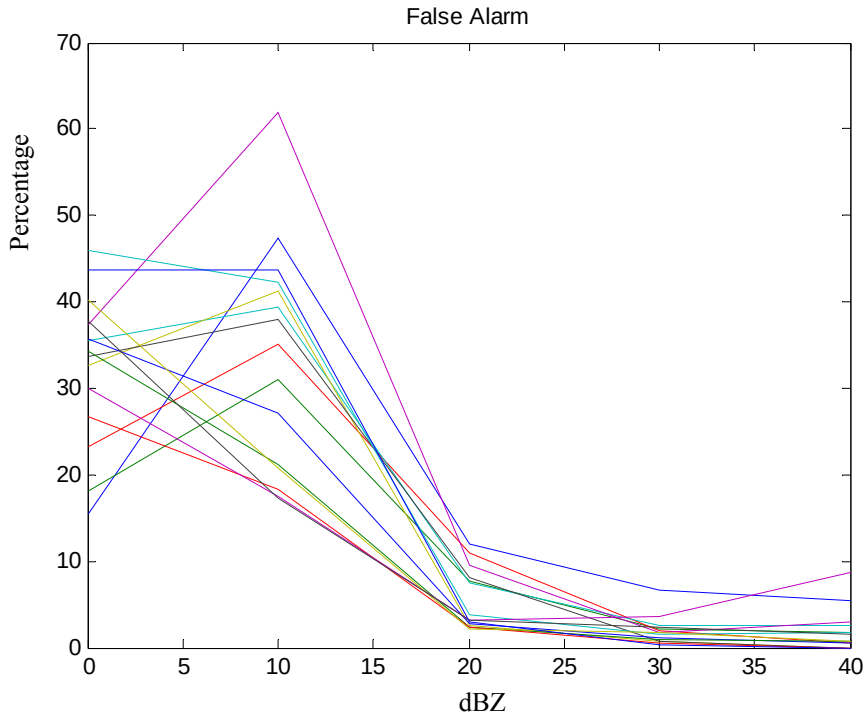


**Fig. 5.18 QC in [1] results - Percentage of False Alarms**

Fig. 5.18 displays the plots of the percentages, for different image cases, when a pixel was actually a non-precipitation pixel according to accurate rain events and was mislabeled as a precipitation pixel, for the results of the QC algorithm proposed in [1]. This plot shows that the false alarms are about 10 % for pixels with intensity of 20 dBZ. This is inferior as compared to the results of the proposed QC algorithm where, as seen in Fig. 5.2, the false alarms are under 5 % for pixels with intensity of 20 dBZ.

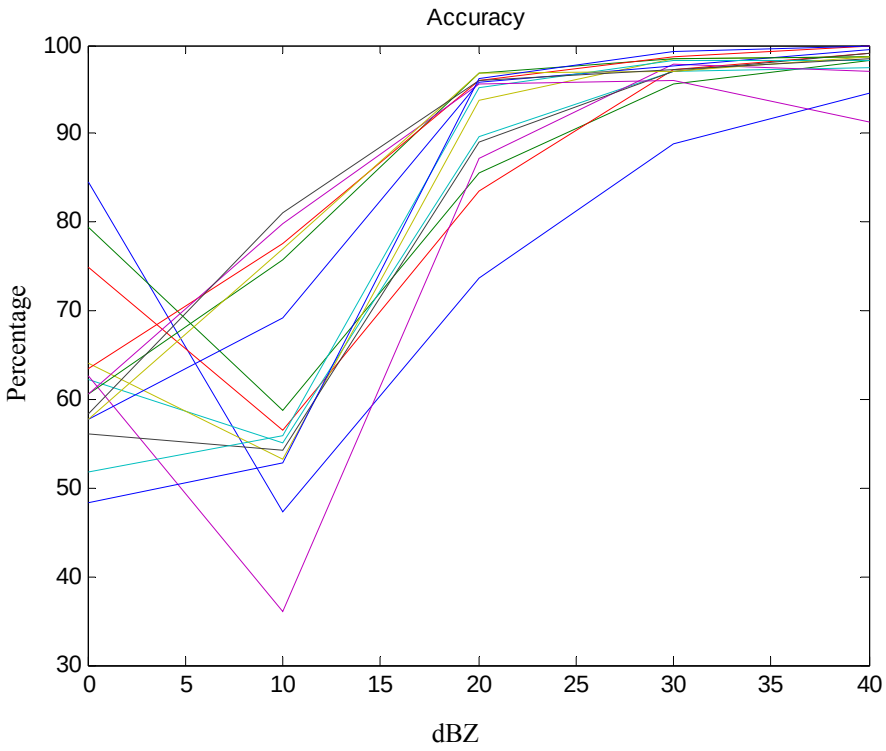


**Fig. 5.19 QC in [1] results – Accuracy**

Fig. 5.19 displays the plots of the percentages, for different image cases, when a pixel was actually a precipitation pixel according to the accurate rain event and was correctly labeled as a precipitation pixel, or when a pixel was actually a non-precipitation pixel according to the accurate rain event and was labeled appropriately as a non-precipitation pixel, for the results of the QC algorithm proposed in [1]. Here it can be observed that the overall accuracies don't rise beyond 95% where as from Fig. 5.3 it can be seen that the accuracies rise past 95 %.

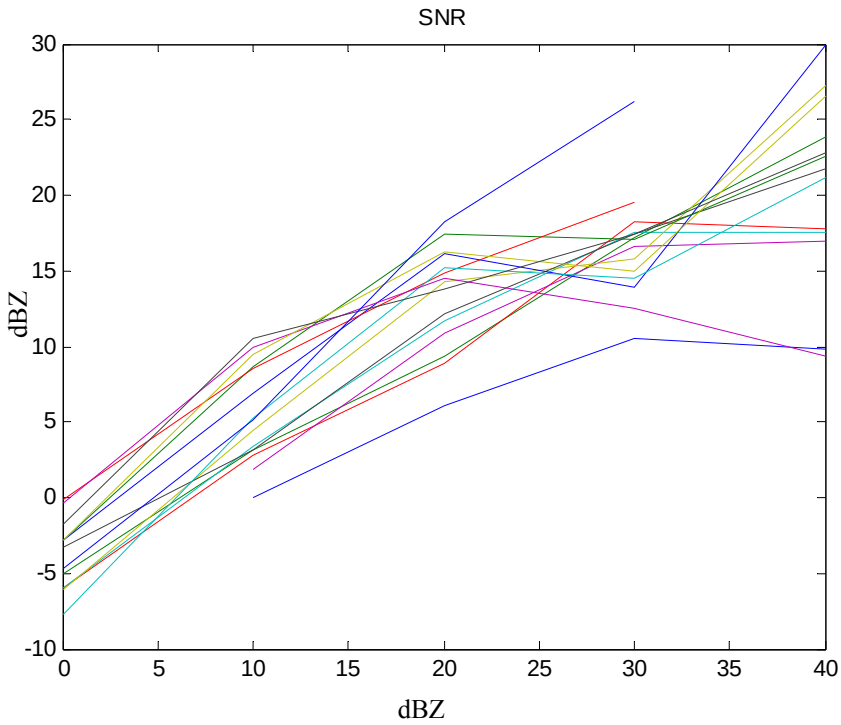


**Fig. 5.20 QC in [1] results – SNR**

Fig. 5.20 displays the plots of the signal to noise ratios (SNR), for different image cases, for the results of the QC algorithm proposed in [1]. Here the precipitation in the accurate rain event image is considered as the signal and the difference in the final result image and the ground truth is considered as the noise. Most the images exhibit finite SNR as seen in the plot above, which indicates some residual error. However, in the proposed QC algorithm, most of the cases do not have any errors, which are demonstrated by an infinite SNR as seen ion Fig. 5.4.

**Table 5.6 Comparison results between accurate rain event and QC algorithm [1] results for testing set (average of 15 test image)**

| Testing Set | | | | |
|---|---|---|---|---|
| Range (dB) | Error misses (%) | Error false Alarms (%) | Accuracy (%) | SNR (dB) |

| | | | | |
|---|---|---|---|---|
| **0 – 10** | 4.494 | 32.674 | 62.832 | -Inf |
| **10-20** | 4.492 | 33.477 | 62.031 | 5.554 |
| **20-30** | 3.202 | 5.412 | 91.386 | 13.320 |
| **30-40** | 1.159 | 1.897 | 96.944 | 16.630 |
| **40-50** | 0.276 | 1.801 | 97.923 | Inf |

In table 5.6, the averages for the miss errors, false alarm errors, accuracies and SNR's for the fifteen test images are presented for the QC algorithm proposed in [1]. These results, also plotted in Figs. 5.21 to 5.24, also support the comparison drawn above.

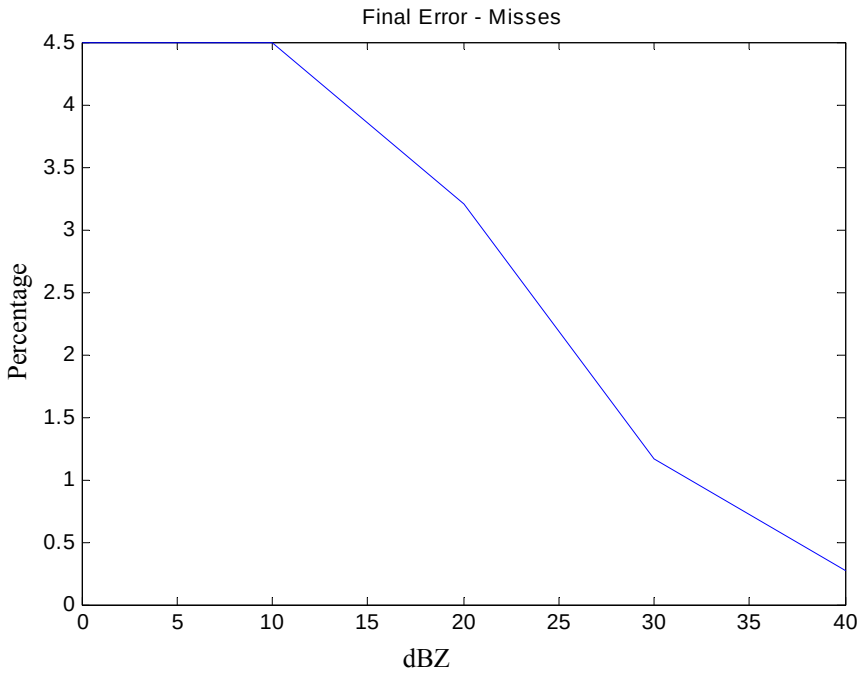


**Fig. 5.21 QC in [1] results - Percentage of misses (Average of 15 images)**

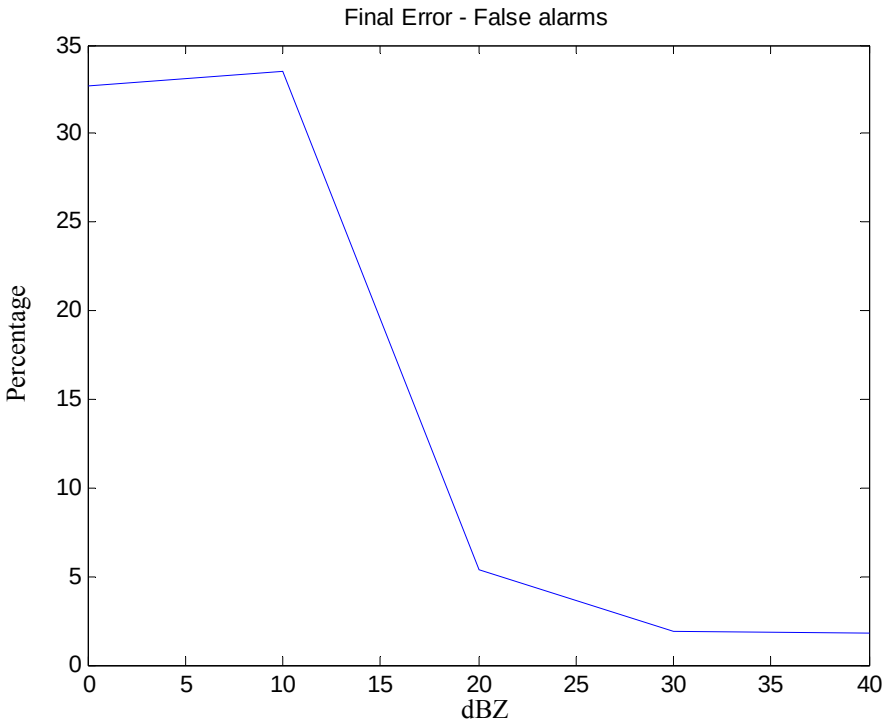


**Fig. 5.22 QC in [1] results - Percentage of False Alarms (Average of 15 images)**

Fig. 5.22 shows the plot for the average false alarm error for all the fifteen test images, for the results of the QC algorithm proposed in [1]. Again this figure shows that these results are inferior as compared to those of the proposed QC algorithm as seen in Fig. 5.6.

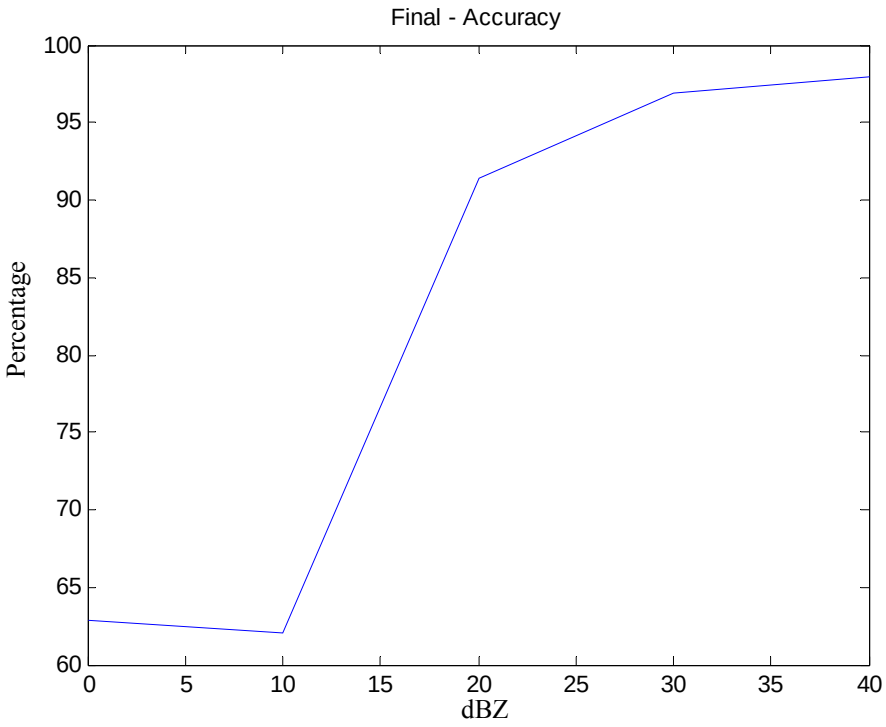


**Fig. 5.23 QC in [1] results – Accuracy (Average of 15 images)**

Fig. 5.23 shows the plot for the average accuracy for all the fifteen test images, for the results of the QC algorithm proposed in [1]. As compared to the results of the proposed QC algorithm shown in Fig. 5.7, these average accuracies are lower for any given pixel intensity level.

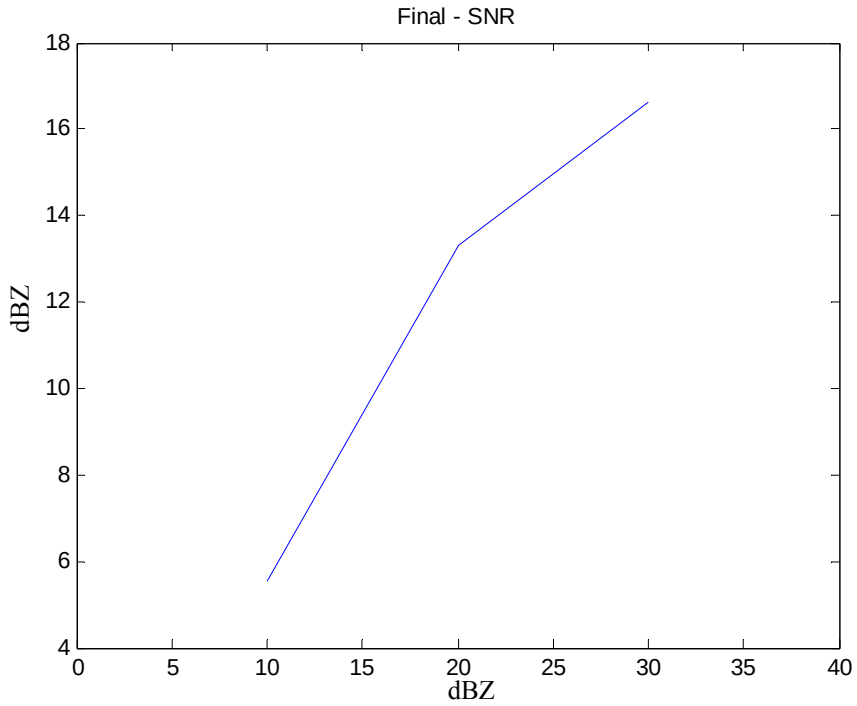


**Fig. 5.24 QC in [1] results - SNR (Average of 15 images)**

Fig. 5.24 shows the plot for the average SNR for all the fifteen test images, for the results of the QC algorithm proposed in [1]. This figure also confirms that the average SNR is +∞ only for pixels with intensity greater than 30 dBz as compared to the results of the proposed QC algorithm where the average SNR reaches +∞ after only 20 dBz as seen in Fig. 5.8.

**Table 5.7 Rain rates for test results using different algorithms**

| **Images** | | | **QC algorithm** | | |
|---|---|---|---|---|---|
| *Hrs* | *Original Reflectivity Images* | *Accurate Rain Events* | *GVS* | *QC [1]* | *Proposed* |
| 0219 | 0.0056 | 0.0013 | 0.002 | 0.0025 | 0.0018 |
| 0419 | 0.0077 | 0.0033 | 0.0042 | 0.0044 | 0.0037 |
| 0519 | 0.0094 | 0.0045 | 0.0061 | 0.0062 | 0.0055 |

| | | | | | |
|---|---|---|---|---|---|
| 0719 | 0.0149 | 0.0085 | 0.0113 | 0.0119 | 0.0111 |
| 0819 | 0.0166 | 0.0078 | 0.0115 | 0.0131 | 0.0115 |
| 1119 | 0.0211 | 0.0123 | 0.0163 | 0.0169 | 0.0158 |
| 1219 | 0.0205 | 0.0119 | 0.0148 | 0.0162 | 0.0146 |
| 1419 | 0.0249 | 0.0178 | 0.0201 | 0.0216 | 0.0205 |
| 1519 | 0.0265 | 0.0203 | 0.0231 | 0.0235 | 0.022 |
| 1619 | 0.0302 | 0.0229 | 0.0251 | 0.0258 | 0.0243 |
| 1719 | 0.0342 | 0.0207 | 0.0282 | 0.03 | 0.0274 |
| 2019 | 0.0313 | 0.0222 | 0.0219 | 0.0267 | 0.0219 |
| 2119 | 0.0291 | 0.0182 | 0.0184 | 0.0244 | 0.0181 |
| 2219 | 0.0311 | 0.0221 | 0.0223 | 0.0275 | 0.0229 |
| 2419 | 0.0266 | 0.0164 | 0.0198 | 0.0234 | 0.0195 |

Table 5.7 shows the closeness of the results of the proposed algorithm and the GVS results in terms of the rain rate. As observed here, the proposed algorithm produces results much closer to the GVS results as compared to the results of the QC algorithm proposed in [1]. This is also shown in Fig. 5.25

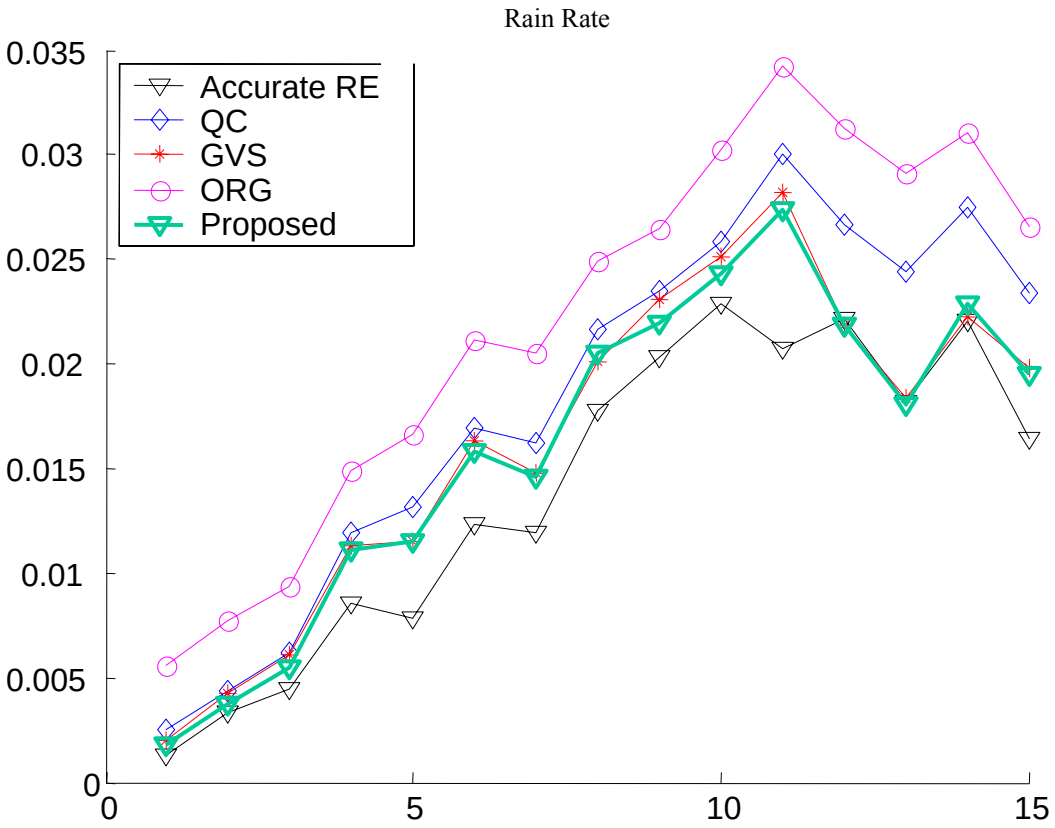


**Fig. 5.25 Rain rates**

All the tables essentially list the results that are also plotted in the corresponding figures. The various colors represent results from different images. The final results are the averages of the results of all the fifteen test images for the corresponding statistic. As seen from Figs. 5.1, 5.2, 5.5 and 5.6, the misses and false alarms drop rapidly as the intensity of the pixels increase. These errors indicate the percentage of instances that a pixel was mislabeled. This demonstrates that the algorithm works almost perfectly for high intensity pixels. This is favorable as the precipitation events exhibit high intensity values in the radar images. This is also observed from the accuracy plots of all the images and the mean accuracy plots as seen in Figs. 5.3 and 5.7, respectively. The accuracy indicates the percentage of instances when a pixel was correctly labeled. From Fig. 5.7 it is observed that the accuracy rises up to 98.95% for the proposed algorithm. Also as seen from Figs. 5.4 and 5.8, the SNR plots for all the images and the mean SNR plots show a steady increase in performance of the algorithm as the intensity of the pixels increase. A

point to be noted in these SNR plots is the abrupt starting and abrupt ending of the some curves. At the start, this due to the fact that the SNR is -∞ and at the end it is due to the fact that the SNR is +∞. It is easily noted from the maximum attainable accuracies as seen in Figs. 5.7, 5.15 and 5.23, that the proposed algorithm works better that the QC algorithm in [1] and the results are better than the GVS results. As seen in Fig 5.25, the rain rate plot shows the closeness or accuracy on the results of the proposed algorithm w.r.t the GVS results. It is observed that the original image and the results of the QC algorithm in [1] are over-estimates of the rain-events and that the proposed algorithm produces results as close as possible to the GVS results.

# CHAPTER 6

# 6. CONCLUSION

As the tables suggest, the result of the proposed QC algorithm dramatically improve with increasing dB levels of the pixel intensity. The general trend of the error rate (false alarms and misses) is that they decrease as the range of intensity values increases. Also, the percentage of false alarms is lesser than the GVS results for high intensity ranges. Though, the misses are higher at lower intensity levels in comparison with the GVS results, they are not of much significance as it is well known that rain events are more likely to be present with intensities greater than 20dB. The overall average accuracy of the proposed algorithm reaches as high as 98.95%. The signal-to-noise ratio values endorse the superior performance of the proposed QC algorithm for accurate rainfall detection. For the proposed algorithm the average false alarm drops to 1.09%, average miss drops to 0.00% and the average accuracy rises to 98.95% whereas, in the GVS results the average false alarm drops to 1.80%, average miss drops to 0.00% and the average accuracy goes up to 97.46%. Also for the QC algorithm proposed in [1], the average false alarm drops to 1.8%, the average misses drops to 0.28% and the average overall accuracy goes upto 97.92%. These figures indicate the superior performance of the proposed algorithm. Another fact to be observed from the rain rate plots is that the proposed algorithm generates results as close as possible to the GVS results. This trend is observed in general for all the 15 test images used. This is another indication that the proposed algorithm produces more accurate results w.r.t. the GVS results than the QC algorithm proposed in [1] which overestimates the rain.

As observed from the various tables above, the misses for the lower intensity pixels are high. This can be attributed to the following fact. Normally precipitation shows up as a high reflectivity (dB) value on the image. While training the algorithm some of the low intensity pixels were considered as non-precipitation. This was done to avoid over training of the algorithm, else though the algorithm would work perfectly for the training data, it would not be robust enough to accurately process any given image. Thus the

various thresholds were chosen accordingly. This led to some misclassifications in terms of misses.

Another important fact to be noted is that the proposed algorithm uses multifractals based on only the second power of the average images as compared to those based using the power of eight in the QC algorithm proposed in [1]. The proposed algorithm uses the textural directionality via Gabor wavelet analysis to extract more useful information. Also, optical implementation of correlation was used to speed up the filtering stage for the above.

From the results presented in the tables above, it can be concluded that the proposed algorithm successfully detects the rain events from the radar images. Also these results show that the proposed algorithm performs as good as or better that the QC algorithm proposed in [1].

## FUTURE WORK

In this thesis most of the mathematical operations were done digitally. It would be of advantage to investigate optical method of performing these operations. Also, performing the thresholding operation optically would aid to make the system completely optical. Due to computational expense only second power of the filtered images were used to create multifractals. Higher powers of the images should be investigated to increase the robustness of the system. The limited scope of the thesis work allowed investigation of only Gabor wavelets for textural analysis. There are many other wavelets in the literature that are used for analysis of similar operations that need to be incorporated. Different type of thresholding techniques should be used for the decision-making stages.

# REFERENCES


[1] Dimitrios Charlampidis, Takis Kasparis, W. Linwood Jones, "Removal of Non precipitation Echoes in Weather Radar Using Multifractals and Intensity," *IEEE transaction son Geoscience and remote sensing*, Vol. 40, No. 5, May 2002

[2] J.W.Goodman, "Introduction to Fourier Optics," Mc Graw Hill Company, New York, 1965.

[3] "WSR-88D Radar Imagery**,** " ; http://ww2010.atmos.uiuc.edu/(Gl)/wwhlpr/radar_echos.rxml?hret=/indexlist.rxml

[4] "Interpreting Weather Watch Radar Images," Commonwealth of Australia 2004, Bureau of Meteorology ; http://mirror.bom.gov.au/weather/radar/radarexp.shtml

[5] V Lakshmanan, Kurt Hondl, Gregory Stumpf, Travis Smith, "Quality Control of WSR-88D Reflectivity Data".

[6] J. Keeler, C. Kessinger, S. Ellis, and J. VanAndel, "AP clutter detection and mitigation: NEXRAD implementation plan," in *Proc. 29th AMS Int. Conf. Radar Meteorology*, Montreal, QC, Canada, 1999.

[7] Dr. Abdul Rehman Alsamman, "Ultra fast Face Recognition "

[8] "Radar Imagery Basics," 2004 ; http://www.mnsu.edu/weather/wx_WALTER/Modules/Radar/radar_edu.html

[9] "Doppler Weather Radar Overview," 2004; http://www.nwas.org/committees/avnwinterwx/doppler_weather_radar_overview.htm

[10] "The 1C-51 Radar Data Quality Control Algorithm Description ";
**http://trmm.gsfc.nasa.gov/TRMMGV/1C51.html**

[11] Cathy Kessinger, Scott Ellis, and Joseph Van Andel, " The Radar Echo Classifier: A Fuzzy Logic Algorithm For The WSR-88D **"**

[12] David B. Wolff, "TRMM GT Radar/Raingauge Data Quality Contro," 1994; http://trmm-fc.gsfc.nasa.gov/trmm_gv/software/qc/qc.html#QC

[13] N.Sarkar and B.B. Chaudhuri, "Multifractal and generalized dimensions of gray-tone digital image," *Signal Process.*, vol. 42, pp. 181–190, 1995

[14] J. Arrault, A. Arneodo, A. Davis, and A. Marsak, "Wavelet based multifractal analysis of rough surfaces :Application to cloud models and satellite data," *Phys. Rev. Lett.*, vol. 79, no. 1, pp. 75–79, July 7, 1997.

[15] M. Alber and J. Peinke, "Improved multifractal box-counting algorithm, virtual phase transitions, and negative dimensions," *Phys. Rev. E*, vol. 57, no. 5, pp. 5489–5493, May 1998.

[16] M. Dekking, J.L. Vehel E. Lutton, and C. Tricot, *Fractals: Theory and Applications in Engineering.* London, U.K.: Springer-Verlag, 1999

[17] Dunn, D. and Higgins, W.E., "Optimal Gabor filters for Texture Segmentation," *IEEE Transactions on Image Processing*, Vol. 4, No. 7, pp. 947-964, Jul 1995.

[18] Dengsheng Zhang, Guojun Lu, "Content-based image retrieval using Gabor texture features", *In Proc. Of First IEEE Pacific- rim Conference on Multimedia (PCM"00)*, pp.1-9, Fargo, ND, USA, June 1-3, 2001.

[19] B.S.Manjunath and W.Y. Ma, "Texture features for browsing and retrieval of image data", *IEEE Transactions on Pattern Analysis and Machine Intelligence (PAMI)*, vol.18, no.8, pp.837-42, Aug 1996.

[20] R.O.Duda, P. E. Hart and David G. Stork "Pattern Classification (2nd ed)" Wiley, New York. NY, 2000

[21] WSI Corporation**, "**An Overview of NEXRAD Products," 1994; http://sysu1.wsicorp.com/unidata/intro.html

[22] Yoram Kaufman , "Weather Forecasting through the ages," ; http://earthobservatory.nasa.gov/Library/WxForecasting/wx2.html

[23] "Forecasting,"; http://weathereye.kgan.com/cadet/forecast/forecasting.html

[24] Dr Jeffrey B. Halverson , Dr. Robert Adler, "General Performance of a Radar Data Quality Control Algorithm," ; http://trmm.gsfc.nasa.gov/jcetop/QC_alg_performance.html

[25] Lianping Chen, Guojun Lu, Dengsheng Zhang, "Effects of Different Gabor Filter Parameters on Image Retrieval by Texture," Gippsland *School of Computing and Information Technology, Monash University, Churchill, Victoria, 3842, Australia*

[26] Bradley g. boone, "Signal Processing using Optics: Fundamentals, Devices, Architectures, and Applications". Oxford, New York, 1998

[27] Joseph Shamir, "Optical computing remains in shadow**",** EE Times July 17, 2000

[28] J. W. Goodman, "Introduction to Fourier Optics," McGraw-Hill, 1996

# APPENDIX

time: 02 09 hrs

Reflectivity Image elevation 1

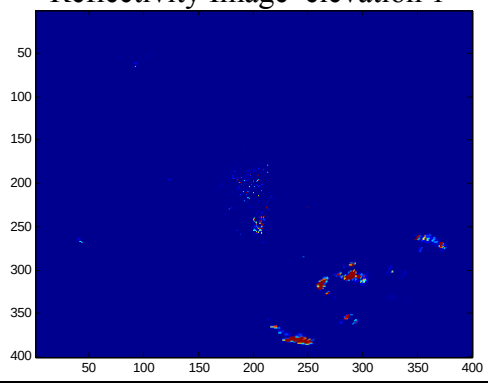


Reflectivity Image elevation 1

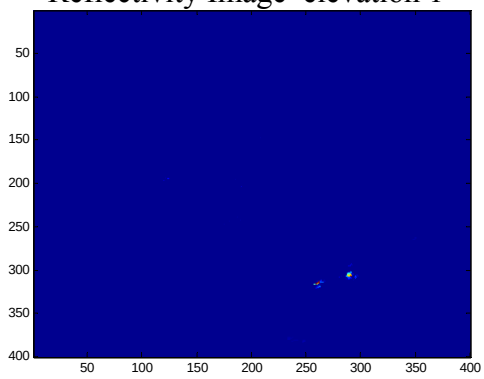


Final output after step 5

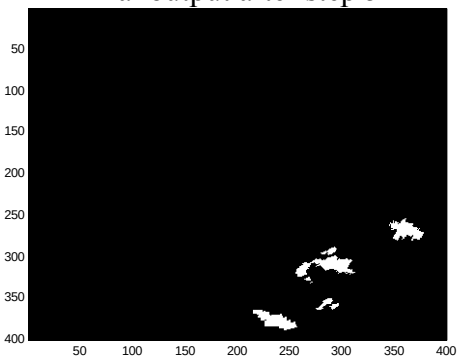


Final output

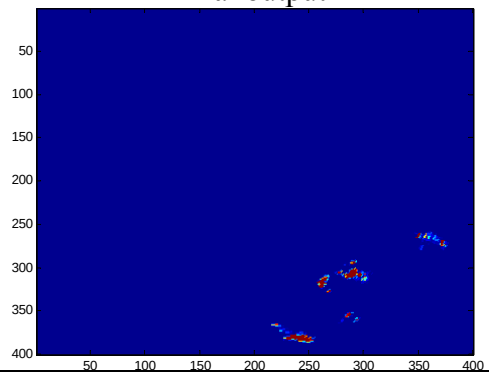


Accurate Rain Event

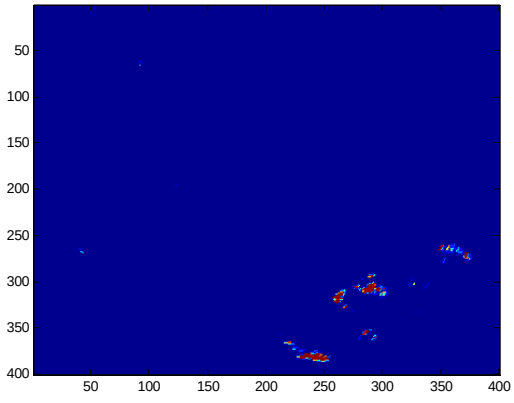

time: 04 09 hrs

Reflectivity Image elevation 1

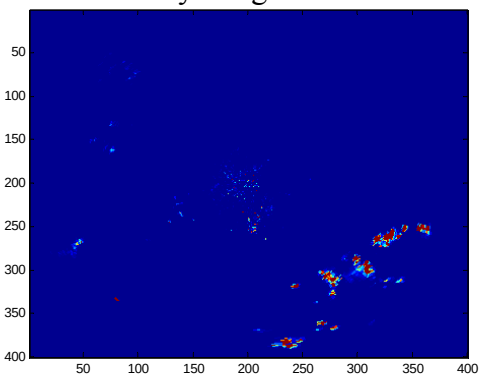


Reflectivity Image elevation 2

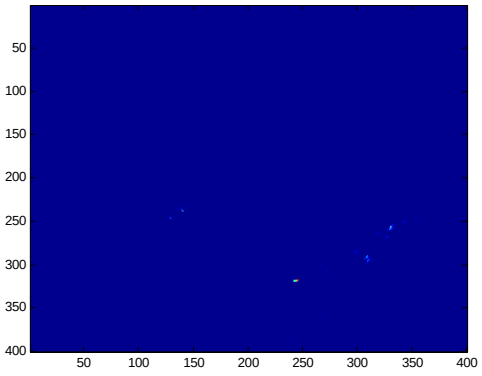


Final output after step 5

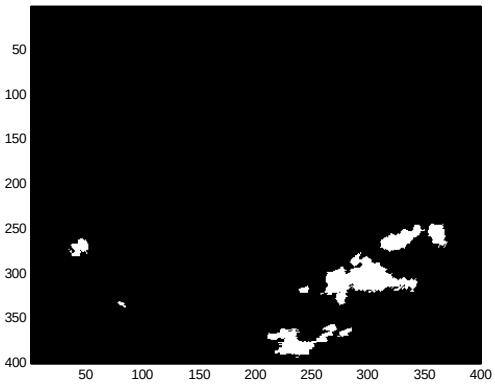


Final Output

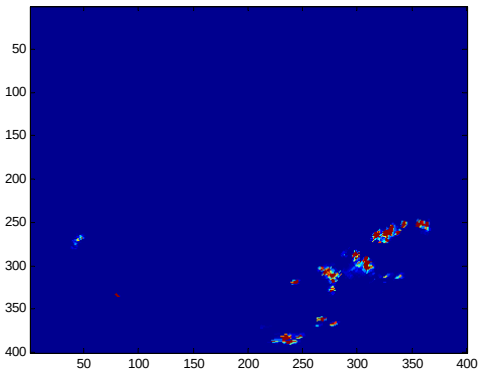


Accurate Rain Event

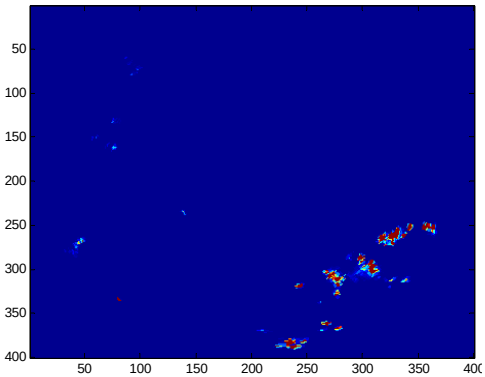

time: 05 09 hrs

Reflectivity Image elevation 1

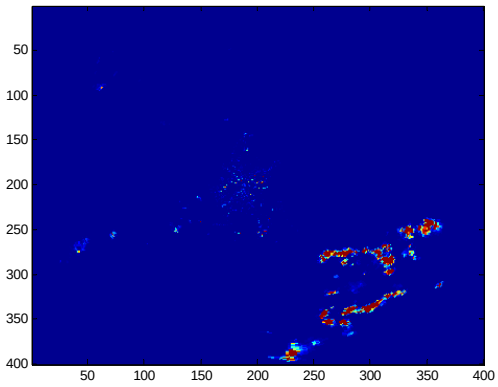


Reflectivity Image elevation 1

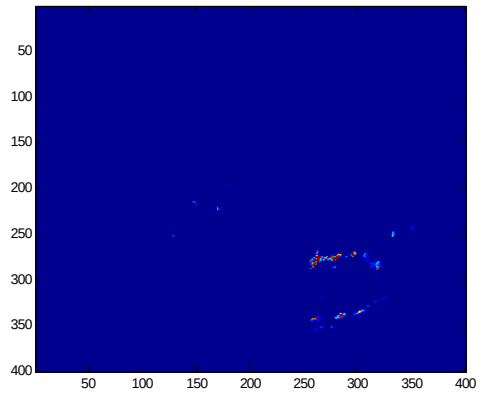


Final output after step 5

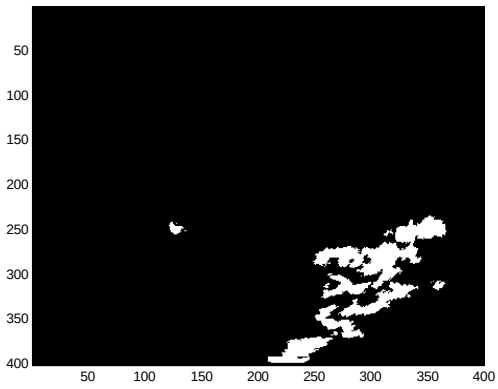


Final Output

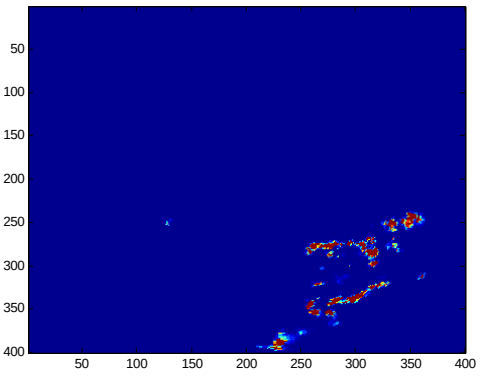


Accurate Rain Event

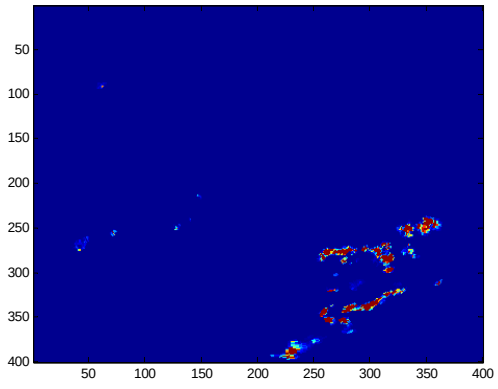

time: 07 09 hrs

Reflectivity Image elevation 1

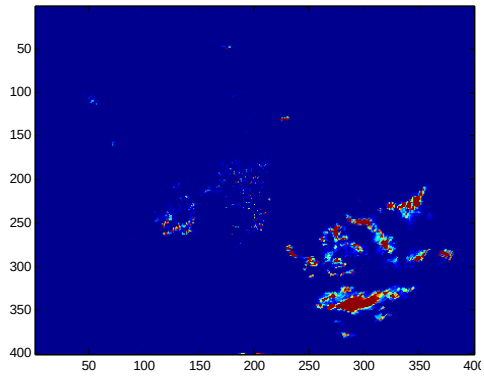


Reflectivity Image elevation 2

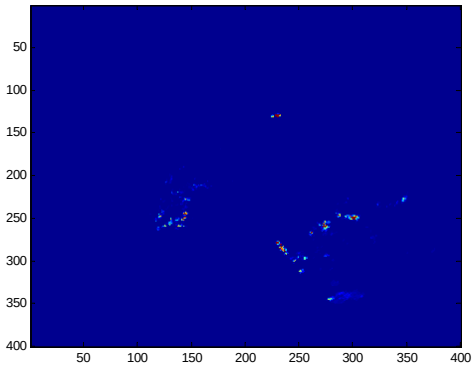


Final output after step 5

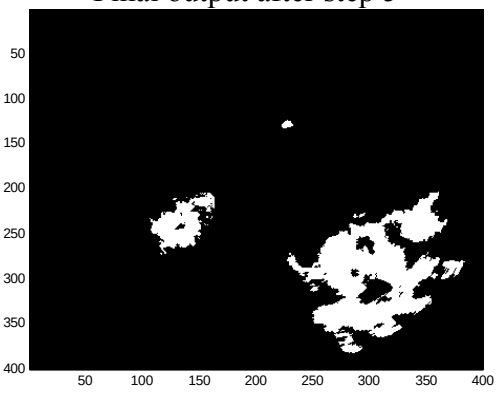


Final Output

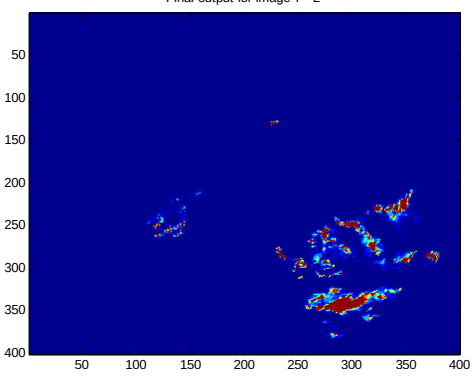


Accurate Rain Event

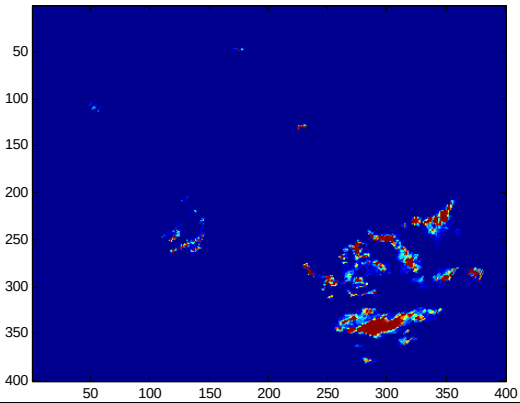

time: 08 09 hrs

Reflectivity Image elevation 1

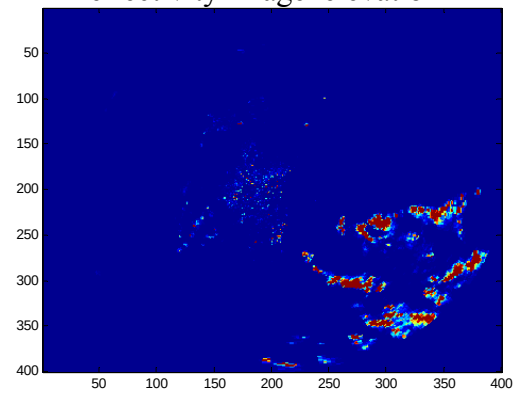


Reflectivity Image elevation 2

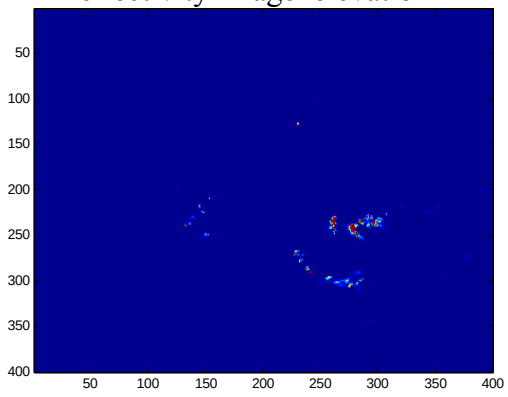


Final output after step 5

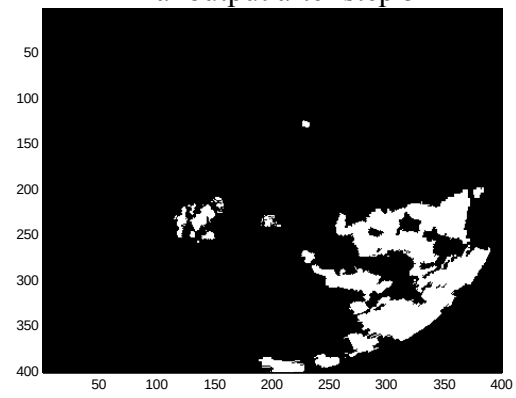


Final Output

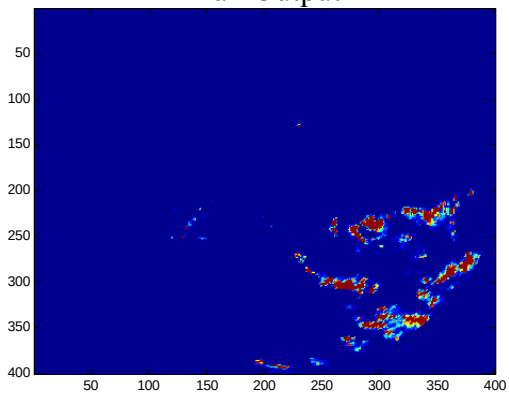


Accurate Rain Event

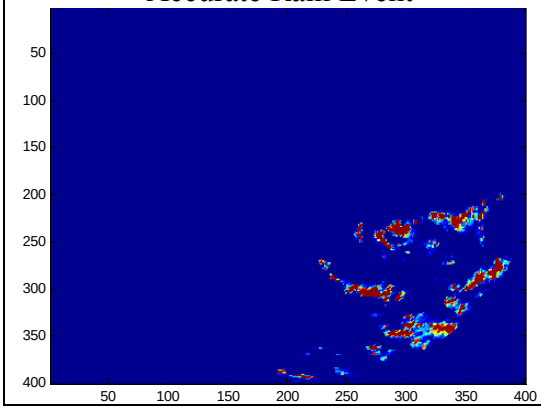

time: 11 09 hrs

Reflectivity Image elevation 1

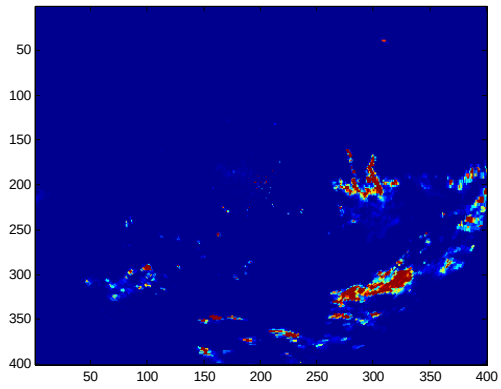


Reflectivity Image elevation 2

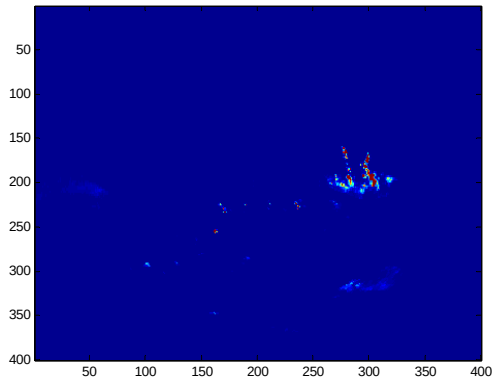


Final output after step 5

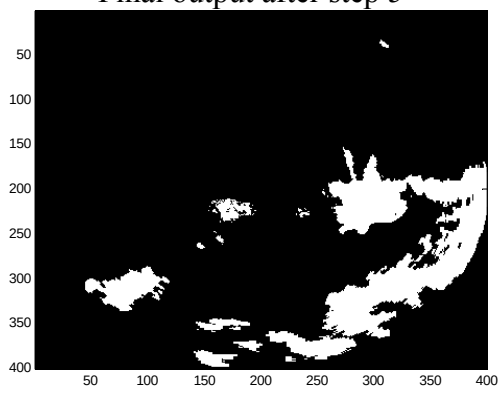


Final Output

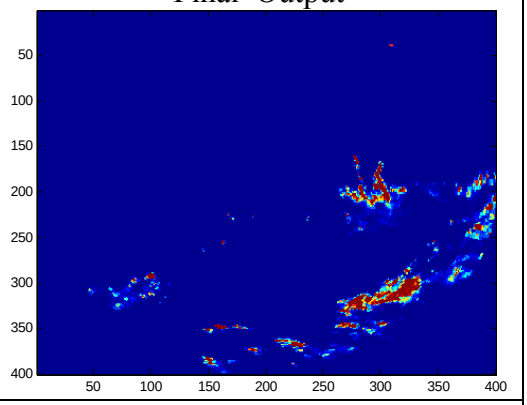


Accurate Rain Event

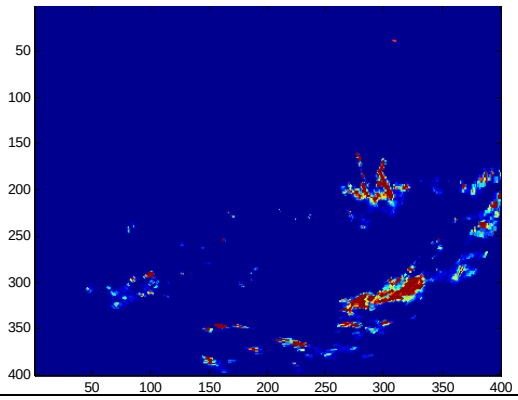

time: 12 09 hrs

Reflectivity Image elevation 1

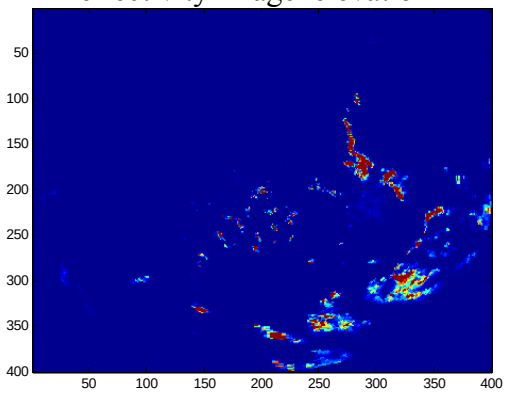


Reflectivity Image elevation 2

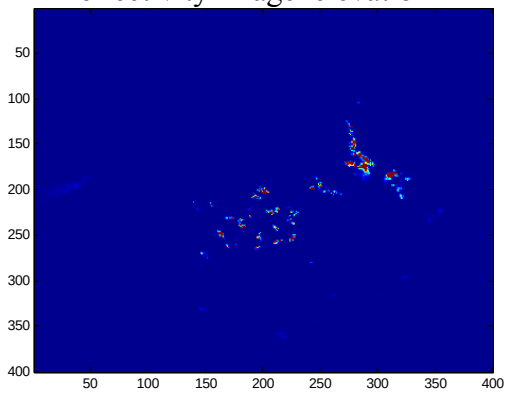


Final output after step 5

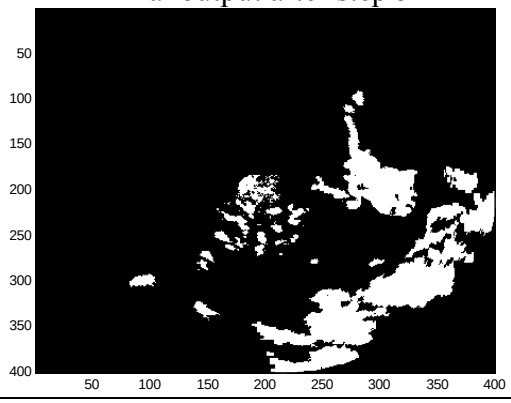


Final Output

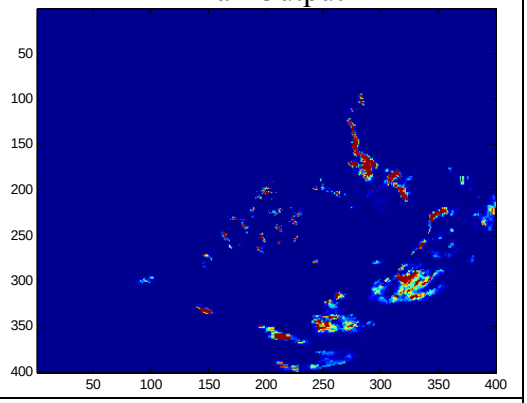


Accurate Rain Event

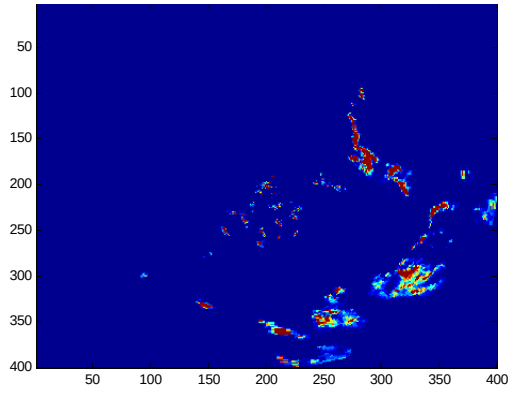

time: 14 09 hrs

Reflectivity Image elevation 1

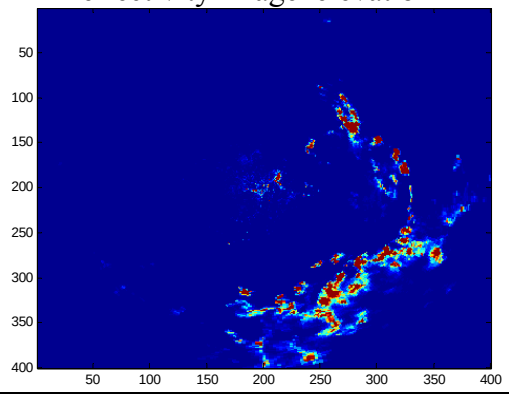


Reflectivity Image elevation 2

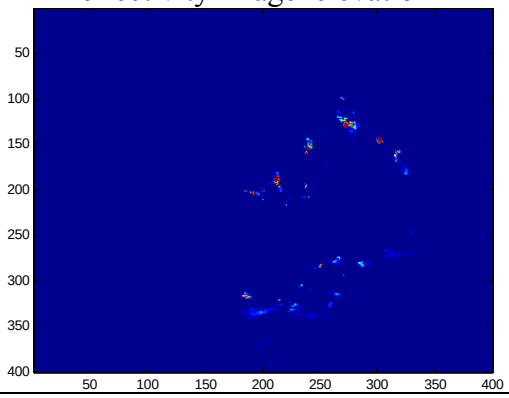


Final output after step 5

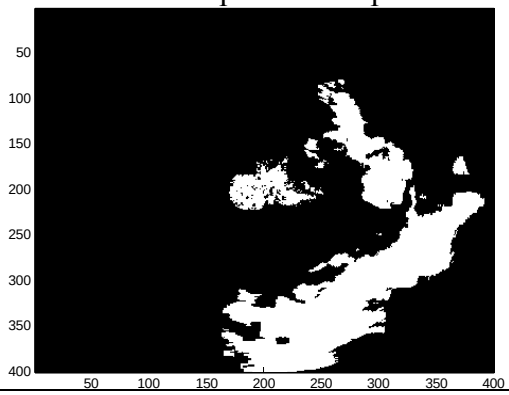


Final Output

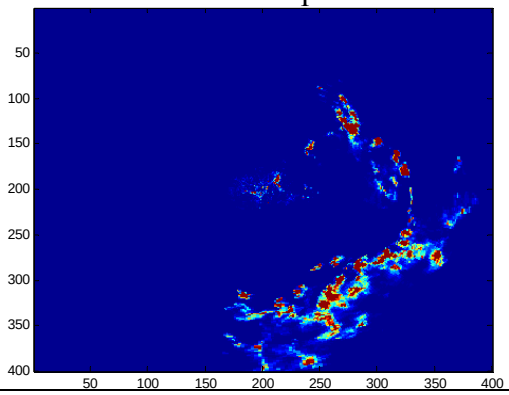


Accurate Rain Event

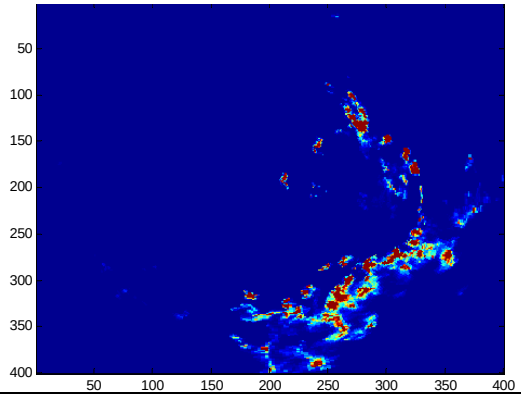

time: 15 09 hrs

Reflectivity Image elevation 1

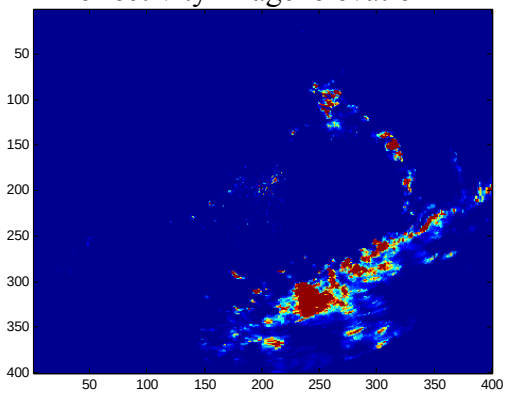


Reflectivity Image elevation 2

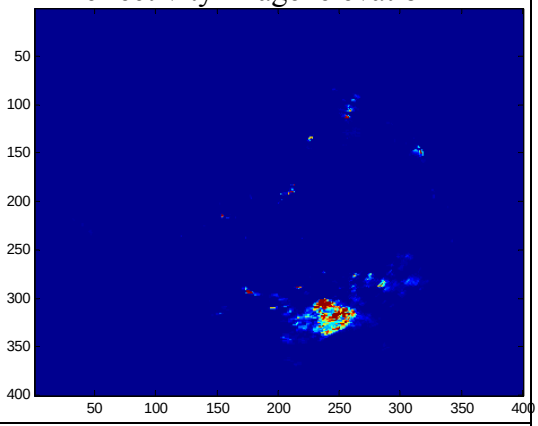


Final output after step 5

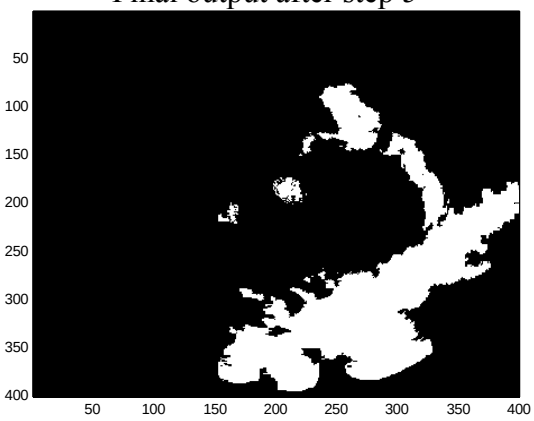


Final Output

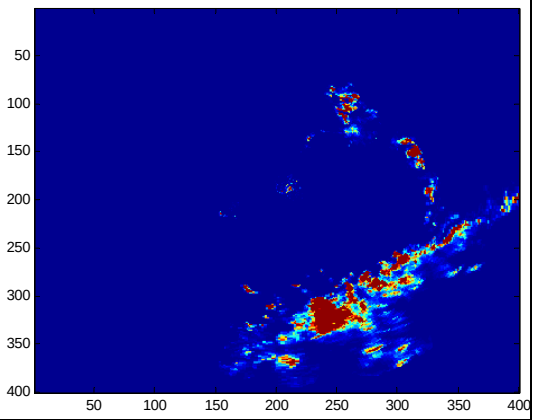


Accurate Rain Event

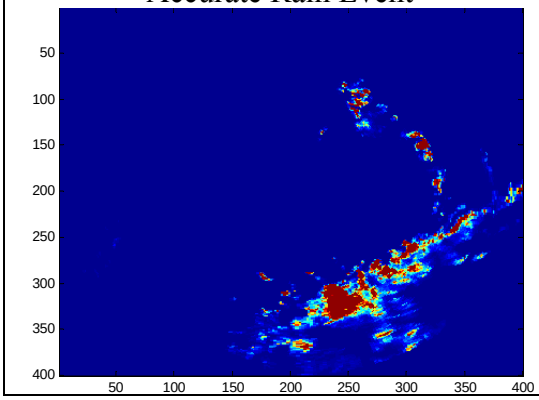

time: 16 09 hrs

Reflectivity Image elevation 1

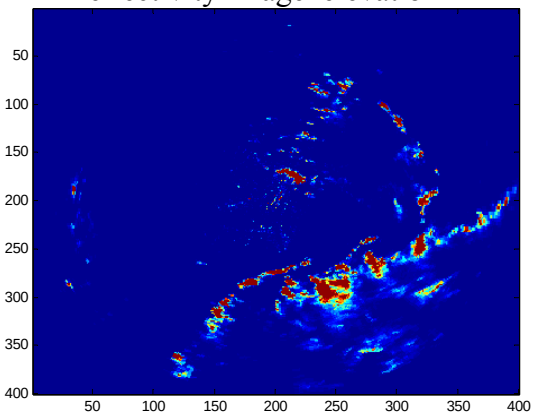


Reflectivity Image elevation 2

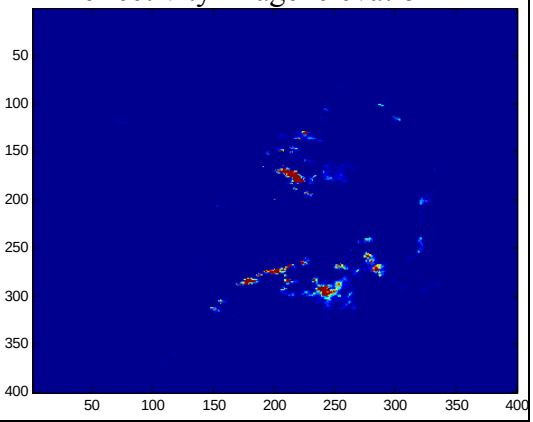


Final output after step 5

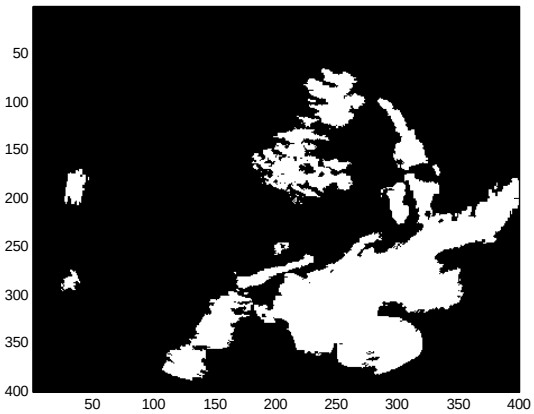


Final Output

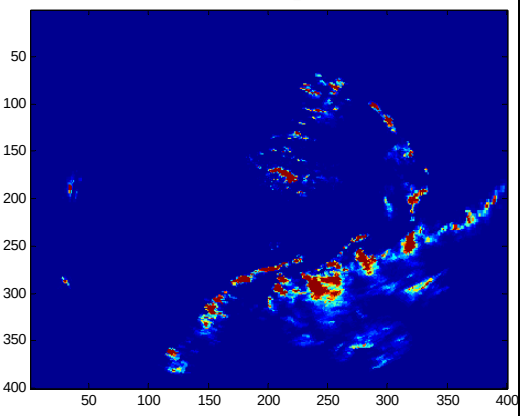


Accurate Rain Event

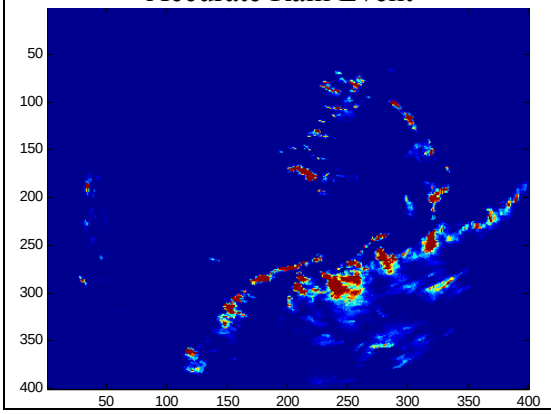

time: 17 09 hrs

Reflectivity Image elevation 1

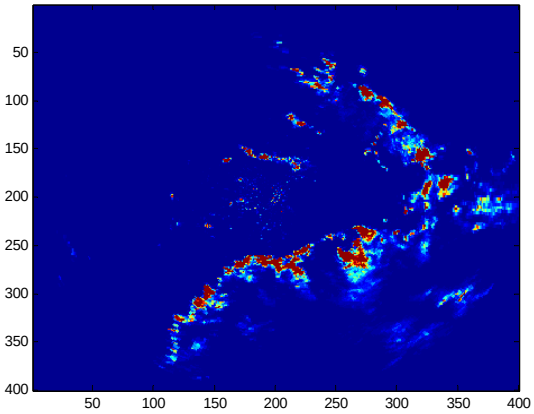


Reflectivity Image elevation 2

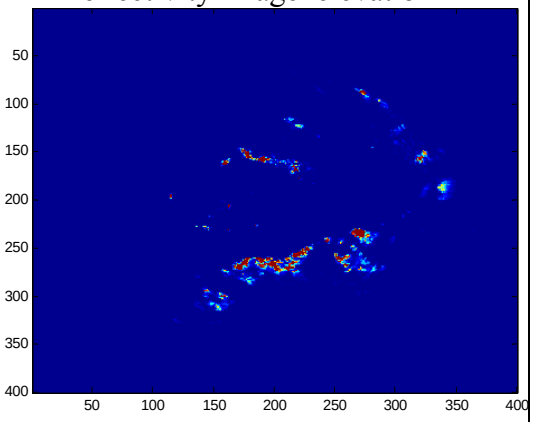


Final output after step 5

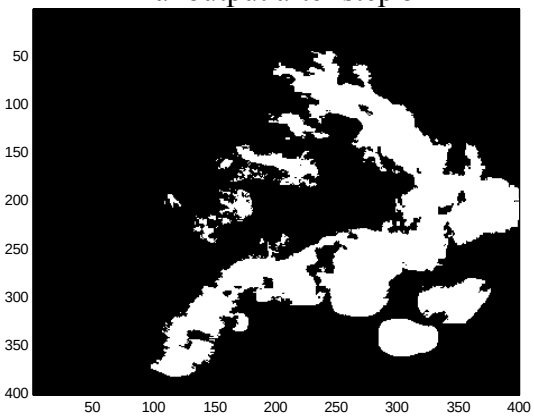


Final Output

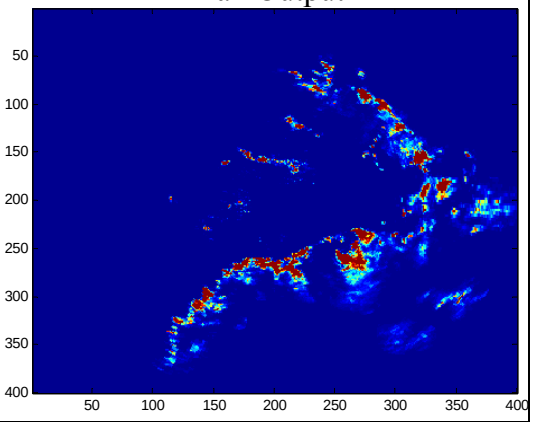


Accurate Rain Event

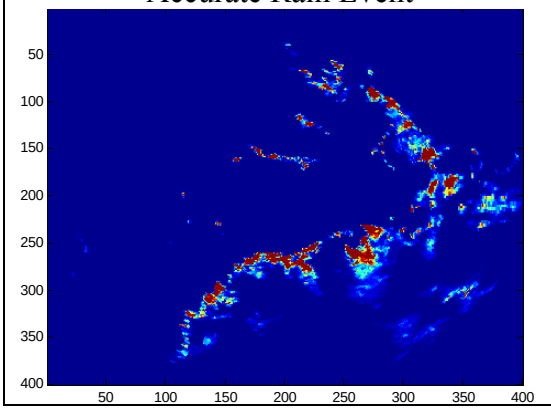

time: 20 09 hrs

Reflectivity Image elevation 1

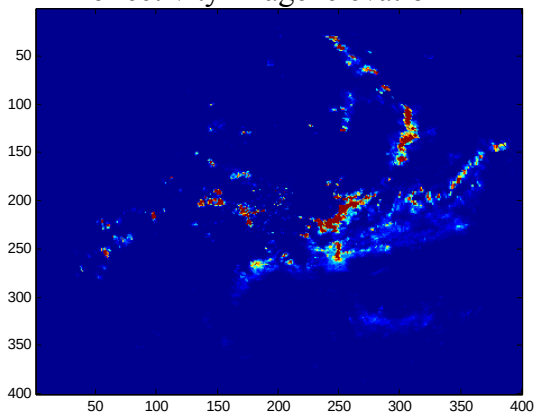


Reflectivity Image elevation 2

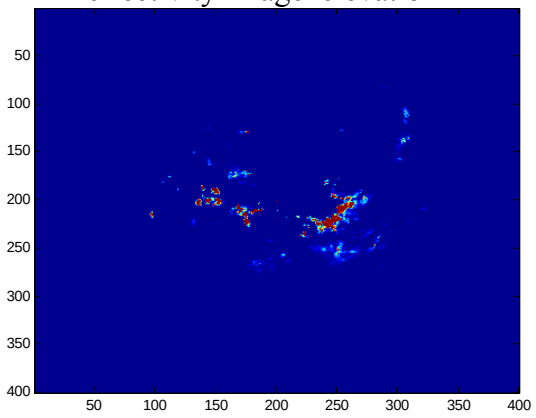


Final output after step 5

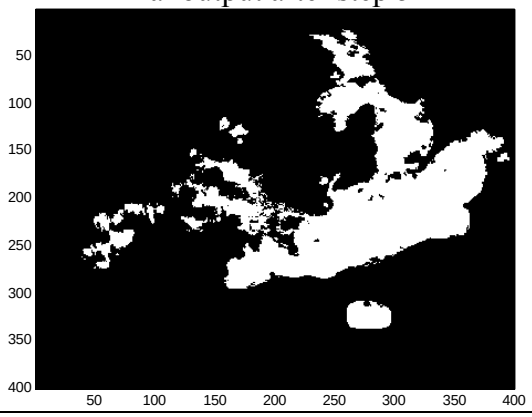


Final Output

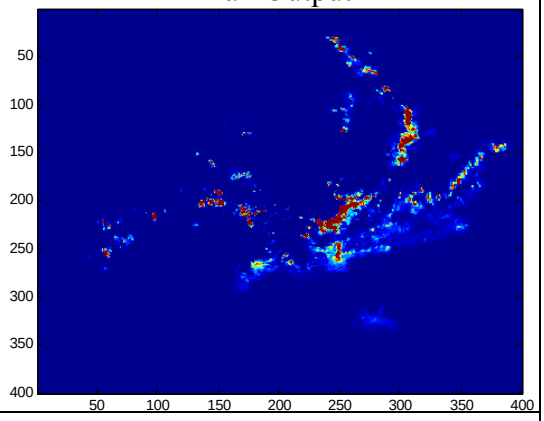


Accurate Rain Event

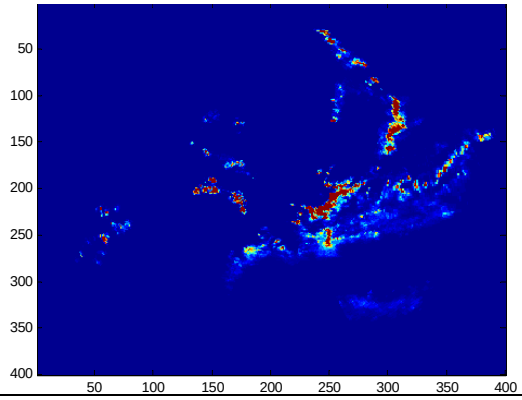

time: 21 09 hrs

Reflectivity Image elevation 1

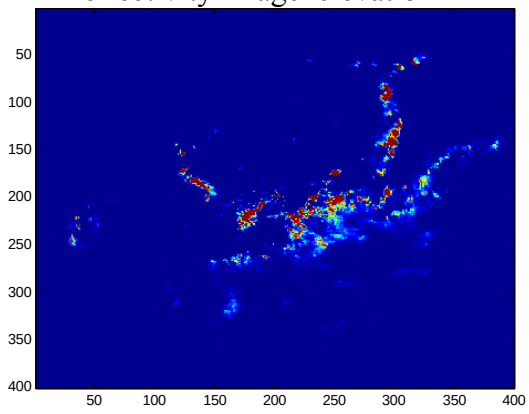


Reflectivity Image elevation 2

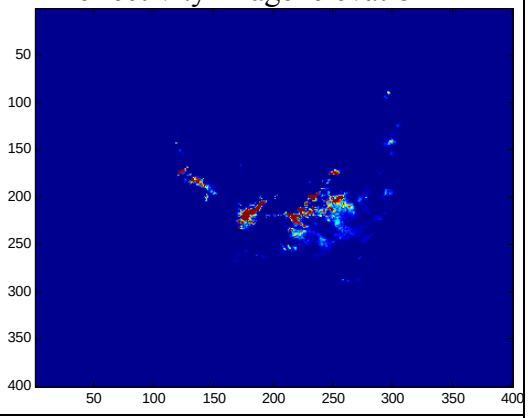


Final output after step 5

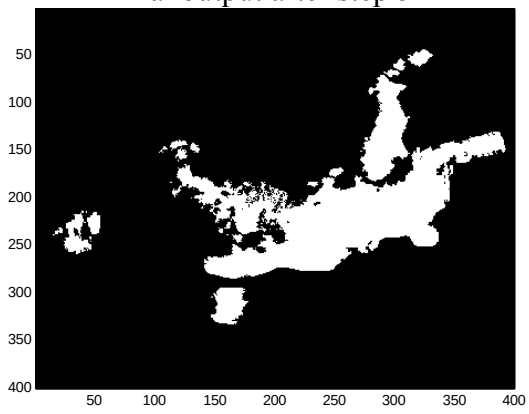


Final Output

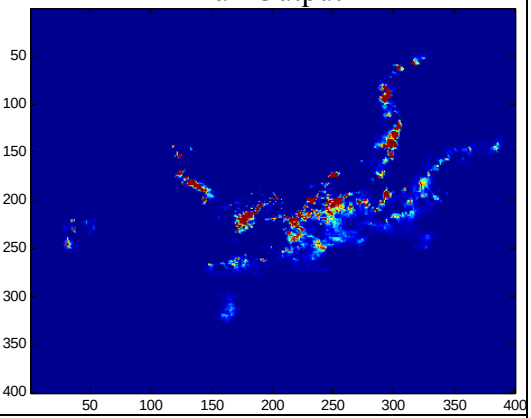


Accurate Rain Event

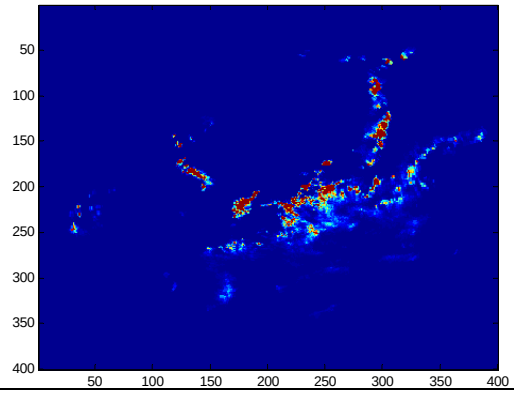

time: 22 09 hrs

Reflectivity Image elevation 1

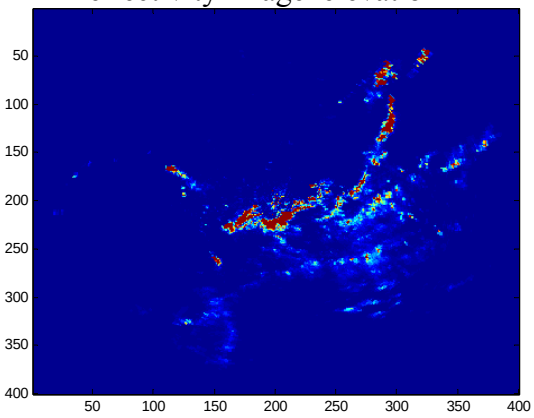


Reflectivity Image elevation 2

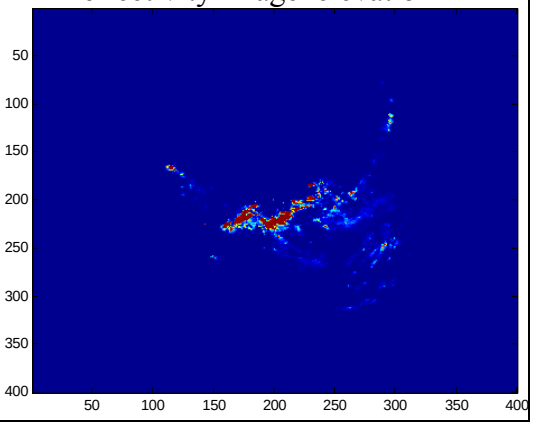


Final output after step 5

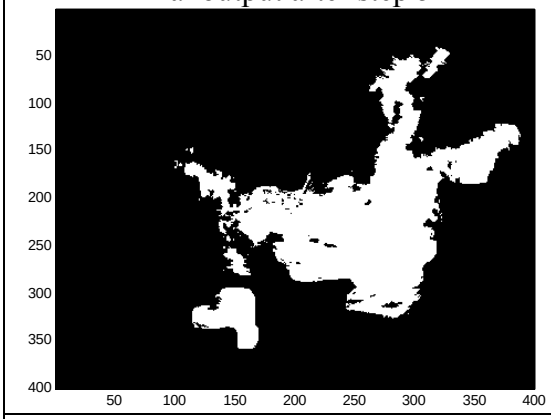


Final Output

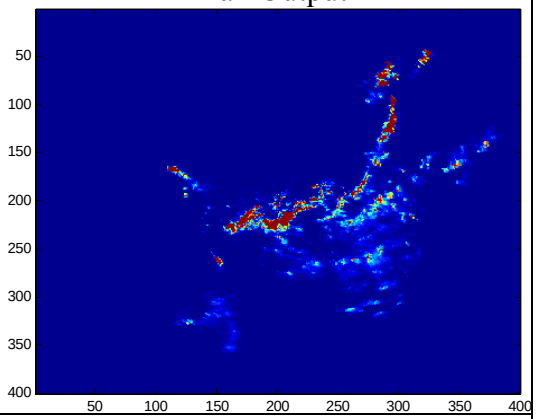


Accurate Rain Event

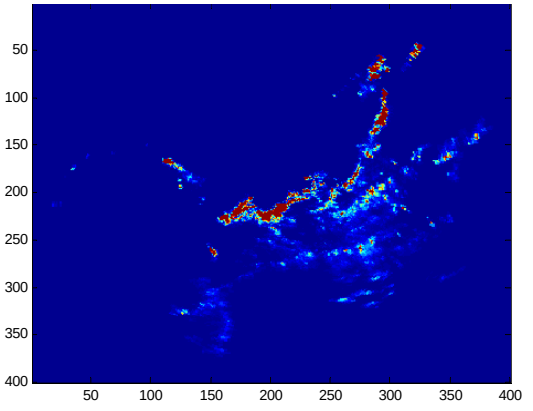

time: 24 09 hrs

Reflectivity Image elevation 1

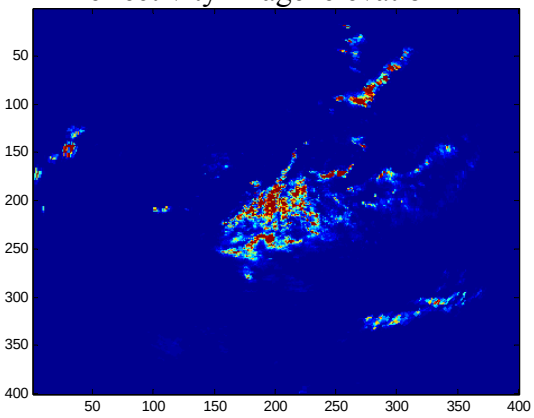


Reflectivity Image elevation 2

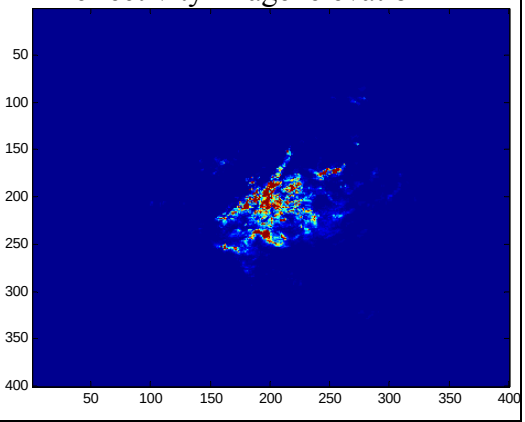


Final output after step 5

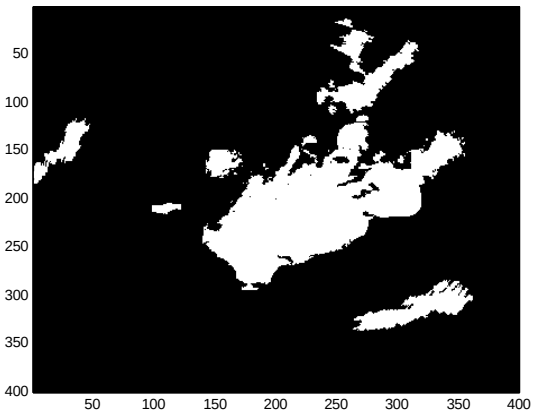


Final Output

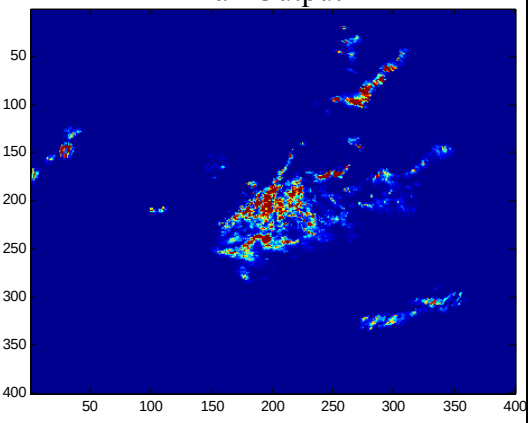


Accurate Rain Event

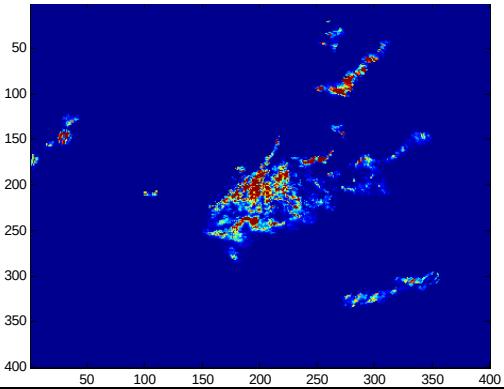

# VITA

Ms.Radhika H. Dahale was born and raised in Mumbai, India. She has received her Bachelors degree in Instrumentation and Control from the University of Pune, Pune, India in 1999.